

THE EFFECTS OF USING ALIOVALENT DOPING IN CERIUM BROMIDE
SCINTILLATION CRYSTALS

by

MARK J. HARRISON

B.S., Kansas State University, 2003
M.S., Kansas State University, 2005

AN ABSTRACT OF A DISSERTATION

submitted in partial fulfillment of the requirements for the degree

DOCTOR OF PHILOSOPHY

Department of Mechanical and Nuclear Engineering
College of Engineering

KANSAS STATE UNIVERSITY
Manhattan, Kansas

2009

Abstract

Strengthening the crystal lattice of lanthanide halides, which are brittle, anisotropic, ionic crystals may increase the availability and ruggedness of these scintillators for room-temperature γ -ray spectroscopy applications. Eight dopants for CeBr_3 , including CaBr_2 , SrBr_2 , BaBr_2 , ZrBr_4 , HfBr_4 , ZnBr_2 , CdBr_2 , and PbBr_2 , were explored at two different doping levels, 500ppm and 1000ppm, in an effort to identify potential aliovalent strengthening agents which do not adversely affect scintillation performance. All dopants and doping levels exhibited improved ingot yields over the undoped case, indicating an improvement in the ease of crystal growth.

Scintillation performance was gauged using four key metrics. Scintillation emission spectra or, rather, radioluminescence spectra were recorded using x-ray irradiation. Total light yield was estimated through pulse height comparison with bismuth germanate (BGO) scintillators. Scintillation kinetics were checked by measuring single interaction pulses directly output by a fast response PMT. Finally, light yield proportionality was measured using a Compton coincidence system.

Samples from each ingot were harvested to benchmark their performance with the four metrics. Of the eight dopants explored, only BaBr_2 and PbBr_2 clearly altered scintillation spectral emission characteristics significantly. The remaining dopants, CaBr_2 , SrBr_2 , ZrBr_4 , HfBr_4 , CdBr_2 and ZnBr_2 , altered scintillation performance to a lesser degree. No dopant appeared to affect light yield proportionality, nor did any drastically alter the light decay characteristics of CeBr_3 . HfBr_4 and ZnBr_2 -doped CeBr_3 exhibited the highest light yields, significantly higher than the undoped CeBr_3 samples tested.

Finally, aliovalent doping appeared to greatly improve CeBr_3 ingot yields, regardless of the dopant, thus it is a promising method for improving crystal strength while not deleteriously affecting scintillation performance. HfBr_4 and ZnBr_2 both demonstrated high performance without any noticeable negative side-effects and are prime candidates for future study.

THE EFFECTS OF USING ALIOVALENT DOPING IN CERIUM BROMIDE
SCINTILLATION CRYSTALS

by

MARK J. HARRISON

B.S., Kansas State University, 2003
M.S., Kansas State University, 2005

A DISSERTATION

submitted in partial fulfillment of the requirements for the degree

DOCTOR OF PHILOSOPHY

Department of Mechanical and Nuclear Engineering
College of Engineering

KANSAS STATE UNIVERSITY
Manhattan, Kansas

2009

Approved by:

Major Professor
Prof. Douglas S. McGregor

Abstract

Strengthening the crystal lattice of lanthanide halides, which are brittle, anisotropic, ionic crystals may increase the availability and ruggedness of these scintillators for room-temperature γ -ray spectroscopy applications. Eight dopants for CeBr_3 , including CaBr_2 , SrBr_2 , BaBr_2 , ZrBr_4 , HfBr_4 , ZnBr_2 , CdBr_2 , and PbBr_2 , were explored at two different doping levels, 500ppm and 1000ppm, in an effort to identify potential aliovalent strengthening agents which do not adversely affect scintillation performance. All dopants and doping levels exhibited improved ingot yields over the undoped case, indicating an improvement in the ease of crystal growth.

Scintillation performance was gauged using four key metrics. Scintillation emission spectra or, rather, radioluminescence spectra were recorded using x-ray irradiation. Total light yield was estimated through pulse height comparison with bismuth germanate (BGO) scintillators. Scintillation kinetics were checked by measuring single interaction pulses directly output by a fast response PMT. Finally, light yield proportionality was measured using a Compton coincidence system.

Samples from each ingot were harvested to benchmark their performance with the four metrics. Of the eight dopants explored, only BaBr_2 and PbBr_2 clearly altered scintillation spectral emission characteristics significantly. The remaining dopants, CaBr_2 , SrBr_2 , ZrBr_4 , HfBr_4 , CdBr_2 and ZnBr_2 , altered scintillation performance to a lesser degree. No dopant appeared to affect light yield proportionality, nor did any drastically alter the light decay characteristics of CeBr_3 . HfBr_4 and ZnBr_2 -doped CeBr_3 exhibited the highest light yields, significantly higher than the undoped CeBr_3 samples tested.

Finally, aliovalent doping appeared to greatly improve CeBr_3 ingot yields, regardless of the dopant, thus it is a promising method for improving crystal strength while not deleteriously affecting scintillation performance. HfBr_4 and ZnBr_2 both demonstrated high performance without any noticeable negative side-effects and are prime candidates for future study.

Table of Contents

List of Figures	viii
List of Tables	xi
Acknowledgements	xii
Dedication	xiii
1 Introduction.....	1
1.1 A Brief History of Scintillation.....	2
1.2 Scintillator-based γ -ray Spectroscopy.....	5
1.3 Strengthening	14
1.4 Overview.....	17
2 Strengthening of Crystals	19
2.1 Bonding.....	21
2.2 Dislocations.....	24
2.2.1 Stress Fields	28
2.2.2 Dislocation Energies	30
2.2.3 Critical Resolved Shear Stress	33
2.3 Strengthening Methods.....	34
2.4 Fracture of Single Crystals.....	36
3 Scintillation.....	39
3.1 Primary Electron-Hole Formation	39
3.2 Secondary Electron-Hole Formation	40
3.3 Thermalization	42
3.4 Migration and Light Emission	42
3.5 Characterization and Performance.....	44
3.5.1 Radioluminescence Spectrum.....	44
3.5.2 Light Yield.....	47
3.5.3 Self-Absorption.....	48
3.5.4 Proportionality of Light Yield	54

3.5.5	Decay Times	55
3.6	Summary	56
4	Experimental Methods.....	59
4.1	Crystal Growth.....	60
4.1.1	Ampoule Preparation	60
4.1.2	Growth Process	63
4.1.3	Sample Harvesting.....	67
4.1.4	Sample Preparation	68
4.2	Characterization	68
4.2.1	Radioluminescence Spectra	68
4.2.2	Total Light Yield Estimation and γ -ray Spectroscopy.....	70
4.2.3	Relative Light Yield Proportionality	76
4.2.4	Decay Constants.....	91
5	Experimental Results.....	95
5.1	Crystal Growth.....	95
5.2	Characterization and Measurements	99
5.2.1	Radioluminescence Spectra	100
5.2.2	Total Light Yield and γ -ray Spectroscopy	105
5.2.3	Light Yield Nonproportionality	108
5.2.4	Decay Constants.....	111
6	Conclusions and Discussion	115
6.1	Crystal Growth.....	115
6.1.1	Ampoule Preparation	115
6.1.2	Growth Processes.....	116
6.1.3	Sample Preparation and Preservation	117
6.2	Characterization	118
6.2.1	Radioluminescence Spectra	118
6.2.2	Total Light Yield and γ -ray Spectroscopy	120
6.2.3	Relative Light Yield Proportionality	121
6.2.4	Decay Constants.....	121
6.3	Summary	122

References.....	125
Appendix A.....	131

List of Figures

Figure 1.1. Regener’s sketch of the experimental apparatus	3
Figure 1.2. Cross-sectional view of a basic scintillator-based γ -ray spectrometer.	6
Figure 1.3. Simulated energy deposition spectrum for ^{137}Cs in a 3”x3” NaI:Tl.....	8
Figure 1.4. Simulated pulse height spectra produced by a 3”x3” NaI:Tl	10
Figure 1.5. Simulated energy absorption spectrum for a 3”x3” NaI:Tl and a 3”x3” LaBr ₃ :Ce...	10
Figure 1.6. Relative light yield of NaI:Tl	13
Figure 1.7. Projection of the UCl ₃ crystal structure of CeBr ₃	14
Figure 1.8. UCl ₃ building block of CeBr ₃	15
Figure 2.1. Basis of CeBr ₃	19
Figure 2.2. [0001] projection of CeBr ₃ lattice structure	20
Figure 2.3. One-dimensional lattice of alternating monovalent cations and anions	22
Figure 2.4. Plot of the repulsive, Madelung and total energies of NaCl.....	23
Figure 2.5. Illustration of the process Frenkel assumed responsible for plastic deformation	25
Figure 2.6. Dislocation glide.....	27
Figure 2.7. Screw dislocation in a cubic lattice	27
Figure 2.8. Determining the Burger’s vector for a dislocation	28
Figure 2.9. Definition of terms used in Eqn. (2.11).....	29
Figure 2.10. Dislocation translating through a medium	32
Figure 2.11. Visual representation of φ	32
Figure 2.12. Resolving an applied dilational stress	34
Figure 2.13. Stress concentrating at the leading tip of a crack.	37
Figure 3.1. Illustration of primary hole relaxation through the Auger effect	41
Figure 3.2. Flow diagram of the migration stage of scintillation.....	43
Figure 3.3. Mechanisms of radiative decay in Ce ³⁺ -activated compounds.....	43
Figure 3.4. Radioluminescence spectrum measured for undoped CeBr ₃	45
Figure 3.5. Spectral sensitivity curve for a Photonis XP5301B photocathode.....	46
Figure 3.6. Illustration of sample orientation and referenced dimensions.....	49

Figure 3.7. Light collection efficiencies calculated for cuboid CeBr ₃ samples.....	50
Figure 3.8. Plot of photoelectron yields published by Drozdowski et. al.....	51
Figure 3.9. Light collection efficiencies calculated for cuboid CeBr ₃ samples.....	52
Figure 3.10. Example of an added absorption energy state, E_{abs}	53
Figure 3.11. Light intensity plotted over time	56
Figure 4.1. Cross-sectional sketch of the quartz crystal growth ampoule and plug	61
Figure 4.2. Prepared ampoules laid nose-to-nose within each EDG furnace	64
Figure 4.3. Periodic plot of zone set points in the ‘single step’ recipe	65
Figure 4.4. Periodic plot of zone set points in the ‘four step’ recipe.....	66
Figure 4.5. Cross-sectional sketch of the light-tight dark box.....	69
Figure 4.6. Measured radioluminescence spectrum of undoped CeBr ₃	72
Figure 4.7. Calibration curve for the MCA.....	73
Figure 4.8. Cross-sectional sketch of a sample scintillator crystal mounted.....	75
Figure 4.9. Diagram of the NIM setup used to collect γ -ray spectra.....	75
Figure 4.10. Top and side view sketches of the source-sample geometry.....	81
Figure 4.11. Sketch of the source-sample geometry for high angle scatter data acquisition.....	81
Figure 4.12. Plot of the energy deposited E_e and scattered γ -ray energy E'_γ	82
Figure 4.13. Connection diagram for the relative light yield coincidence system	83
Figure 4.14. Example singles spectrum collected from the PMT.....	86
Figure 4.15. Example singles spectrum collected from the HPGe detector	86
Figure 4.16. Example three dimensional surface plot of the data point density.....	87
Figure 4.17. Example plot of the data from a single \bar{E}_e bin.....	88
Figure 4.18. Example plot of the data from a single \bar{E}_e bin.....	90
Figure 4.19. Example scatter plot of a final data set collected	90
Figure 4.20. Example plot of relative light yields calculated	91
Figure 4.21. Comparison of the pulse shapes of NaI:Tl and undoped CeBr ₃	92
Figure 5.1. First ingot grown, HG1, with HGF method under UV lighting.....	95
Figure 5.2. Ingots HB2 and HB3 under normal lighting.	96
Figure 5.3. Ingot HB6, undoped CeBr ₃ under normal light.....	96
Figure 5.4. Ingot HB22, 1000ppm HfBr ₄ doped CeBr ₃ as photographed under UV lighting	97

Figure 5.5. Sketch of the before and after distillation states.....	99
Figure 5.6. Collected radioluminescence emission spectra for BGO, NaI:Tl and LaBr ₃ :Ce.....	100
Figure 5.7. Collected radioluminescence emission spectra for Ca-doped CeBr ₃	101
Figure 5.8. Collected radioluminescence emission spectra for Sr-doped CeBr ₃	101
Figure 5.9. Collected radioluminescence emission spectra for Ba-doped CeBr ₃	102
Figure 5.10. Collected radioluminescence emission spectra for Ca-doped CeBr ₃	102
Figure 5.11. Collected radioluminescence emission spectra for Hf-doped CeBr ₃	103
Figure 5.12. Collected radioluminescence emission spectra for Zn-doped CeBr ₃	103
Figure 5.13. Collected radioluminescence emission spectra for Cd-doped CeBr ₃	104
Figure 5.14. Collected radioluminescence emission spectra for Pb-doped CeBr ₃	104
Figure 5.15. Collected radioluminescence emission spectra for undoped CeBr ₃	105
Figure 5.16. Example γ -ray spectra collected.....	108
Figure 5.17. Relative light yield curves for NaI:Tl, LaBr ₃ :Ce and undoped CeBr ₃	109
Figure 5.18. Relative light yield curves for CeBr ₃ doped with Group IIA cations.....	109
Figure 5.19. Relative light yield curves for CeBr ₃ doped with Group IIB cations.....	110
Figure 5.20. Relative light yield curves for CeBr ₃ doped with Group IVA cations.....	110
Figure 5.21. Relative light yield curves for CeBr ₃ doped with Group IVB cations.	111
Figure 5.22. Voltage pulses as collected for the various Group IIA samples.....	112
Figure 5.23. Voltage pulses as collected for the various Group IIB samples.....	112
Figure 5.24. Voltage pulses as collected for the various Group IVA samples.....	113
Figure 5.25. Voltage pulses as collected for the various Group IVB samples.....	113
Figure 6.1. Photograph showing the strain in the single crystals of doped CeBr ₃	116
Figure 6.2. Measured temperature profiles of the EDG furnaces.....	117
Figure 6.3. Two Gaussian peaks fit to the Ba-doped CeBr ₃ radioluminescence data set.....	118
Figure 6.4. Radioluminescence emission peak locations.....	119
Figure 6.5. Radioluminescence emission peak area fractions.	120

List of Tables

Table 2.1. Positions of Ce and Br atoms in the unit cell.....	20
Table 4.1. Target doping masses.....	62
Table 4.2. RLY Coincidence System Equipment List.....	84
Table 4.3. Diagram illustrating how four collection cycles are used.....	85
Table 5.1. Ingot masses, resulting dopant concentrations, and ingot results.	98
Table 5.2. Estimated integral quantum efficiencies (IQE) for the materials	105
Table 5.3. Dimensions of total light yield samples.....	106
Table 5.4. Estimated total light yields and energy resolution (FWHM) of each sample.....	107
Table 6.1. Radioluminescence data analysis.....	119

Acknowledgements

The author is greatly indebted to Prof. Douglas S. McGregor and the members of the Semiconductor Materials and Radiological Technologies (SMART) Laboratory at Kansas State University and would like to thank the following people, in no particular order, for their invaluable contributions to this work: Dr. Philip Ugorowski, Chris Linnick, Tyler Krehbiel, Mark McCreary, Ben Montag, Samuel Brinton, Walter McNeil, Alireza Kargar, Martin Ohmes, Steven Bellinger, Blake Rice, Elsa Ariesanti, Adam Brooks, Michael Meier, Kyle Nelson, Fernando Sierra, Troy Unruh and Brian Cooper. The author also wishes to thank Dr. F. Patrick Doty with Sandia National Laboratories for the many fruitful discussions, guidance and advice. Also, the author would like to thank Dr. Bill Dunn and the Stand-Off Bomb Detection Laboratory at Kansas State University for the use of their x-ray generator. Finally, the author wishes to extend his appreciation to his advising committee including Dr. Krishna Mandal, Prof. Bruce Babin, Prof. Andrew Rys, Prof. James Edgar, and Prof. Christopher Levy for their guidance and support.

Dedication

I would like to dedicate this work to my beautiful fiancée, courageous brother, and wonderful parents. Your encouragement has always provided me with the strength to keep moving forward, even during those darkest of hours. Thank you.

1 Introduction

Thallium-doped sodium iodide (NaI:Tl) scintillator-based γ -ray spectrometers have been an important technology since their introduction in 1948 [1]. Despite the introduction of semiconductor-based spectrometers in the early 1960s with superior energy resolution characteristics [2,3], the NaI:Tl spectrometer has remained a staple of γ -ray spectroscopy because NaI:Tl crystals are relatively inexpensive, available in large sizes, have intrinsically high efficiencies, and operate at room-temperature. Semiconductor-based spectrometers, the primary alternative technology to scintillator-based systems, have several attractive features, but are often precluded from field applications due to various limitations.

Mature semiconductor materials, such as Ge or Si, suffer from high thermally-generated leakage currents and excessive electronic noise at room temperature because they have narrow energy gaps. Thus, high purity Ge (HPGe) and lithium-drifted Si (Si(Li)) spectrometers are operated at LN2 temperatures. This low temperature requirement complicates remote use of these narrow energy gap semiconductor spectrometers.

Certain wide band gap semiconductors, such as mercuric iodide (HgI₂), cadmium zinc telluride (CdZnTe), and more recently thallium bromide (TlBr), have been under development for years to remove the burden of cooling from semiconductor-based spectrometers, but available volumes are still limited to approximately 1 cm³ and raw crystal costs are expensive (e.g. \$4600 per cm³ for CdZnTe [4]). NaI:Tl scintillator crystals, on the other hand, are readily available in volumes of 350 cm³ for \$3.17 per cm³ [5]. These drastic differences leave a huge gap in pricing and efficiency for the two most common room-temperature-operated technologies.

While NaI:Tl is the preferred scintillator material for γ -ray spectroscopy due to its high Z , high mass density, and reasonably high light yield, it is limited in performance. The energy resolutions achievable with NaI:Tl are typically near 6-7% full width at half maximum (FWHM) at 662keV [6] and the light decay constant ($\tau = 230$ ns) is not suitable for high speed applications. Finally, NaI:Tl exhibits a non-proportional response to γ -rays with respect to deposited energy, varying by up to 20% over the range of 1keV to 1000keV [7].

Numerous searches for higher performance scintillating materials for approximately 50 years were not successful though. Bismuth germanate ($\text{Bi}_4\text{Ge}_4\text{O}_{12}$ or BGO) was primarily designed to produce a dense, high Z crystal for good γ -ray attenuation [8]. Barium fluoride (BaF_2), known to be a scintillator at least as early as 1928 [9], has a relatively low light yield but exhibits a fast light decay for high count rate and timing applications. Thus, niche materials have been developed for certain applications, but no single material has been superior to NaI:Tl for traditional performance metrics until recently with the introduction of cerium-doped lanthanum bromide ($\text{LaBr}_3\text{:Ce}$) in 1999 [10,11]. To fully appreciate the leap forward provided by $\text{LaBr}_3\text{:Ce}$, a brief review of the history of scintillation is in order.

1.1 A Brief History of Scintillation

The physical phenomenon of scintillation has played a key role in nuclear physics even before the nucleus was discovered. As pointed out by Becquerel, M. and Mme. Curie were the first to recognize that barium platinocyanide ($\text{BaPt}(\text{CN})_4$) screens fluoresced in response to radiation emitted by a radioactive substance [12]. In fact, Wilhelm Conrad Röntgen used a $\text{BaPt}(\text{CN})_4$ fluorescent screen to detect cathode rays on November 8, 1895, when he first detected x-rays [13]. The discovery of the light emission from certain materials when exposed to radiation led to a series of breakthroughs that eventually brought about the practical use of scintillators as radiation detectors. At present, scintillators are the technology of choice for room-temperature-operated γ -ray spectroscopy applications.

It was not recognized at first that each quantum of radiation produced a small flash of light in these scintillators, rather the glow resulting from exposure to radium was observed to be uniform. Sir William Crookes, however, noted upon closer inspection that the “uniform glow” was actually a sea of small, bright flashes of light that he termed “scintillations” [14]. Crookes went on to develop what he called the “spinhariscope” in which one could easily observe the phenomenon of scintillation. Later experiments by Rutherford and Geiger, who used an ionization method to check scintillation counting results, proved that each flash of light was actually a single alpha particle striking the thin screen [15,16].

In 1908, Regener devised a method to determine the number of α -particles striking the screen by counting individual scintillations on a screen [17-19]. A sketch of his experimental apparatus is reprinted in Figure 1.1. This was a major step forward and provided a method by

which many important scattering experiments could be conducted. It was not until the late 1920s before researchers began to seriously study the phenomenon of scintillation as it applied to scintillation counting [20-23]. During this classical period of visual scintillation counting, good eye sight and the ability to concentrate for long periods of time was crucial to becoming a competent experimentalist [24].

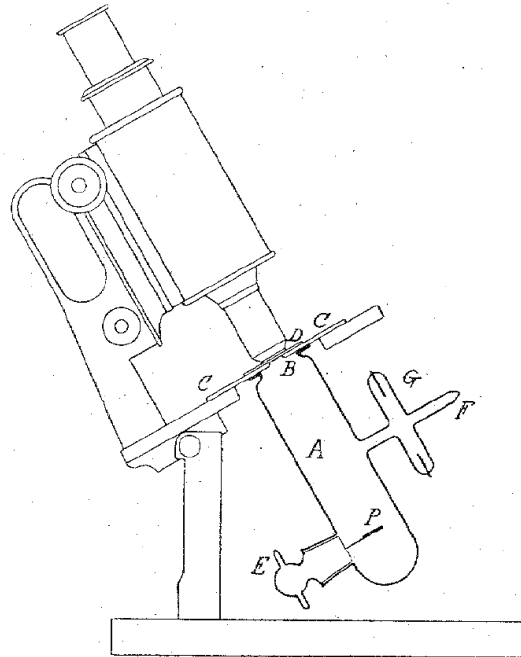


Figure 1.1. Regener's sketch of the experimental apparatus used to count scintillations on a ZnS screen [19]. An evacuated glass tube, which held a polonium source at one end and a ZnS screen at the other, was positioned directly in the field of view of a microscope. Reprinted with permission.

By 1930, the practice of visually counting scintillations was giving way to electronic counting methods devised for gas ionization chambers [25]. This was a relatively inactive period for scintillators. Scintillators were noted, however, as having superior discrimination between α -particles and β -particles or γ -rays [24], so were likely useful in that capacity. Finally, in 1941, Krebs first attempted to electronically count scintillations from a ZnS screen by using a photosensitive Geiger-Müller counter [26]. This was an exciting development since electronically counting scintillations removed from an experiment the uncertainties inherent in an experimentalist's eyes and concentration. Geiger-Müller tubes, however, were quickly replaced by a far better technology.

The first use of a photomultiplier tube (PMT) to count scintillations occurred under the Manhattan Project in 1944 at the University of California at Berkeley by Curran and Baker [27]. They arranged an RCA 1P21 PMT over a ZnS screen. The PMT output was connected to an oscilloscope that allowed them to visualize the pulses from 2 MeV α -particles. Of course, this work was originally classified but was later disclosed in 1948 [28]. The first publicly disclosed use of a PMT to measure scintillations was done by Blau and Dreyfus [29].

The next step toward a γ -ray spectrometer was taken when Kallman optically coupled a large, transparent block of naphthalene to a PMT to observe α -particles, β -particles and γ -rays in 1947 [30]. This was the first time a thick block of scintillator was used, paving the way for Hofstadter. In 1948, Hofstadter introduced NaI:Tl in polycrystalline form and demonstrated its ability to be used for γ -ray detection [1]. Soon after, it was shown that single crystals of NaI:Tl were capable of providing spectroscopic information when coupled to photomultiplier tubes. This was a huge leap forward in γ -ray spectroscopy and the radiation detection field in general. Prior to Hofstadter's discovery, γ -ray spectroscopy was accomplished by reflecting off crystal lattices [31] or with proportional gas ionization detectors [32]; both of which were inefficient.

As a side note, Villard discovered 'radiations très pénétrantes' in 1900 using photographic film [33] (later named γ -rays by Rutherford in early 1903). However, the nature and origin of these new penetrating rays remained undetermined until 1914 when Rutherford and Andrade performed their reflection experiment [34].¹

After Hofstadter's discovery of NaI:Tl, inorganic scintillators were of great interest for the following decade. Cadmium tungstate (CdWO_4) [36], thallium-doped cesium iodide (CsI:Tl) [37], pure CsI [38], cesium fluoride (CsF) [39], and europium-doped lithium iodide (LiI:Eu) [40] were all discovered in the 1950s. This period of excitement then dwindled for the next 20 years. Only CsI:Na [41], europium-doped calcium fluoride (CaF_2 :Eu) [42] and BGO [8] were notable discoveries of the 1960s and 1970s.

The 1980s brought about renewed interest in inorganic scintillators due to newly developed requirements from the fields of medicine and high energy physics [7]. The 1990s

¹ It has been pointed out in fact that Rutherford, Becquerel, the Curies, and Röntgen all received Nobel Prizes for their respective contributions to the discoveries of α -particles, β -particles and x-rays, but Villard was passed over [35]. It is unfortunate that Villard has since been nearly forgotten for his contribution to nuclear science.

expanded on the increasing trend in the search for new, higher performance scintillators with an explosion of discoveries. In 1997, Rodnyi predicted that Ce-doped and Ce-based scintillators appeared to be the predominately promising class of scintillators for investigation. Indeed, within two years, the development of the cerium-doped lanthanum halide family, including cerium-doped lanthanum chloride ($\text{LaCl}_3:\text{Ce}$) and lanthanum bromide ($\text{LaBr}_3:\text{Ce}$), was announced [10,11]. Energy resolutions decreased from the standard 6-7% FWHM at 662keV characteristic of NaI:Tl [6] to nearly 3% FWHM with $\text{LaBr}_3:\text{Ce}$ [43]. Since then, a flourish of activity has surrounded this family in the research community. Unfortunately, availability of $\text{LaBr}_3:\text{Ce}$ on the commercial market is still limited due to difficulties in achieving high yields of large, crack-free crystals [44].

In 2003, Radiation Monitoring Devices Inc. published data indicating undoped CeBr_3 was nearly equivalent in performance to $\text{LaBr}_3:\text{Ce}$ [45]. This greatly simplified the manufacturing processes necessary to producing large single crystals. A self-activated crystal avoids certain issues surrounding the doping of a host lattice. Without the need for an activator dopant, segregation of activator during melt growth of crystals was no longer a concern. Unfortunately, similar to LaBr_3 , CeBr_3 also orients into a hexagonal lattice with low fracture toughness [46]. Despite easing the difficulty of crystal growth by eliminating the need for a dopant, widespread use of CeBr_3 still faces difficulties similar to LaBr_3 in producing large single crystals inexpensively.

1.2 Scintillator-based γ -ray Spectroscopy

A basic scintillator-based γ -ray spectrometer most commonly includes a large, single crystal of a scintillating material that is optically coupled to a photomultiplier tube (PMT) assembly or a photodiode. Figure 1.2 illustrates the basic setup for a spectrometer constructed with a PMT assembly as the light converter. The detection of an energy absorption event requires several steps in the system depicted in Figure 1.2. The steps are:

1. Scintillation light produced
2. Light collected at photocathode
3. Photoelectrons emitted
4. Electrons multiplied through dynodes

5. Current induced on anode

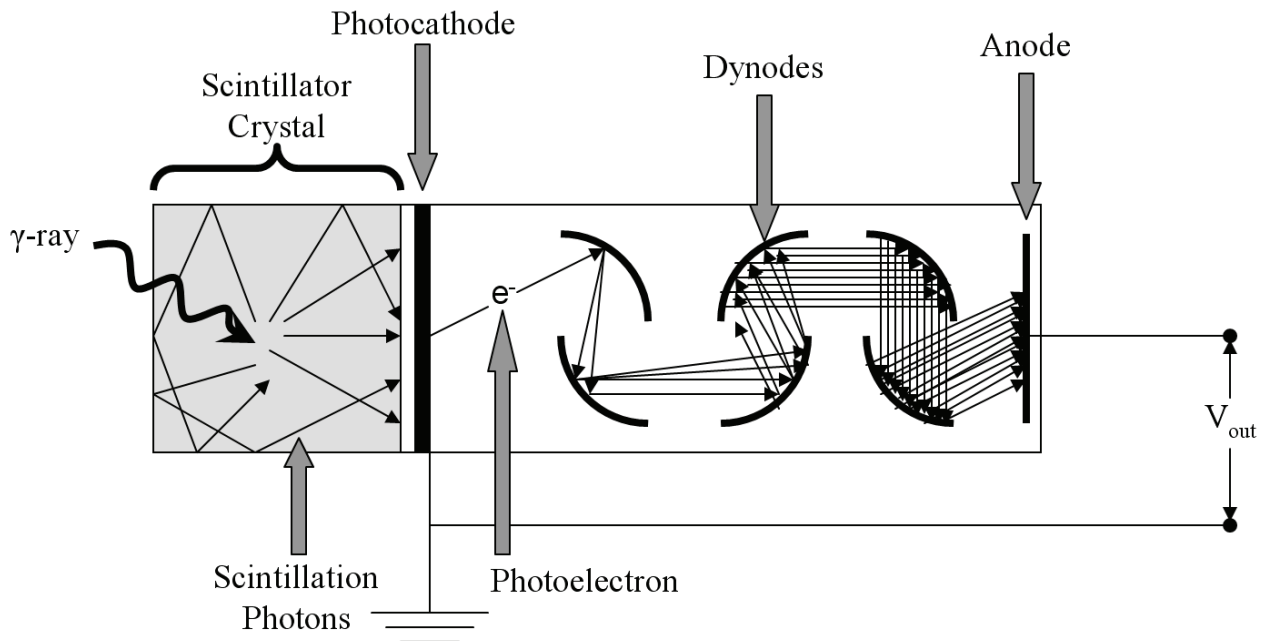


Figure 1.2. Cross-sectional view of a basic scintillator-based γ -ray spectrometer.

The first stage in the detection process involves the emission of light by the scintillator. When a quantum of radiation imparts some or all of its energy to the scintillator crystal, electrons are excited into higher energy states leaving behind energetic holes. Holes are simply the absence of an electron in a normally occupied energy state. The relaxation of the excited electrons and holes to their ground energy states can occur along several paths, a few of which result in radiative emission of scintillation light. The number of photons emitted during these radiative relaxations is roughly proportional to the amount of energy deposited by the radiation quantum. The physical mechanisms of de-exciting these high energy electrons and holes are discussed more thoroughly in Chapter 3.

Light produced during the scintillation process must be collected at the photocathode. Scintillator crystals are generally wrapped or coated with a highly reflecting layer such as MgO to maximize the light collection efficiency at the photocathode. Before reaching the cathode, the light must also pass through the coupled crystal face, a thin layer of optical coupling grease or epoxy, and a window (e.g. quartz). Indexes of refraction of the various layers are carefully matched to minimize reflections and maximize light collection.

Photons striking the photocathode can cause electrons to be ejected into a vacuum. The incident photons must impart energies greater than the work function of the photocathode material in order for electrons to be ejected into vacuum. Of the electrons excited, only a fraction actually reach the surface of the photocathode and enter the vacuum surrounding the PMT. Free, ejected photoelectrons are then accelerated into a series of dynodes with an applied electric field.

The dynodes within a PMT are biased such that photocathode-ejected electrons or, rather, “photoelectrons” are accelerated into each dynode in sequence. When a dynode is struck by a fast-moving electron, more electrons are released into the cascade. Thus, a single photoelectron ejected by the photocathode might release 10 electrons after the first dynode, 100 after the second dynode, and so on. Gains on the order of 1×10^6 are readily achievable through a 10 dynode sequence [47].

Finally, the electrons emitted by the last dynode induce a current on the collecting anode as they approach. A capacitively-coupled operational amplifier (not shown in Figure 1.2) then isolates and amplifies the current pulse before sending a voltage tail pulse on to shaping and counting electronics. The magnitude of the tail pulse is roughly proportional to the original energy absorbed in the scintillator crystal.

Analog tail pulses from a γ -ray spectrometer are generally amplified to peak within the range 0-10V and shaped into a Gaussian pulse by a shaping amplifier. Each 0-10V Gaussian pulse is then passed to a multi-channel analyzer (MCA). An MCA captures the peak height of an analog 0-10V Gaussian pulse, then histograms the peak voltage into a channel. Multi-channel analyzers are typically 14-bit systems, so have a maximum of 16,384 channels and a minimum bin width of 0.61 mV. This amplification and binning process occurs for every γ -ray interaction inside the scintillator crystal. Over many pulses, a differential pulse height spectrum is formed, which is effectively a discrete approximation of the frequency of interaction versus energy deposition within the scintillator.

The energy absorption spectrum within a scintillator crystal is determined by material Z number, mass density, geometry and size. Figure 1.3 shows an energy absorption spectrum for ^{137}Cs uniformly irradiating the front face of a 3”x3” NaI:Tl scintillator crystal. The resulting spectrum has two main features, a full energy peak (FEP) and a Compton continuum. The FEP is the result of complete energy absorption of the γ -ray through either a single photoelectric absorption or one or more Compton scatter events followed by a photoelectric absorption. The

Compton continuum is formed by incomplete absorptions, such as a Compton scatter in which the scattered photon escapes the scintillator without further interaction.

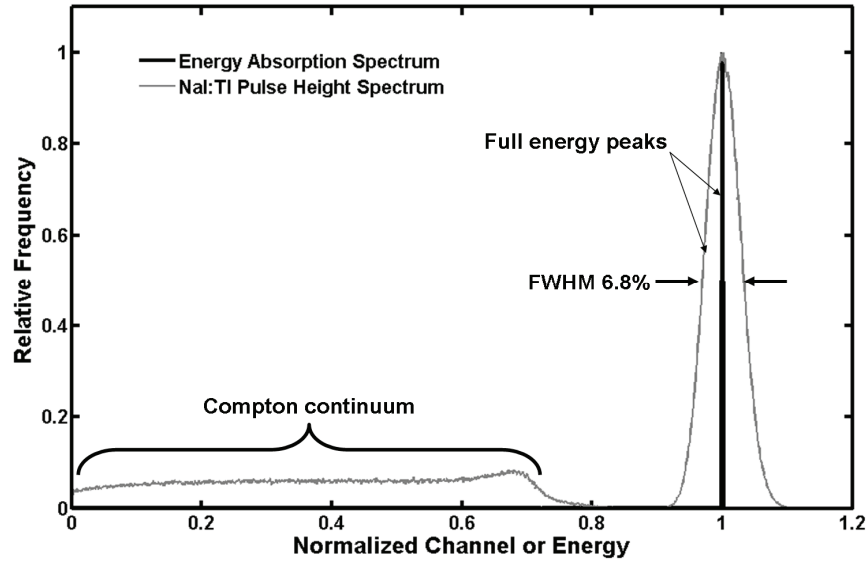


Figure 1.3. Simulated energy deposition spectrum for ^{137}Cs in a 3''x3'' NaI:Tl scintillator crystal and the corresponding pulse height spectrum from the same crystal coupled to a PMT.

A spectrometer attempts to capture the true energy absorption spectrum, but necessarily fails due to spectrometer system statistical limitations, nonlinearities, and discretization of the output. The pulse height spectrum produced in a non-ideal spectrometer thus is simply an approximation of the true energy absorption spectrum. Adding the requisite sources of error, the pulse height spectrum becomes a blurred version of the energy deposition spectrum like that shown in Figure 1.3. Note that the FEP has widened considerably, from a single channel to a broad Gaussian-shaped peak. The width of the peak and thus energy resolution is described by the full width at half maximum (FWHM or Γ) value. Here, the 3''x3'' NaI:Tl spectrometer produced a FEP with energy resolution of 6.8% FWHM at 662keV, while the energy absorption peak is actually vanishingly narrow but limited to one channel due to the discretization of the MCA. The FWHM is simply the number of channels (or equivalently energy) the peak is wide at half its maximum height. The FWHM is normally expressed as a percentage of the peak channel in scintillator-based spectrometer systems.

The usefulness of the data collected by a γ -ray spectrometer is ultimately dependent upon how quickly and accurately a γ -emitting isotope can be identified. The two main

characteristics that make a γ -ray spectrometer useful are the absorption efficiency and energy resolution. γ -ray spectra collected using a scintillator-based spectrometer, amplifying electronics and a multi-channel analyzer (MCA) are generally analyzed by an operator or a computer-based algorithm to determine isotope and strength. The ability to discern closely spaced γ -ray emissions is key to isolating the specific isotope under investigation. Spectrometers with high energy resolution (narrow FWHM) can easily differentiate between closely spaced γ -ray emissions, whereas a spectrometer with low energy resolution (wide FWHM) may show only one broad peak that in reality contains multiple γ -ray emissions.

NaI:Tl in the configuration illustrated in Figure 1.2 has been a staple of the room-temperature γ -ray spectroscopy industry for years. As a whole, the detector assembly with NaI:Tl typically produces energy resolutions on the order of 6-7% FWHM at 662 keV [6]. A similarly configured LaBr₃:Ce detector produces energy resolutions in the range of 3% FWHM at 662 keV by comparison [43]. A reduction in energy resolution greatly improves the usefulness of the device.

As an example, let us define a hypothetical isotope called ‘Makebelievium-300’ (³⁰⁰Mk). ³⁰⁰Mk emits γ -rays with energies of 630keV and 690keV with equal probability. Pulse height spectra of solely ¹³⁷Cs and of both ³⁰⁰Mk and ¹³⁷Cs with a 3”x3” NaI:Tl scintillation spectrometer are recorded. For this case, assume the ³⁰⁰Mk activity to be approximately 40% of the ¹³⁷Cs activity. The resulting pulse height spectra might look like those shown in Figure 1.4. Notice that despite the addition of two γ -ray emissions, the combined isotope spectrum is very similar to the single ¹³⁷Cs spectrum. Therefore, it is seen that a NaI:Tl spectrometer is inadequate to detect and properly quantify the ³⁰⁰Mk activity in this particular case.

Now, suppose a LaBr₃:Ce scintillation spectrometer is utilized to record a spectrum of the combined ³⁰⁰Mk and ¹³⁷Cs sources as before. The resulting pulse height spectrum from the LaBr₃:Ce spectrometer as shown in Figure 1.5 clearly exhibits three full energy peaks, unlike the NaI:Tl system. The energy absorption spectrum changes very little between the two scintillator materials, yet the information provided by the LaBr₃:Ce is far superior to the NaI:Tl spectrometer. Identification and quantification of the ³⁰⁰Mk activity thus becomes possible with the LaBr₃:Ce spectrometer.

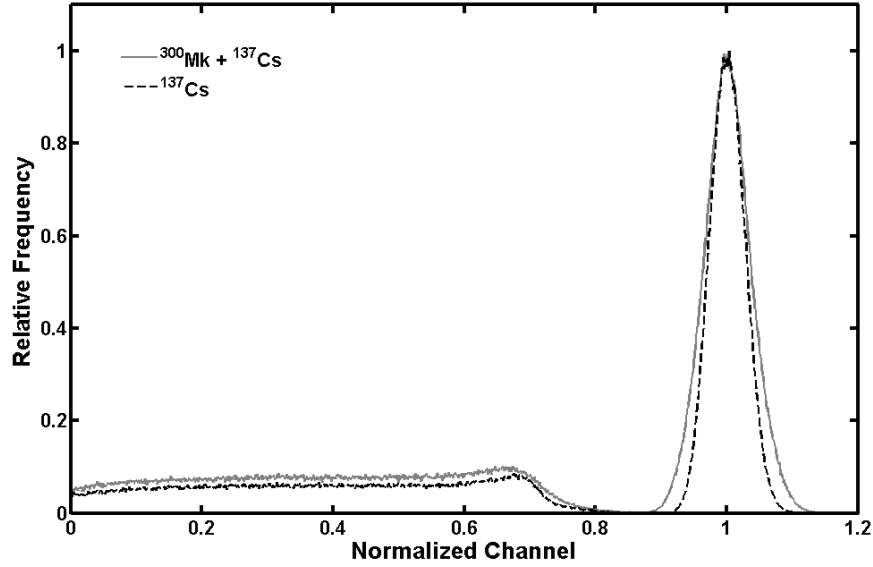


Figure 1.4. Simulated pulse height spectra produced by a 3”x3” NaI:Tl scintillation spectrometer in response to two source configurations, one with only a ^{137}Cs source present and one in which both ^{300}Mk and ^{137}Cs sources are present.

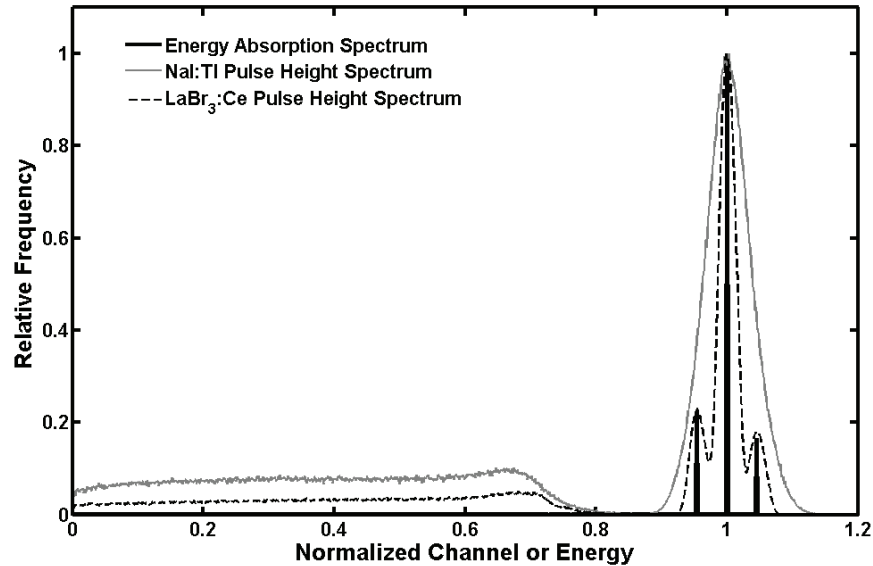


Figure 1.5. Simulated energy absorption spectrum for a 3”x3” NaI:Tl scintillation crystal and pulse height spectra produced by a 3”x3” NaI:Tl and a 3”x3” LaBr₃:Ce scintillation spectrometer in response to both ^{300}Mk and ^{137}Cs sources.

Energy resolution is limited by many factors. One critical parameter is the total light yield of the scintillator material. The total light yield is the number of photons emitted per unit of energy deposited. NaI:Tl emits approximately 50,000 photons/MeV at 662keV [48], whereas

LaBr₃:Ce emits approximately 61,000 photons/MeV at 662keV [7]. The statistics surrounding the generation of light is generally described as Gaussian. Thus, the variance in light output for a given energy is simply the mean light yield, e.g. for NaI:Tl producing on average (μ) of 26,480 photons for a 662keV energy absorption event, the standard deviation in light production (σ) is 163 photons. Since FWHM (Γ) is related to σ by

$$\Gamma = (2\sqrt{2\ln 2})\sigma, \quad (1.1)$$

the percent FWHM of the light generated is then

$$\Gamma(\%) = \frac{\Gamma}{\mu} \times 100\% = 1.4\%.$$

But the light generation variance is only one of many contributions to the total observed FWHM of a FEP. In addition to the stochastic variance of light generation as described above, the spatial variance in activator concentration can also have an impact [49] as can many other factors. After light is generated, it must be collected at the photocathode. Light collection efficiency (generally on the order of 50% for a NaI:Tl right rectangular prism [25]) also has a variance associated with it as does the next step. The generation of photoelectrons by the photocathode described by the quantum efficiency also introduces a requisite variance to the system. The quantum efficiency (QE) of a photocathode is a measure of how many photoelectrons are generated and ejected into the PMT vacuum per scintillation photon striking the photocathode. For a typical 3"x3" NaI:Tl crystal mounted to a bialkali photocathode, the QE is on the order of 35% [47].

The statistics surrounding photoelectron generation are the most crucial because it is at this point in the signal generation process that the total number of 'information carriers' is at its lowest. For instance, assume 26,480 photons were generated in NaI:Tl when 662keV of energy was absorbed and 50% of those photons (13,240 photons) were collected by the photocathode. Of these collected photons, only 35% then produce photoelectrons. The average number of photoelectrons being ejected into the PMT is then 4634 e⁻. Again, this process is assumed to follow Gaussian statistics, thus the standard deviation is 68 e⁻ or 3.5% FWHM. Generally, the

limiting process in achieving high energy resolution PMT-type scintillation spectrometers is the photoelectron generation process at the photocathode as it contributes the most to the overall variance. The numerous processes discussed above in generating a signal are all generally described using Gaussian statistics and are assumed to be independent of one another, thus they can be added in quadrature when estimating the total variance of a FEP.

Several other factors also contribute to the overall FEP width. For instance, in Figure 1.2, the efficiency of light collection at the far right surface near the photocathode may be 52% while the light collection efficiency at the far left surface may only be 50%. The photocathode QE is sensitive to what wavelengths of light are emitted by the scintillator, the photocathode geometry and the material from which the photocathode is constructed. Also, the photocathode normally generates a small leakage current due to thermal excitation of electrons from the photocathode into the vacuum. Cooling of the photocathode avoids this problem, but is counter-productive to producing a room-temperature-operated device. Finally, electron multiplication at the dynodes is highly sensitive to applied bias. Total PMT amplification has a power function relationship to applied bias, thus any noise present in the bias manifests itself as fluctuations in amplification. However, despite these drawbacks, PMTs are considered low noise, high gain amplifiers and are the preferred technology for most scintillator-based γ -ray spectrometer applications.

Nonproportional light yield is yet another contributing factor in degrading energy resolution, especially in large, high efficiency spectrometers. The total light produced per unit energy is not constant for all energies in most scintillator materials, thus is nonproportional. NaI:Tl exhibits higher light yields for mid-range energy absorptions. LaBr₃:Ce, on the other hand, has a much more proportional response over a wide range of energies. Figure 1.6 illustrates these trends for NaI:Tl and LaBr₃:Ce. Notice that the light yield at 35keV is approximately 7% more for NaI:Tl than at 662keV. Typically, nonproportionality is measured not by measuring the absolute total light yield at all energies, but by measuring light yields relative to those measured at 662keV to provide a relative light yield comparison. This measurement process is described in much greater detail in Chapter 4.

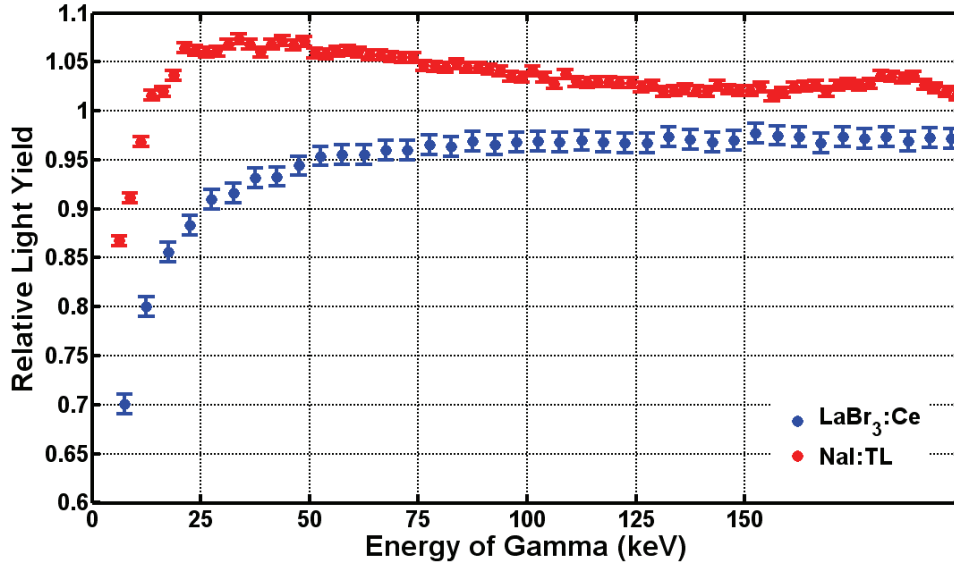


Figure 1.6. Relative light yield of NaI:Tl for the energy range 5keV to 225keV as measured using a Compton coincidence system.

Nonproportionality acts to widen a FEP when full energy absorption is not accomplished by a single photoelectric absorption, but rather through one or more Compton scatter events followed by a photoelectric absorption. To illustrate this point, first observe that NaI:Tl produces 26,480 photons for a single photoelectric absorption of a 662keV γ -ray. However, if the original γ -ray first Compton scatters twice (depositing 35keV each time) and then is fully absorbed through photoelectric absorption, it produces approximately 26,676 photons. This double scatter-absorption scenario then produces a PH approximately 0.74% wider than the direct photoelectric absorption case. Nonproportional response of scintillators becomes a greater problem as crystal sizes are increased because the probability of capturing all the energy from a Compton scattered γ -ray increases. Small scintillator crystals are less likely to recapture a Compton scattered γ -ray, thus are less affected by nonproportional light yields.

Ce-based and Ce-doped lanthanide halide scintillators generally exhibit improved light proportionality and total light yields as compared to NaI:Tl. Furthermore, the wavelengths of light produced by these scintillators generally couple well to common photocathode materials, making quantum efficiencies quite favorable. Overall, these qualities ensure spectroscopic performance of Ce-based and Ce-doped lanthanide halides is far superior to NaI:Tl. However, these ionic crystals exhibit very limited and anisotropic plasticity and brittle fracture; both of which play a key role in limiting the availability of the material.

1.3 Strengthening

CeBr₃ forms a hexagonal crystal lattice with the uranium (III) chloride (UCl₃) prototype structure [50] shown in Figure 1.7. For LaBr₃, the cation, La³⁺, is 9-fold coordinated about Br⁻ anions [46] with its six nearest neighbors located 3.10Å away and the next three 3.15Å away. Figure 1.8 illustrates the basic 9-fold coordinated structure found in LaBr₃ and CeBr₃.

Lattice constants for LaBr₃ are $a = 7.97\text{\AA}$ and $c = 4.92\text{\AA}$. This low c/a ratio is also demonstrated by CeBr₃ as well. Both CeBr₃ and LaBr₃ are extremely brittle crystals, cleaving preferentially along the prismatic planes, parallel to the c -axis. Theoretical treatments on the subject indicate that slip along these prismatic planes is much more likely to occur than slip along the c or basal plane [46].

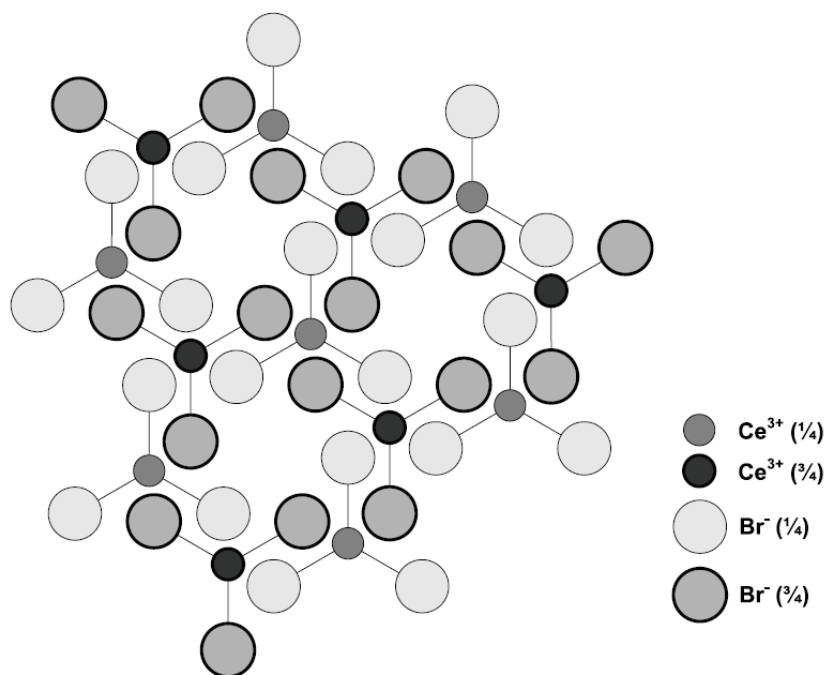


Figure 1.7. Projection of the UCl₃ crystal structure of CeBr₃ [50].

The problems associated with the fragility of the crystal are further compounded by the fact that thermal expansion is highly anisotropic. Along the a -axis, expansion is estimated to occur at 28.1 ppm/°C whereas along the c -axis expansion occurs at a lower rate of 7.5 ppm/°C. Since the growth of these crystals is accomplished through melt growth, the requisite thermal gradients tend to plastically deform the crystal along the prismatic planes if not properly aligned.

CeBr₃ and LaBr₃ are therefore highly susceptible to cracking during crystal growth and subsequent detector fabrication.

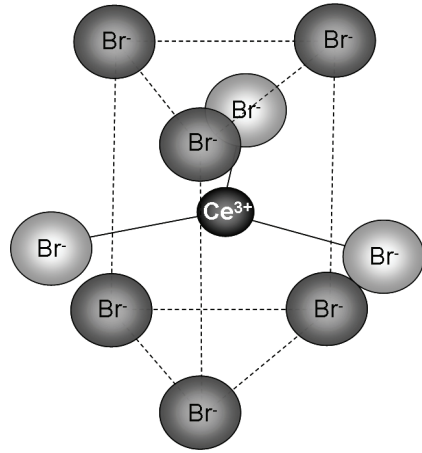


Figure 1.8. UCl₃ building block of CeBr₃.

Plastic deformation of a crystal occurs through the motion of dislocations. Dislocations are basically crystalline imperfections that can glide or climb. A more in-depth discussion of dislocations and their dynamics is provided in Chapter 2. Inhibiting the motion of dislocations is key to strengthening a crystal.

Three methods for inhibiting dislocation motion materials are commonly used [51]. Particle strengthening, in which small particles of another material or phase are introduced into the lattice, relies on the resulting elastic strain around a particle to pin dislocations. Particles in an optical crystal are likely to scatter and/or absorb light though, degrading light transmission and overall scintillation performance. A second method, commonly used in the steel industry, is to mechanically work harden a material. The limited plasticity of CeBr₃ before fracture precludes work hardening however. The third method, solid solution hardening, utilizes the elastic strain and/or electric potential fields around impurity atoms to impede dislocation flow.

Solid solution hardening of ionic crystals through cation replacement can be accomplished in two ways. The first, isovalent alloying, replaces the cation with a like-valence cation of differing ionic radius. For instance, the Ce³⁺ cation in CeBr₃ could be replaced with Y³⁺. A much more potent method is aliovalent alloying, which replaces the cation with one of different valence. In this case, the Ce³⁺ cation could be replaced with Cd²⁺ or Zr⁴⁺. Of the two methods available, aliovalent alloying appears to be advantageous, since much lower levels of

doping are required, and this seems less likely to interfere with the scintillation process. In aliovalent alloys, the doping levels necessary to increase stress strength by an order of magnitude are in the 100 – 500ppm range [52]. Alternatively, substitution levels for an isovalent alloy are on the order of 10 – 30 mol % to achieve the same strengthening effect [53].

Despite requiring three orders of magnitude less dopant to achieve an order of magnitude increase in strength, aliovalent doping of CeBr₃ still poses a serious threat to scintillation performance. The addition of even minute quantities of certain elements can severely degrade or alter scintillation in Ce-activated scintillators. Ce-doped lutetium pyrosilicate (Lu₂Si₂O₇:Ce) is a prime example of such impurity interference with the scintillation process. Lu₂Si₂O₇:Ce scintillates very well when grown by the melting zone technique, but is quenched when grown by the Czochralski method. Further investigation proved that the iridium crucible used during Czochralski growth was the culprit for the quenching. Ir⁴⁺ cations were subsequently introduced into the melt during growth, interfering with the Ce scintillation mechanisms [54]. It is also well known that Ce-doped tungstates and vanadates do not scintillate due to the multiple stable valences of the W and V cations. Indeed, it is generally true that the presence of any cations with multiple stable valences quenches the Ce scintillation mechanisms [44]. Therefore, the strengthening of CeBr₃ through aliovalent doping must be done carefully to ensure the added dopants do not interfere with the scintillation mechanism, either by quenching the light emission process or by re-absorbing the emitting light. Careful selection of dopants though may still prove aliovalent doping to be a promising method for strengthening CeBr₃. A more in depth look at potential candidate dopants is presented in Chapter 4.

Aliovalent doping of an ionic crystal is an extremely ‘potent’ method for strengthening when compared to isovalent alloying. Solid solution strengthening of a crystal lattice can be approximated as

$$\tau = \psi Sc^{1/2} \tag{1.2}$$

for small concentrations of dopant, where τ is the increase in critical resolved shear stress, S is the shear modulus of the host lattice, c is the concentration of dopant solute in atomic fraction, and ψ is a constant of proportionality [51]. The approximation in Eqn. (1.2) is the strengthening effect based on lattice strain due to the dopant cations and does not account for electrical

interactions between aliovalent cations and the surrounding lattice in the case of aliovalent doping. Isovalent dopants introduce spherical strain fields around themselves, while aliovalent dopants cause tetragonal lattice distortions. The constant of proportionality, ψ , for aliovalent doping is typically on the order of unity. In contrast, ψ is in the range of 10^{-4} to 10^{-6} for isovalent doping. As an example, it has been experimentally determined that the addition of ~ 250 ppm of Y^{3+} to CaF_2 increases critical resolved shear stress (CRSS) by an order of magnitude [52], whereas the addition of ~ 20 mol% of KBr is necessary to achieve the same strengthening effect in KCl [53].

1.4 Overview

The Ce-activated lanthanide halide class of scintillators offers substantial performance advantages over conventional scintillator materials such as NaI:Tl. However, the lanthanide halides are brittle materials with low fracture toughness making production of large single crystals difficult and expensive. Adding aliovalent dopants to lanthanide halide scintillators may potentially provide a mechanism to overcoming the obstacles to mass producing large single crystals in a cost-effective manner. A more rugged version of $CeBr_3$ has many potential applications in the γ -ray spectroscopy field, including the medical and defense industries. Stronger, more fracture resistant $CeBr_3$ also implies improved crystal growth yields and subsequently improved availability and cost for implementation. The primary concern in doping a scintillator is the potential impact the dopant has on the performance of the scintillator.

The focus of the following work is on the scintillation effects of aliovalently-doping $CeBr_3$. Various performance metrics were used to determine the overall impact of each dopant on the scintillation characteristics of $CeBr_3$.

Details are given regarding the preparation of aliovalently-doped $CeBr_3$ samples and the performance analysis of each. Chapter 2 discusses the theoretical considerations behind aliovalently-doping $CeBr_3$ and the potential strengthening effects. In Chapter 3, the details of the mechanisms of scintillation, how they apply to $CeBr_3$, and the potential side-effects aliovalent dopants may have on scintillation performance are discussed. In Chapter 4, an outline of the crystal growth and sample preparation procedures used to produce the doped $CeBr_3$ crystals is given as well as a description of the various methods used to benchmark scintillation performance. In Chapter 5, a summary of the scintillation performance measurements conducted

to determine dopant effect on scintillation performance of CeBr_3 is given. Finally in Chapter 6, a discussion regarding the conclusions that can be drawn from the various results is presented.

2 Strengthening of Crystals

Crystals are the ordered arrangement of a basis of atoms into a regular lattice structure. A basis is a set of one or more atoms that constitute a single building block. In a compound such as CeBr_3 , the basis contains an equivalent ratio of atoms as in the chemical formula. Thus, the basis of CeBr_3 is a multiple of the ratio of Ce:Br or 1:3. Due to the arrangement of the CeBr_3 crystal though, the basis contains two Ce atoms and six Br atoms. Figure 2.1 gives an example of one possible basis for CeBr_3 . Replicating a single basis at each lattice point constitutes a crystal.

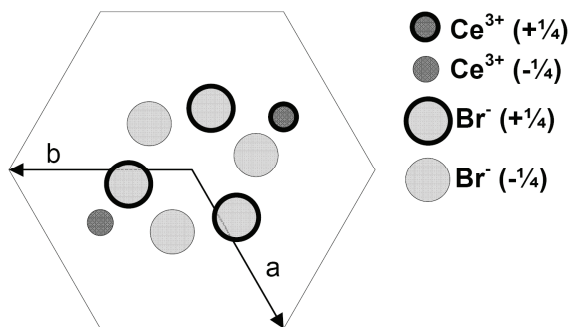


Figure 2.1. Basis of CeBr_3 . The two Ce atoms are offset by $\frac{1}{2}$ lattice parameter in the c -direction (into the paper). Atom positions in the unit cell are given in Table 1.

The locations of the atoms in a basis are referenced to the lattice vectors. For the hexagonal structure of CeBr_3 , two vectors, \vec{a} and \vec{b} , are defined as shown in Figure 2.1. The third vector, \vec{c} , projects perpendicularly into the plane of the paper in Figure 2.1. The atoms comprising the basis of CeBr_3 are located at the positions noted in Table 2.1. In this case, the locations of the Br atoms can be defined in terms of two parameters, x and y , and relationships between them. Table 2.1 also provides the relationships between x and y for each atom of the basis.

The distance from a Ce cation and its nearest coplanar Br anion along the basal plane is 3.15\AA (such as between atom #1 and atom #3 in Table 2.1) while the nearest neighbor is actually 3.07\AA away (atom #1 to atom #8) and is located $\frac{1}{2}\vec{c}$ above or below the Ce ion.

Table 2.1. Positions of Ce and Br atoms in the unit cell. For CeBr_3 , $x \cong 0.39$ and $y \cong 0.30$ [55].

	Atom	Positions		
		\bar{a}	\bar{b}	\bar{c}
Ce	1	1/3	2/3	1/4
	2	-1/3	-2/3	-1/4
Br	3	$x = 0.39$	$y = 0.30$	1/4
	4	$-x = -0.39$	$-y = -0.30$	-1/4
	5	$-y = -0.30$	$x - y = 0.09$	1/4
	6	$y = 0.30$	$y - x = -0.09$	-1/4
	7	$y - x = -0.09$	$-x = -0.39$	1/4
	8	$x - y = 0.09$	$x = 0.39$	-1/4

Arranging the basis in Figure 2.1 into a hexagonal Bravais lattice, as shown in Figure 2.2, with lattice constants of $a = 7.952 \text{ \AA}$ and $c = 4.444 \text{ \AA}$ completes the CeBr_3 structure giving the crystal a mass density of 5.18 g/cm^3 [50]. Distinctive open, hexagonal channels between the Br anions form parallel to the c -axis in this crystal structure. These channels are shown at the center and vertices of the superposed hexagon in Figure 2.2.

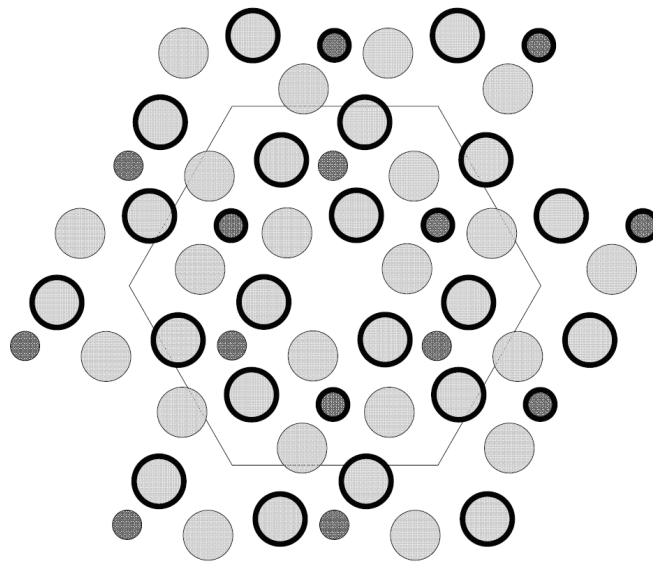


Figure 2.2. [0001] projection of CeBr_3 lattice structure. Shown are seven unit cells arranged in the hexagonal arrangement of the UCl_3 prototype structure. Atom representations are identical to those in Figure 2.1.

Basic solid state theory predicts the bond strengths between the ions in the crystal. However, using these simplistic bond models to predict material strength is misleading, producing estimates of yield stress many orders of magnitude too high. The introduction of the

concept of dislocations, which are crystalline defects, helps to correct these strength estimates. The motion of dislocations through a crystal accounts for the measured decrease in material strength and yielding behavior. Blocking the motion of these naturally occurring dislocations with obstacles is key to increasing strength in a crystalline solid.

Several methods for introducing obstacles to dislocation motion are known, but aliovalent solid solution hardening appears to be most advantageous as discussed in Chapter 1. This hardening method utilizes impurity atoms of differing valence to impede dislocation motion. These aliovalent impurities create strain fields around themselves, effectively pinning nearby dislocations. Thus, when a propagating crack passes near an aliovalent impurity atom, the local stress necessary to continue crack propagation increases considerably. On a whole, aliovalent impurities have been shown to increase the macroscopic critical stress of a material by an order of magnitude [51]. The physical mechanisms behind this phenomenon and their application to strengthening of CeBr_3 are discussed in greater detail in the following sections.

2.1 Bonding

The bonds holding atoms together in a crystal lattice are the sum of several attractive and repulsive forces. The primary forces to consider in an ionic crystal such as CeBr_3 is an electrostatic attraction between oppositely charged ions, repulsion between like-charged ions and a central field repulsion as described by to the Pauli exclusion principal [56].

Consider a one-dimensional lattice of monovalent ions as illustrated in Figure 2.3. Ions of opposite charge attract one another, while like-charged ions repel each other. The bonds shown in Figure 2.3 are simply a first approximation of the total bond structure in a one-dimensional lattice as it only considers the nearest and next nearest neighbor bonds. In reality, third, fourth, fifth, etc. neighbors also contribute to the overall bonding of a crystal. The total bond energy, U_i , of an ion can be represented as a sum of all contributions [56],

$$U_i = \sum U_{ij}, \quad (2.1)$$

where

$$U_{ij} = T \exp\left(\frac{-r_{ij}}{C}\right) \pm \frac{q^2}{4\pi\epsilon_0 r_{ij}} \quad (2.2)$$

is the bond energy between ions i and j . The first term in Eqn. (2.2), $T \exp\left(\frac{-r_{ij}}{C}\right)$, represents the central field repulsive energy between atoms as described by the Pauli exclusion principal. The second term, $\pm \frac{q^2}{4\pi\epsilon_0 r_{ij}}$, is the electrostatic energy between the ions. The electrostatic energy term is positive for like-charged ions and negative for oppositely charged ions. Referring to Figure 2.3, the electrostatic energy term is negative for bonds (a) and positive for bonds (b). In Eqn. (2.2), T and C represent empirical constants that describe the strength and range of the repulsive force respectively. ϵ_0 is the permittivity of vacuum and r_{ij} is the distance between ions i and j .

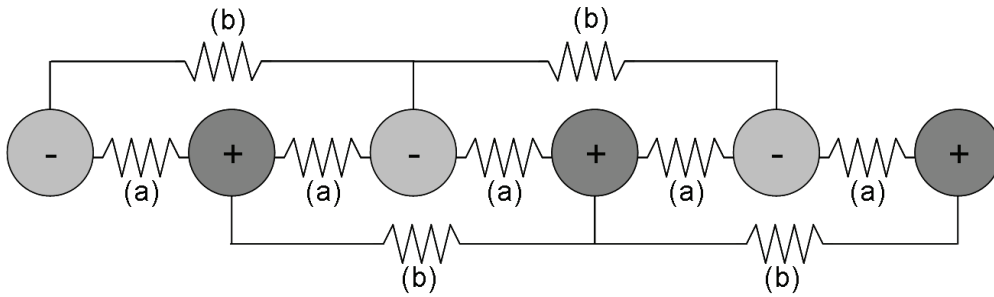


Figure 2.3. One-dimensional lattice of alternating monovalent cations and anions. Bonds (a) are attractive while bonds (b) are repulsive.

Assuming only the bonds between the first two neighboring ions are important, the total bond energy for a binary compound can be expressed as

$$U_{tot} = ZT \exp\left(-\frac{R}{C}\right) - \frac{\alpha(n_1 + n_2)z_1 z_2 q^2}{4\pi\epsilon_0 R} \quad (2.3)$$

where Z is the number of nearest neighbor ions, z_1 and z_2 are the charges of the two ions, n_1 and n_2 are the stoichiometry of the binary compound and α is the Madelung constant for the lattice

[57]. In Eqn. (2.3), the substitution $r_{ij} = Rp_{ij}$ was made for simplicity. R represents the distance between nearest neighbors.

As an example, sodium chloride (NaCl) arranges in a cubic structure and has a Madelung constant of $\alpha = 1.747565$ [56]. The empirical repulsion parameters for NaCl have been determined to be $ZT = 1.05 \times 10^{-8}$ ergs and $C = 0.321 \text{ \AA}$ [56]. Plotting the crystal energy against atom separation distance, R , produces the responses shown in Figure 2.4. Note that a minimum in total energy occurs at $R_0 = 2.815 \text{ \AA}$, which is near the experimentally verified atom separation distance (2.820 \AA) in NaCl at absolute zero temperature.

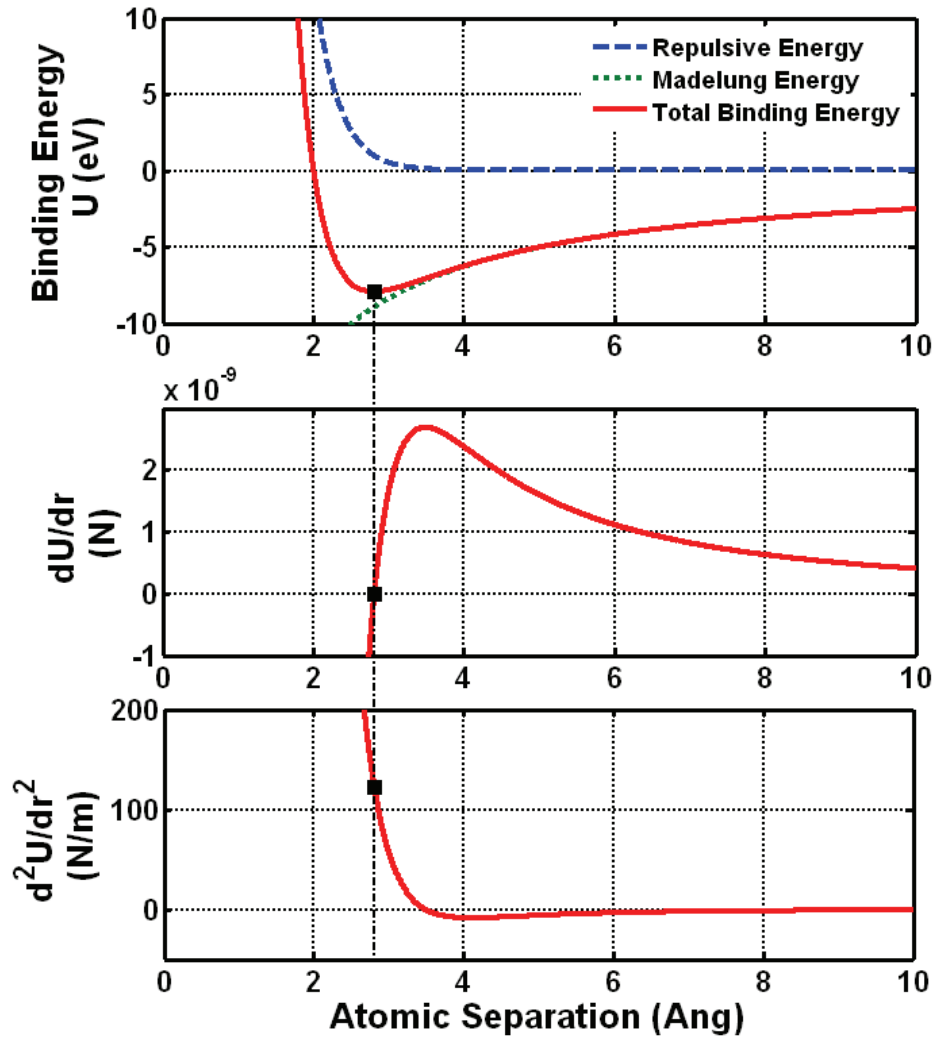


Figure 2.4. Plot of the repulsive, Madelung and total energies of NaCl for different atom separation distances (top), the first differential of the total binding energy (middle) and the second differential of the total binding energy (bottom). The black squares indicate the values of each at equilibrium separation.

The bulk modulus B for a rock salt structure is calculated as [57]

$$B = -\frac{1}{18R} \left. \frac{d^2U}{dR^2} \right|_{R=R_0}. \quad (2.4)$$

Performing the differentiation on Eqn. (2.4), the bulk modulus of NaCl is predicted to be 24.1GPa agreeing quite well with observations of 24.4GPa [58]. Further, by assuming Poisson's ratio for NaCl to be $\nu = 0.228$ [58], the shear modulus S and Young's modulus E are predicted by the relations

$$S = \frac{3B(1-2\nu)}{2(1+2\nu)} \quad (2.5)$$

and

$$E = \frac{3B(1+\nu)(1-2\nu)}{(1+2\nu)}. \quad (2.6)$$

for an isotropic crystal [59]. Poisson's ratio describes lateral strain as a fraction of the longitudinal strain for a given material when under linear elastic strain conditions. Inserting B and ν values, $S = 11.9$ GPa and $E = 29.9$ GPa. Experimentally determined values, $S = 12.6$ GPa and $E = 40.0$ GPa, are also in reasonable agreement [60]. Thus, it seems elastic behavior is well predicted by the atomistic models of the bond energies. However, as will be shown in the next section, simple theoretical models predict yield strengths many orders of magnitude too high.

2.2 Dislocations

Dislocations, originally independently proposed in 1934 by Taylor, Orowan, and Polanyi to explain the discrepancy between theoretical crystal strength and experimentally measured values [61-63], are key to describing plastic deformation in crystals. Prior to the introduction to the concept of dislocations, Frenkel proposed a method to predict the critical shear stress by first assuming plastic deformation occurred when a plane of atoms glided over an adjacent plane from

one position of equilibrium to the next [63]. Figure 2.5 provides a one-dimensional case in which a line of atoms is forced to glide to the right by one lattice position. Frenkel assumed the force necessary to perform this motion was sinusoidal by nature since the force at the midpoint of motion (Figure 2.5b) should be zero because the attractive forces to the original position and the new position would be balanced. Beyond the midpoint, the force would become negative as the atoms became preferentially attracted to the new position (Figure 2.5c)

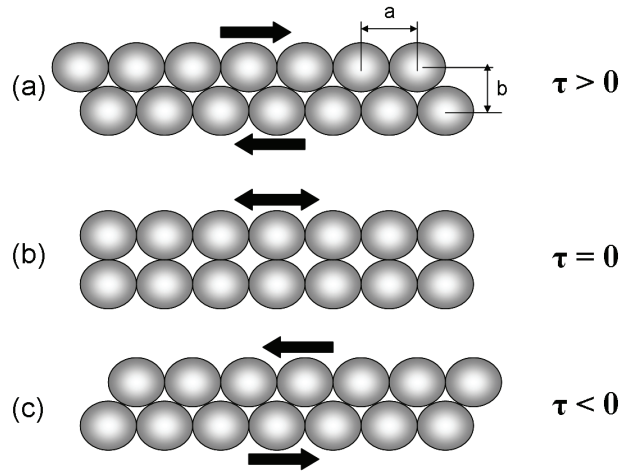


Figure 2.5. Illustration depicting the process Frenkel assumed responsible for plastic deformation. (a) A shearing force ($F > 0$) is applied. The top row of atoms then glide to the midpoint (b) where applied force is zero. After the midpoint, attractive forces take over in (c). To maintain position a negative force must be applied.

The shearing force τ required to perform the motion in Figure 2.5 was assumed to have the form [64]

$$\tau = \frac{SD}{2\pi a} \sin\left(\frac{2\pi x}{D}\right), \quad (2.7)$$

where a is the distance between planes, and D is the atom separation. Therefore, the critical shear stress to plastically deform a crystal with $a \approx D$ is simply

$$\tau_c = \frac{S}{2\pi}. \quad (2.8)$$

Using the predicted values from the previous section, NaCl should exhibit a critical shear stress of $\tau_c = 2.0$ GPa. However, measurements indicated that the actual critical shear stress of NaCl is closer to 0.4 MPa or about 5,000 times smaller [60]. From this result, Frenkel's theory appears to lack the sophistication to describe plastic deformation.

Taylor, Orowan and Polanyi postulated that the presence of crystalline defects or dislocations in real crystals reduced the observed critical shear stress considerably. To illustrate, consider a cubic crystal lattice with a line defect as illustrated in Figure 2.6. The line defect appears as an added half plane in Figure 2.6. When shear is applied, the added half plane or edge dislocation effectively moves in the direction of the shearing force. This mechanism of dislocation motion is called glide. In this manner, plastic deformation occurs as a sequence of bonds breaking and reforming consecutively, rather than simultaneously as Frenkel suggested. The force required to break a single bond one at a time is far less than that required to break all bonds simultaneously.

A model describing the critical stress involved in laterally moving an edge dislocation was proposed by Peierls and later modified by Nabarro [65,66],

$$\tau_f = S \exp\left(\frac{-2\pi w}{a}\right), \quad (2.9)$$

in which τ_f is the 'Peierls' or 'frictional' stress, a is the distance between the translating planes and w is a value characteristic of the size of the dislocation. A 'narrow' dislocation is one in which the atomic distortion around the dislocation is located only in the immediate vicinity of the edge dislocation and has a width w of just a few lattice constants a . A 'wide' dislocation, on the other hand, has a value of w of many lattice constants. For NaCl, an ionic solid in which dislocations are generally narrow, w takes on a value of approximately $1.6a$ in order to match the observed critical resolved shear stress.

Two general types of dislocations are typically defined, those being edge dislocations, as illustrated in Figure 2.6, and screw dislocations as illustrated in Figure 2.7. Screw dislocations are helical distortions in the lattice about a central axis. Much like an edge dislocation, a screw dislocation facilitates shear by moving stepwise. However, a screw dislocation moves perpendicular to the applied stress unlike the edge dislocation which moves parallel to the stress

vector. Rarely is a dislocation purely edge or screw though. Rather, dislocations appearing in real crystals are often a combination of the two types.

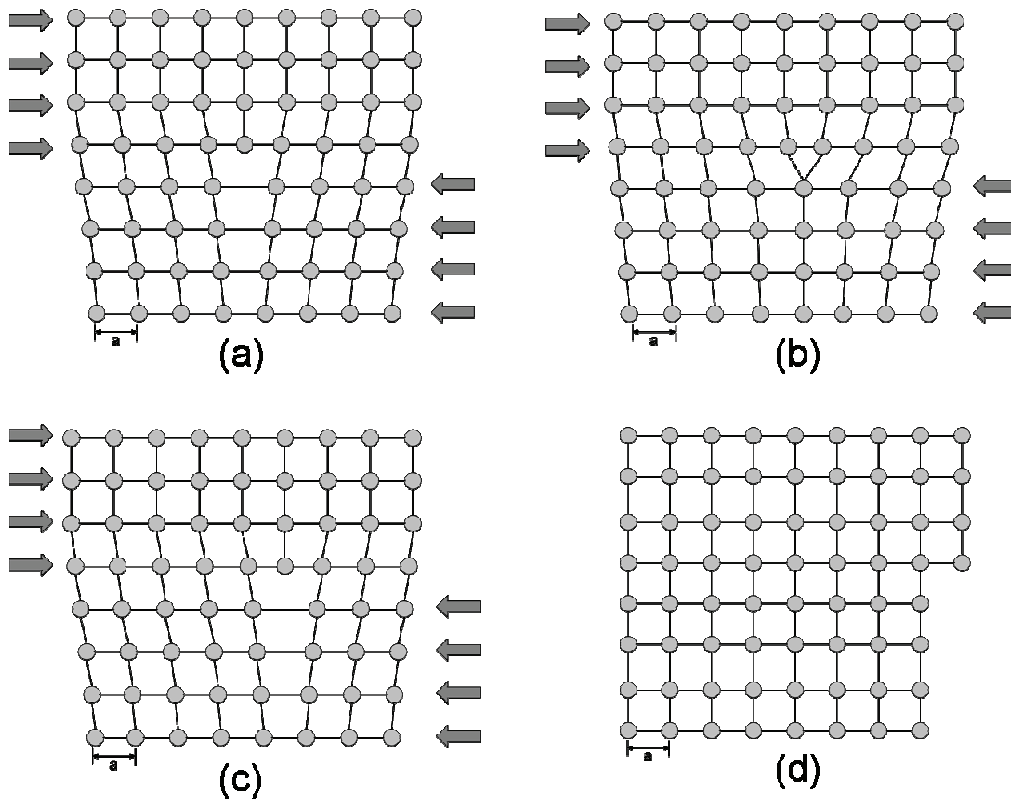


Figure 2.6. Dislocation glide. (a) A half plane defect is present in the crystal. (b) An applied shear causes the bonds at the termination of the half plane to switch to the next adjacent plane. (c) The half plane has effectively moved to the right by one lattice spacing. (d) Continued movement of the half plane results in the half plane terminating at the right surface and a plastic deformation of a .

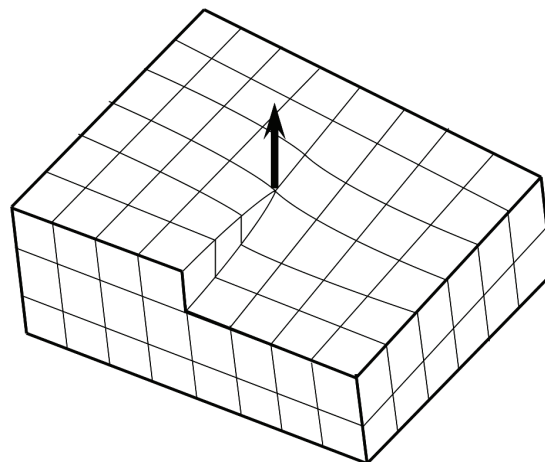


Figure 2.7. Screw dislocation in a cubic lattice. Screw axis is denoted by the arrow.

2.2.1 Stress Fields

Dislocations produce stress and strain fields in the distorted lattice nearby. Since the motion of dislocations is a result of the sum of all stresses, both externally applied and internally generated, it is important to understand the nature of these self-generated stress fields. “Core” stresses, those very near the dislocation, are difficult to accurately predict as they require detailed knowledge of the bonding, crystal structure, and the nature of the dislocation [51]. Fortunately, these short-range stresses play a relatively unimportant role in the motion of dislocations. Long-range stresses, on the other hand, are quite simple to calculate using elasticity theory and are the dominant force in determining dislocation motion.

Screw dislocations produce only shear stresses and, thus, are the easiest to describe. The shear stress, τ , as a function of radial distance, r , from the center of a screw dislocation is described as [51]

$$\tau = \frac{S|\bar{B}|}{2\pi r} \quad (2.10)$$

where $|\bar{B}|$ is the magnitude of the Burger’s vector for the dislocation.

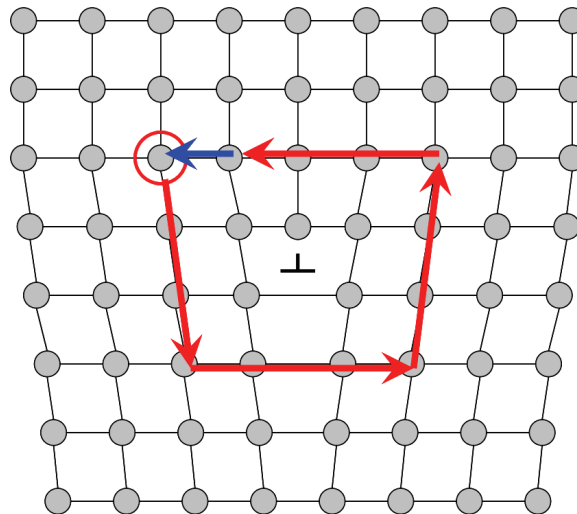


Figure 2.8. Determining the Burger’s vector for a dislocation. The additional vector needed to close the loop (blue) is the unique Burger’s vector for the dislocation. Here, the Burger’s vector has a length of one lattice constant and points left.

Burger's vector is a unique descriptor of a dislocation. It is found by starting at a lattice position near a dislocation and taking equal lattice steps around the dislocation. Figure 2.8 illustrates this method for an edge dislocation. In the case shown in Figure 2.8, start at the lattice position at the upper left and move four lattice positions in each direction around the dislocation. The vector required to close the loop, shown in blue in Figure 2.8, is then the Burger's vector.

Edge dislocations produce both shear and dilational stresses though. Describing the stress field around an edge dislocation requires four values, dilational stresses in the x-, y-, and z- directions ($\sigma_x, \sigma_y, \sigma_z$) as well as a shear stress in the xy-plane (τ_{xy}) since no shear stress is developed in the z-direction. For a pure edge dislocation, these values are described by the following relationships [51]

$$\sigma_x = \frac{-S|\bar{B}|}{2\pi(1-\nu)r} \sin \Theta [2 + \cos 2\Theta], \quad (2.11a)$$

$$\sigma_y = \frac{-S|\bar{B}|}{2\pi(1-\nu)r} \sin \Theta \cos 2\Theta, \quad (2.11b)$$

$$\sigma_z = \frac{-S|\bar{B}|\nu}{\pi(1-\nu)r} \sin \Theta, \quad (2.11c)$$

$$\tau_{xy} = \frac{S|\bar{B}|}{2\pi(1-\nu)r} \cos \Theta \cos 2\Theta, \quad (2.11d)$$

where r and Θ are as described in Figure 2.9 and ν is Poisson's ratio.

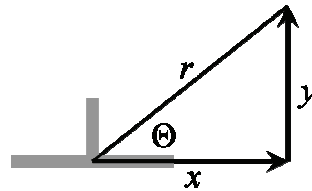


Figure 2.9. Definition of terms used in Eqn. (2.11). The gray symbol (\perp) represents an edge dislocation running perpendicular to the plane of the paper with the added half plane of atoms above the origin.

2.2.2 Dislocation Energies

The elastic strain of bonds around a dislocation has an energy associated with it and bears important consequences upon the dynamics of crystals as a whole. Edge and screw dislocations are line defects, so their related energies are often calculated as a function of unit length and thus have units of force, typically referred to as “line tension”.

Shear strain about a screw dislocation is described by [51]

$$\gamma = \frac{|\bar{B}|}{2\pi r}. \quad (2.12)$$

Since the energy associated with shear stress is described by the integral

$$U_\gamma = \int \tau d\gamma \quad (2.13)$$

and

$$\tau = S\gamma, \quad (2.14)$$

the total energy per unit length associated with a screw dislocation becomes [51]

$$U_\gamma = \frac{S\gamma^2}{2}. \quad (2.15)$$

Therefore, for a differential volume element dr at r , the differential elastic strain energy dU'_s is [51]

$$dU'_s = 2\pi l dr \left(\frac{S|\bar{B}|^2}{8\pi^2 r^2} \right) = \frac{S|\bar{B}|^2 l}{4\pi} \frac{dr}{r}. \quad (2.16)$$

Integrating Eqn. (2.16) from $r = r_0$ to $r = r_1$, the energy per unit length of a screw dislocation is

$$U_s = \frac{U'_s}{l} = \frac{S|\bar{B}|^2}{4\pi} \ln\left(\frac{r_1}{r_0}\right) \quad (2.17)$$

where r_0 is the dislocation core radius and r_1 is some radius at which other dislocation energies dominate or the crystal edge, whichever is smaller. Typically, r_1 is microscopic. Often, Eqn. (2.17) is approximated as [51]

$$U_s \cong \frac{1}{2} S|\bar{B}|^2. \quad (2.18)$$

Following a similar derivation for edge dislocations, the energy per unit length for an edge dislocation is [51]

$$U_e \cong \frac{S|\bar{B}|^2}{2(1-\nu)}. \quad (2.19)$$

Ultimately, the energy of a dislocation is heavily dependent upon the Burger's vector magnitude, $|\bar{B}|$, and that slip directions are commonly closely-packed ones. Also, it would be expected that screw dislocations tend to form parallel to a closely-packed plane, while edge dislocations tend to preferentially form perpendicular to closely-packed planes as these orientations require less energy ($|\bar{B}|$ is smaller in these orientations).

As dislocations translate through a lattice under an applied shearing force such as encountered during plastic deformation, the dislocations often encounter obstacles, such as impurity atoms, secondary phase particles, or other dislocations. These obstacles pin the dislocation at a single point, forcing the dislocation to bow out as illustrated in Figure 2.10.

An obstacle to dislocation motion increases the energy required to plastically deform the material due to the increase in dislocation length and, thus, the associated total dislocation elastic strain energy. The fact that an obstacle increases the length of a dislocation can be observed quite simply in comparing the length of the dislocation in Figure 2.10a to that in Figure 2.10c.

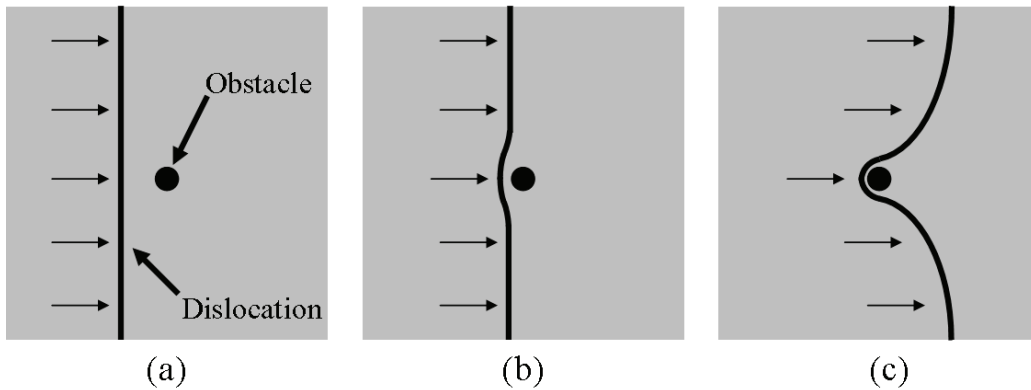


Figure 2.10. Dislocation translating through a medium (a) encounters an obstacle at (b) and begins to bow around the obstacle (c).

Continuing shear strain, a dislocation eventually overcomes an obstacle when some critical ‘breaking angle’, φ_c , is reached [67], where φ is defined as shown in Figure 2.11. The magnitude of φ_c determines whether the obstacle is considered ‘weak’ or ‘strong’. A strong obstacle is generally considered to be one in which the critical breaking angle is less than 100° .

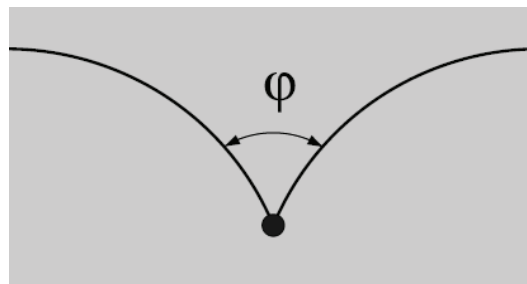


Figure 2.11. Visual representation of φ as the angle the bowing dislocation makes with itself.

The amount of shear stress required to move a dislocation past strong obstacles with effective spacing L' is approximated as

$$\tau \cong \frac{S|\bar{B}|}{L'} \cos \frac{\varphi_c}{2}. \quad (2.20)$$

Maximum stress is required when $\varphi_c = 0$ and $L' = L$. For very strong obstacles, φ_c approaches zero and the effective spacing L' approaches L , the average spacing between obstacles on the slip plane. Very weak obstacles, on the other hand, have breaking angles approaching 180° and very large effective spacings. In the weak obstacle limit, L' approaches the distance between two obstacles intersecting a random line drawn in the slip plane.

2.2.3 Critical Resolved Shear Stress

Before continuing, it is important to review the basic concept of resolved shear stress. Single crystals exhibit slip in specific crystallographic directions on specific planes, thus it is important to resolve applied forces onto these ‘weakest links’.

Given a sample with cross-sectional area A_0 and applied force F as shown in Figure 2.12, the force acting in the slip direction is [51]

$$F_s = F \cos \delta \quad . \quad (2.21)$$

F_s acts over the resolved area A_s , so the resolved shear stress becomes

$$\tau_{RSS} = \frac{F_s}{A_s} = \frac{F \cos \delta}{A_0 / \cos \theta} = \frac{F}{A_0} \cos \theta \cos \delta \quad . \quad (2.22)$$

Letting

$$m = \frac{1}{\cos \theta \cos \delta} \quad , \quad (2.23)$$

and recognizing $\sigma = F/A$, Eqn. (2.22) simplifies to

$$\tau_{RSS} = \frac{\sigma}{m} \quad . \quad (2.24)$$

Slip will occur in a shearing fashion anytime the applied stress is great enough to cause the resolved shear stress to reach its critical resolved shear stress (CRSS) value, τ_{CRSS} . CRSS is an oft used parameter in gauging material strength and will be referred to quite frequently in later sections.

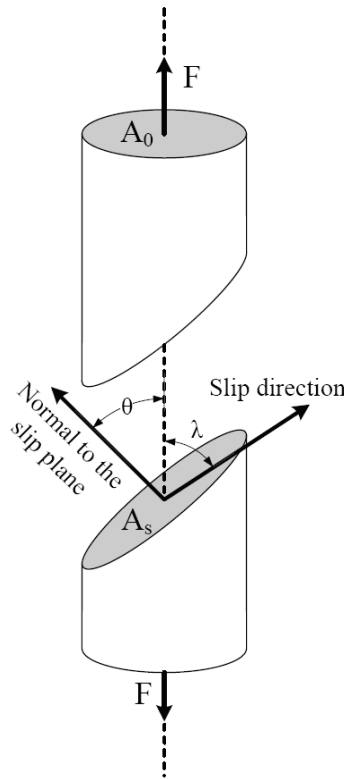


Figure 2.12. Resolving an applied dilational stress into a specific slip direction on a specific crystallographic plane of a single crystal.

2.3 Strengthening Methods

Numerous methods are known for strengthening materials, most of which apply mainly to metals where plasticity is not nearly as limited and other structural materials, such as composites or polycrystalline ceramics. Ionic single crystals, though, have only a few available methods, including precipitate hardening and solid solution hardening [51]. Either method effectively introduces obstacles to the path of dislocations to increase the CRSS of the matrix. Second-phase precipitates are undesirable in optical materials such as scintillators though, as they may scatter and/or absorb light. Solid solution hardening, on the other hand, relies on individual “impurity” atoms to halt dislocation motion. Neglecting possible interferences with

the radiative decay process in these scintillators, the impurity atoms seem less likely to interfere with the photon propagation process.

Solid solution hardening techniques can be broken into two broad categories, isovalent alloying and aliovalent doping. Isovalent alloying involves replacing either the cation or anion with a like-valence ion. Size differences between the solvent and solute atoms create lattice strains which help to pin dislocations. It is important to note that since size differences between solute and solvent are important to the strengthening process, adding CeBr₃ to LaBr₃ does very little to strengthen LaBr₃ as Ce and La cations are very similar in size. The local, spherically-symmetric strain fields around the solute atoms are considered ‘soft’ obstacles to dislocation motion because thermal energies are great enough to aid a dislocation in overcoming the barrier. Estimates place their critical breaking angle, φ_c , near 179° [51]. Thus, isovalent alloying often requires solute addition on the order of 50% to achieve considerable strengthening. At these high levels of alloying, band gap energies are likely to be changed, thus affecting the radioluminescence emission spectrum, a potentially deleterious side-effect for scintillators. An example of isovalent alloying in CeBr₃ might be to replace a portion of the Ce³⁺ cations with Y³⁺ cations.

Alternatively, aliovalent doping requires doping levels on the order of 500ppm to achieve the same strengthening effect. The strain fields generated around an aliovalent impurity atom are tetragonal and considered to be ‘hard’ barriers to dislocation motion. The critical breaking angle around a tetragonal distortion has been estimated to be between 157° and 169° [51]. Further, the low levels of doping are less likely to interfere with the scintillation process. An example of aliovalent doping would be to add a small amount (<1000ppm) of ZrBr₄ to CeBr₃. In other materials, aliovalent doping on the order of 100 – 500ppm, such as Y³⁺ in CaF₂, can increase the CRSS by an order of magnitude [52].

The effective spacing in a slip plane for tetragonal distortions is estimated as

$$L' = \frac{D}{\sqrt{2c}}, \quad (2.25)$$

but is much greater for spherical distortions, estimated to be

$$L' = \frac{D}{\sqrt{c(\pi - \varphi_c)}} \quad (2.26)$$

where $(\pi - \varphi_c)$ is near 1° . Here, c is the concentration of impurity atoms. Recalling Eqn. (2.20), the shear strengthening due to tetragonal defects is

$$\tau_{TET} = Sc^{1/2} \left[\sqrt{2} \cos\left(\frac{\varphi_c}{2}\right) \right] = \chi_{TET} Sc^{1/2} \quad (2.27)$$

and is

$$\tau_{SPH} = Sc^{1/2} \left[\sqrt{(\pi - \varphi_c)} \cos\left(\frac{\varphi_c}{2}\right) \right] = \chi_{SPH} Sc^{1/2} \quad (2.28)$$

for spherical distortions. Using the above estimates for critical breaking angles, it might be expected that $0.14 \leq \chi_{TET} \leq 0.28$, while $\chi_{SPH} \approx 6 \times 10^{-4}$. Therefore, aliovalent doping is far more ‘potent’ in that the same amount of dopant achieves as a far greater strengthening effect. In general, the CRSS of aliovalently-doped crystals exhibit a $c^{1/2}$ dependency up to the solubility limits of the lattice. Beyond the solubility limit of the solvent host, the solute begins to form precipitates, which exhibits a different (and more complex) strengthening behavior.

2.4 Fracture of Single Crystals

One basic approach to calculating the fracture stress of a crystal would be estimate the force necessary to sever every bond across a plane of atoms simultaneously. Of course, this simplistic viewpoint is idealistic and this mechanism of fracture is not observed in nature. Instead, fracture occurs through the propagation of a preexisting crack through the bulk to the surfaces. Propagation of a crack requires far less force than the simultaneous breaking of all bonds since the crack acts to concentrate stress at its tip. Figure 2.13 illustrates a crack of length d propagating through a medium. At the leading tip of the crack, the material undergoes severe

elastic strain and even plastic deformation in the case of metals. Brittle, ionic solids like CeBr_3 , however, do not undergo any appreciable plastic strain before fracture.

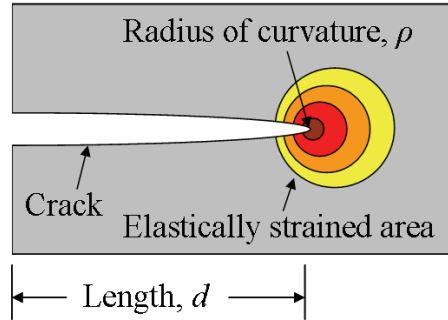


Figure 2.13. Stress concentrating at the leading tip of a crack.

The maximum stress occurs at the tip of the crack, approximated as being elliptically-shaped, and is

$$\sigma_{\max} \cong 2\sigma \left(\frac{d}{\rho} \right)^{1/2} \quad (2.29)$$

where σ is the nominally applied stress. Rearranging Eqn. (2.24) for CRSS,

$$\sigma_C = m \tau_{CRSS} \quad (2.30)$$

to find a condition for critical stress as related to CRSS. When σ_{\max} exceeds σ_C , the crack propagates. A relation can now be drawn between CRSS and the applied stress necessary to propagate a crack, i.e. fracture the solid,

$$\sigma_F \geq \frac{1}{2} m \tau_{CRSS} \left(\frac{\rho}{d} \right)^{1/2}. \quad (2.31)$$

Fracture toughness, K_C , is a parameter often used to describe how resistant a material is to fracture and is defined in the equation

$$\sigma_F = \frac{K_c}{(\pi d)^{1/2}}, \quad (2.32)$$

where $K_c = \sigma\sqrt{\pi d}$ which is simply nominal stress multiplied by the square root of crack length and a constant of proportionality, $\sqrt{\pi}$. Equating Eqn. (2.31) and Eqn. (2.32), it is found that

$$K_c = \frac{1}{2} m \tau_{CRSS} \sqrt{\pi \vartheta}. \quad (2.33)$$

Substituting Eqn. (1.2) into Eqn. (2.33),

$$K_c = \frac{1}{2} \psi S m \sqrt{\pi \vartheta} \cdot c^{1/2}, \quad (2.34)$$

which states that $K_c \propto c^{1/2}$ just as was shown for CRSS in Eqns. (2.27) and (2.28).

It is important to note that the above derivation applies only to solids in which plastic deformation at the crack tip is negligible during fracture as is exhibited by brittle, ionic solids. Further, the derivation is only applicable if the mode of fracture, slip direction and slip plane are not changed by the addition of the dopant atoms. Nevertheless, the result is important in that it clearly predicts an increase in both CRSS and fracture toughness as the square root increase in concentration of aliovalent dopant up to the solubility limit.

3 Scintillation

The physical mechanisms involved in the phenomenon of scintillation are actually quite complex and not entirely understood, but can be broken into five basic stages [7]:

1. Absorption of an ionizing radiation quantum and primary electron-hole formation.
2. Primary electron-hole relaxation, production of secondary electrons.
3. Thermalization.
4. Migration to luminescence centers.
5. Radiative relaxation/light emission.

Each step of the process has numerous branches concerning the energy conversions and losses. A brief overview of the more important processes is provided in the following sections followed by short discussions of the overall scintillation kinetics concerning time response, emission spectra, and proportionality of response.

3.1 Primary Electron-Hole Formation

Primary electrons and holes form when an energetic photon, such as an X-ray or γ -ray, transfers some or all of its energy to an electron within a scintillation medium. Typically, an interaction occurs in one of three common ways, photoelectric absorption, Compton scattering, and electron-positron pair production. Many other interactions occur, but are not considered here as they are unimportant for the purposes of this work. Photoelectric absorption is the dominate interaction for low energy photons.

In a photoelectric event, all the photon energy is imparted onto an electron. Compton scattering, on the other hand, cannot transfer all of the photon momentum to the electron. Rather, the photon transfers only a portion of its energy to the electron in an elastic collision which subsequently alters the scattered photon direction of travel. Pair production occurs when a photon interacts with the Coulombic field around a nucleus of an atom, creating an electron and a positron. The electron-positron pair with a threshold energy of 1.022MeV, rest mass of an

electron and positron, share the remaining energy of the photon as kinetic energy. Thus, if a 2MeV γ -ray were to interact with a nucleus and produce an electron-positron pair, the electron and positron would share the remaining 0.978MeV of energy, split almost equally between them. Pair production does not occur below 1.022MeV, but is the dominate form of interaction at high photon energies. The energetic positron will eventually lose its kinetic energy and annihilate with an electron, producing two 511keV annihilation photons. Depending on the location of annihilation and the size of the detector, these 511keV photons may subsequently interact either by Compton scattering, photoelectric absorption or escape the device.

Ultimately, however, these three interaction mechanisms act to impart kinetic energy to a bound electron. The resulting energetic electron is then ejected from its bound energy state into upper energy bands in the crystal, leaving behind a “hole”. A hole is the absence of the electron, an empty energy state normally occupied by an electron. Since a hole behaves much like a particle in its de-excitation, it is treated conceptually as a particle having a positive elementary charge in many cases. Consequently, the interaction of a quantum of radiation with a bound electron forms a highly energetic primary electron-hole pair.

3.2 Secondary Electron-Hole Formation

The second stage of the scintillation phenomenon is the most complex. Essentially, this stage is the transfer of energy from the primary electron and hole to other electrons in the medium, producing a number of secondary electrons and holes. Primary holes relax via one of two primary modes, radiatively and non-radiatively. The radiative relaxation of the hole, which is generally less likely than non-radiative relaxation, results in the emission of X-rays as outer shell electrons drop into empty energy states in the inner electron shells around the ionized atom. Non-radiative relaxation, as illustrated in Figure 3.1, occurs via the Auger effect in which an outer shell electron is ejected when an outer shell electron moves to fill the inner shell primary hole. The transition energy gained by the outer shell electron dropping into an inner shell is imparted to another outer shell electron, which subsequently ejects it from the outer shell into the conduction band. The Auger process thus results in two lower energy holes and an energetic secondary electron from a single high energy hole.

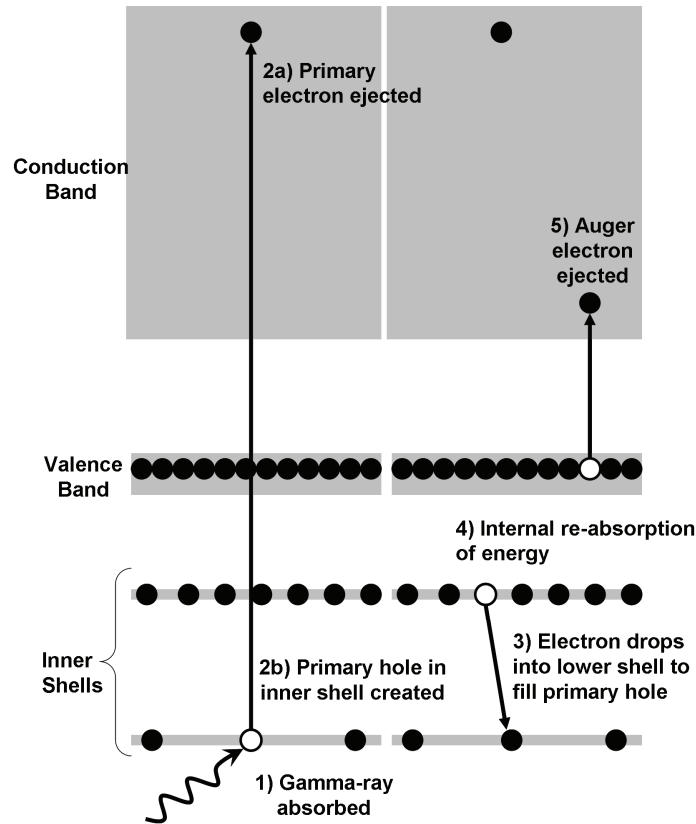


Figure 3.1. Illustration of primary hole relaxation through the Auger effect. A primary electron and hole are created when an inner shell electron absorbs a γ -ray. The primary hole is subsequently filled by a higher shell electron. The energy gained in transitioning the electron from an upper shell to a lower shell is re-absorbed internally and thus ejects a valence electron into the conduction band.

Primary electrons, on the other hand, relax by creating plasmons and inelastically scattering off other electrons [7]. Plasmons are the longitudinal oscillations of charge density of the valence electrons left in the wake of an energetic electron passing through a lattice, much like the wake left behind a boat. Plasmons typically have energies on the order of 10 – 20eV and decay into electron-hole pairs. Inelastic scattering of high energy electrons directly ionizes an atom to produce an energetic electron-hole pair. These relaxation mechanisms continue until all electrons and holes have energies below the ionization threshold energy, E_t , of the material. For ionic materials, the ionization threshold energy is approximately $E_t \approx \left(\frac{9}{7}\right)E_g$ [7]. Electrons with energy greater than E_t lose energy by generating lattice vibrations known as phonons. This loss of energy is therefore reflected in the fact that the ionization threshold energy is greater than the band gap energy.

3.3 Thermalization

The thermalization of the secondary electrons and holes is how much of the original energy is 'lost', or rather, converted to a form not useful for detection purposes. The generation of phonons is the key thermalization process which converts a portion of the kinetic energy of the secondary electrons and holes to lattice vibrations or heat. Conversion of energy to phonons is a direct energy loss mechanism, which is unfortunately unavoidable and deleterious to the light yield. Estimates of energy lost to phonon generation are in the range of 30% for ionic crystals [7].

3.4 Migration and Light Emission

Electrons and holes after thermalization, located at the bottom of the conduction band and the top of the valence band respectively, diffuse through the lattice where they can interact with defects, impurities, activator atoms and each other. Electrons can be removed from the conduction band in a number of ways. For sufficiently dense ionization, recombination of electrons with holes is a detrimental effect often encountered when detecting heavy charged particles. Capture by impurity traps in the energy band gap can remove electrons from the scintillation process, but can also simply slow the process if the electron traps are shallow. Electrons trapped in shallow energy levels can de-trap and re-enter the scintillation process. De-trapping though can be a rather slow process, producing undesirable afterglow effects. Forming immobile F centers with an anion vacancy is another mechanism by which electrons are removed from the scintillation process. Anion vacancies act as effective capture centers for electrons. When an anion vacancy traps an electron within it, the stable complex is called an F center.

Holes can also undergo capture by impurity traps and be effectively removed from the scintillation process much like electrons. A hole can become bound between two anions to form what is known as a V_k center or self-trapped hole (STH). Unlike the F center, V_k centers are somewhat mobile at room temperature, exhibiting a sort of hopping motion. V_k centers are generally the dominate state holes occupy given the fact that formation of V_k centers only requires on the order of 10^{-11} s or 10^{-12} s, many orders of magnitude less time than the lifetime of a free hole. V_k centers can also go on to trap free electrons to form self-trapped excitons (STE). Approximately 10^{-10} s after the creation of the primary electron and hole, an ionic scintillator contains a number of free electrons, V_k centers, and STEs. Figure 3.2 below illustrates the

processes described above for electrons and holes following thermalization and prior to luminescence center excitation.

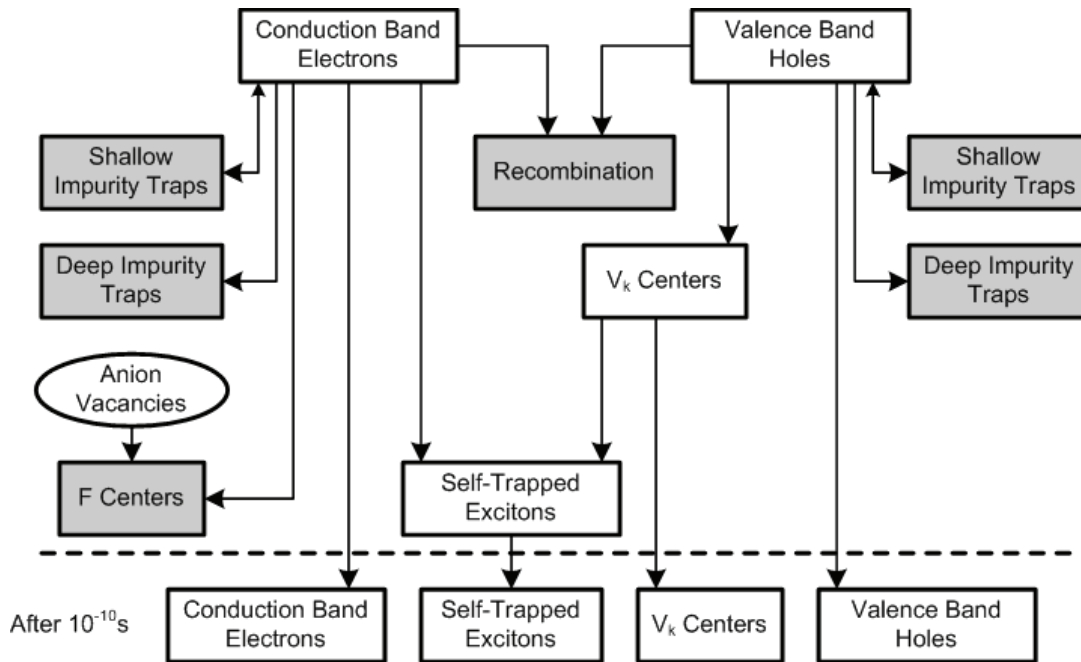


Figure 3.2. Flow diagram of the processes thermalized electrons and holes undergo during the migration stage of scintillation. Blocks in gray indicate those final states in which energy is lost from the scintillation process.

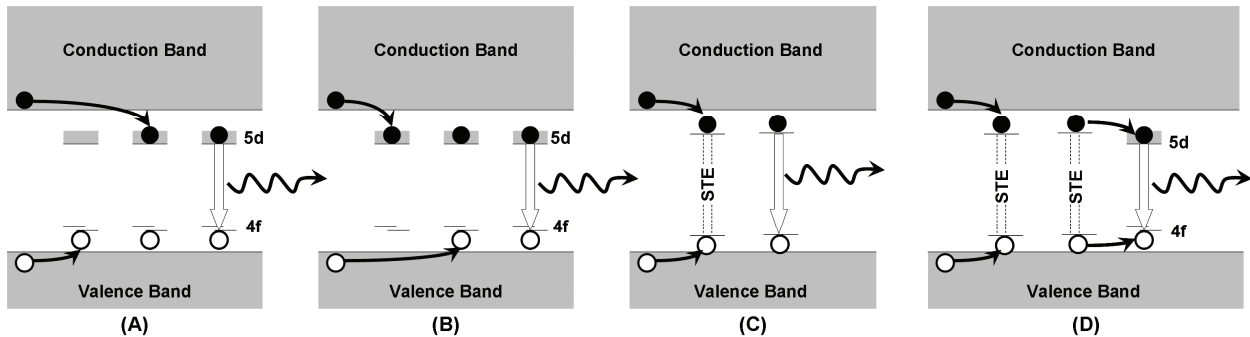


Figure 3.3. Mechanisms of radiative decay in Ce³⁺-activated compounds. (A) Ce³⁺ ion captures a hole (or V_k center) to become Ce⁴⁺. Ce⁴⁺ next captures an electron to become an excited Ce³⁺ ion. The excited Ce³⁺ ion subsequently decays to its ground state via the 5d-4f transition and emits a scintillation photon. (B) A Ce³⁺ ion captures an electron, then a hole (or V_k center) before decaying to its ground state. (C) A V_k center traps an electron to form a self-trapped exciton (STE). The STE then directly decays radiatively before migrating to a Ce³⁺ luminescence center. (D) An STE migrates to a Ce³⁺ luminescence center and transfers its energy to the Ce³⁺ ion. The Ce³⁺ ion then radiatively decays to its ground state.

During the migration stage of the scintillation process, the excited particles (free electrons, free holes, V_k centers and STEs) migrate to luminescence centers, exciting them. The luminescence centers may first capture a hole followed by an electron, vice versa or directly capture an exciton to become excited as shown in Figure 3.3A, Figure 3.3B and Figure 3.3D respectively. STEs may also directly de-excite to emit scintillation photons as shown in Figure 3.3C. However, STEs are relatively long lived so decay quite slowly.

3.5 Characterization and Performance

Production of scintillation light is to a first approximation proportional to the energy deposited in the primary electron and hole, which is the key reason scintillators have been employed as γ -ray spectrometers since 1948. Of course, statistical fluctuations and nonlinearities of light yield within the scintillation medium exist and are deleterious to spectroscopic performance. The efficiency and speed of energy conversion to scintillation light is also a key factor in determining overall scintillator performance.

3.5.1 Radioluminescence Spectrum

The emission spectrum of a scintillator is an important feature when considering its performance potential in spectroscopic applications. The light emitted by a scintillator must be accurately and efficiently quantified to achieve high energy resolution. Typical scintillator systems utilize a photomultiplier tube (PMT) or some sort of photodiode (PD) to convert scintillation light to an electrical signal. Since these light conversion devices are not uniformly sensitive to all wavelengths of light, it is important that the emission spectrum emitted by a scintillator match well with the spectral sensitivity of an available PMT or PD to achieve high conversion efficiency.

The spectrum of scintillation is a consequence of the various light emission mechanisms available within the scintillator and their relative efficiencies. Ce-based and Ce-activated scintillators rely on the 5d – 4f transition mechanism for light production. Due to spin-orbit coupling, the 4f energy state is split into the $^2F_{5/2}$ and $^2F_{7/2}$ energy states, resulting in a double peaked emission spectrum with the peaks being approximately 18nm apart in $CeBr_3$ [68]. Unlike $LaBr_3:Ce$, $CeBr_3$ has not been observed to emit light with any measurable intensity due to an excitonic mechanism.

As shown in Figure 3.4, undoped CeBr₃ exhibits two emission peaks in its radioluminescence spectrum, which blur together to yield a maximum emission peak at 390nm [69]. This emission spectrum for CeBr₃ is well matched to a common bialkali photocathode with an integral quantum efficiency (IQE) near 39.8% for a Photonis XP5301 PMT. NaI:Tl, by comparison, has a slightly lower IQE of 38.8% for the same PMT.

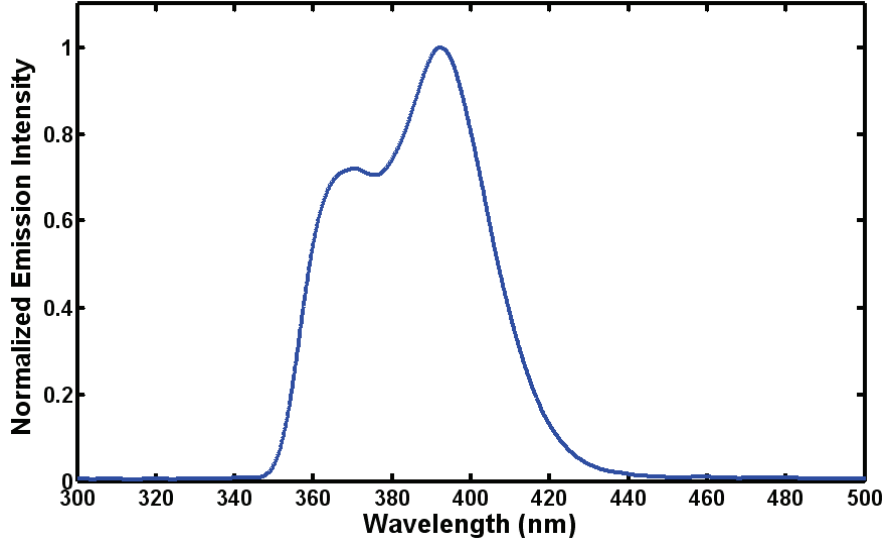


Figure 3.4. Radioluminescence spectrum measured for undoped CeBr₃.

Integral quantum efficiency is the average number of photoelectrons produced in a light conversion device per incident scintillation photon. Each light conversion device exhibits a specific spectral sensitivity ($S_{k,\lambda}$), typically expressed by manufacturers in units of mA W⁻¹, which is a measure of the current produced per unit of power incident. The spectral sensitivity curve for a Photonis XP5301 PMT is shown in Figure 3.5 as an example. From spectral sensitivity, spectral quantum efficiency is given by

$$\rho_{\lambda} = \frac{h\nu}{q\lambda} S_{k,\lambda} \quad (3.1)$$

in which h is Planck's constant, ν is the speed of light in a vacuum, q is the elementary charge, and λ is wavelength [70]. Integral quantum efficiency is the expected value of spectral quantum efficiency over all wavelengths with respect to the spectral emission intensity function, $\Phi_{e,\lambda}$.

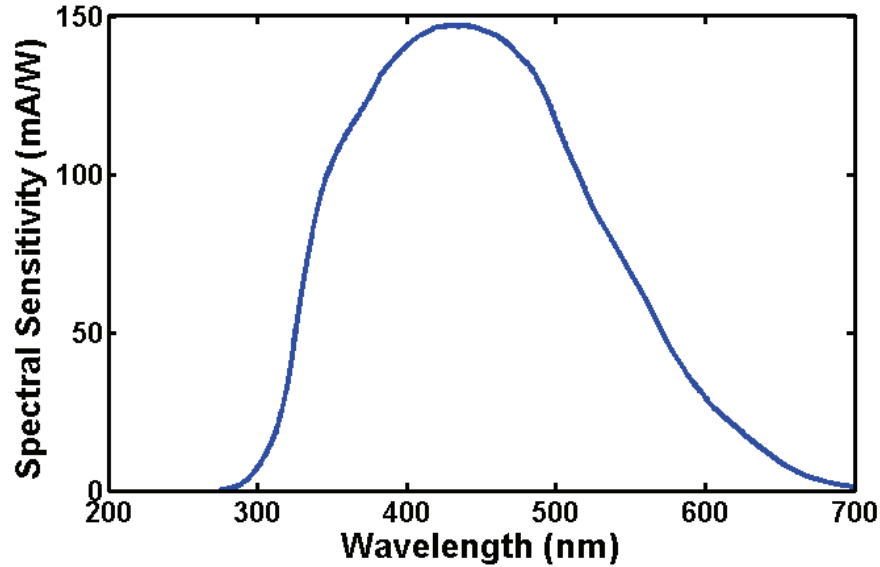


Figure 3.5. Spectral sensitivity curve for a Photonis XP5301B photocathode [71].

The IQE of a scintillator with spectral emission intensity $\Phi_{e,\lambda}$ coupled to a light conversion device with spectral quantum efficiency of ρ_λ is given by

$$I = \frac{\int \lambda \rho_\lambda \Phi_{e,\lambda} d\lambda}{\int \lambda \Phi_{e,\lambda} d\lambda}. \quad (3.2)$$

As stated previously, IQE is the weighted average number of photoelectrons produced per scintillation photon incident upon the surface of the light conversion device given the probabilities of emission wavelength and spectral sensitivity. Of course, the process of photoelectron ejection is a stochastic process and is subject to variance. A well matched scintillator-light detection system possesses high quantum efficiency and thus low relative variance, maintaining high energy resolution in a spectroscopic application.

3.5.2 Light Yield

The total number of photons emitted per unit energy deposited, total light yield, is a critical performance criterion when gauging spectroscopic performance. A higher light yield generally indicates better energy resolution. This trend holds for cases in which proportionality of light yield with respect to energy does not deviate significantly over the range of energies of interest. Proportionality of light yield will be discussed later in detail, but for now we will assume that light yield is roughly constant for all deposited energies.

The average number of photons emitted for a γ -ray of energy E_γ is expressed as

$$\bar{N} = E_\gamma Y \quad (3.3)$$

in which Y is light yield expressed in photons per unit energy. Equivalently, light yield can be expressed as

$$Y = \frac{1}{\kappa E_g}. \quad (3.4)$$

Here, E_g represents the band gap energy of the crystal and κ is a scalar coefficient indicating the average number of band gap energies necessary to yield a photon. κ is approximately 1.5 to 2.0 for ionic crystals. As examples, NaI:Tl is reported to emit approximately 50,000 ph/MeV [48], BGO emits about 6,850 ph/MeV [72], LaBr₃:Ce yields about 70,000 ph/MeV [48] and undoped CeBr₃ emits about 68,000 ph/MeV [45].

The variance about the number of photons emitted following a radiation interaction, σ_N^2 , is well approximated by Gaussian statistics, i.e

$$\sigma_N^2 = \bar{N}. \quad (3.5)$$

The common method of measuring energy resolution in γ -ray spectroscopy is the full width at half maximum (FWHM or Γ) value of a full energy peak. FWHM is related to standard deviation in Gaussian statistics by

$$\Gamma = (2\sqrt{2\ln 2})\sigma_N. \quad (3.6)$$

In terms of percent, Eqn. (3.6) becomes

$$\Gamma(\%) = \frac{2\sqrt{2\ln 2}}{\sqrt{N}}, \quad (3.7)$$

which illustrates the fact that as light yield increases, percent energy resolution improves.

The light yield of a scintillator depends on several factors. Many mechanisms during the scintillation process may cause energy to be lost. Phonon production during thermalization is a significant energy loss mechanism, in which it is estimated that about 30% of the initially absorbed energy is lost from the scintillation process and never recovered. Of course, F centers and direct recombination also play a strong role. The concentration of luminescence centers also plays a part in determining the efficiency at which energy is transferred to them. Too few luminescence centers results in long migration lengths for the charge carriers and subsequently greater energy losses.

3.5.3 Self-Absorption

A tendency to re-absorb emitted scintillation photons is highly undesirable in scintillators as it places a spatial dependency on the signal. Radiation absorption events occurring farther from the light detector coupling surface will have a lower signal than those occurring near the coupling surface, causing degradation in energy resolution.

Cuboid samples are parallelepipeds with all angles being 90°. Designating the side lengths to be x , y , and z in descending order, the largest faces are the two xy -surfaces as illustrated in Figure 3.6. In the work that follows, all samples were cuboid in shape and were mounted to PMT faces on one of their two xy -surfaces. As such, the discussions that follow only consider cuboid-shaped samples mounted in the manner shown in Figure 3.6. The z -dimension is often referred to as height, whereas the x and y -dimensions are referred to as the side dimensions.

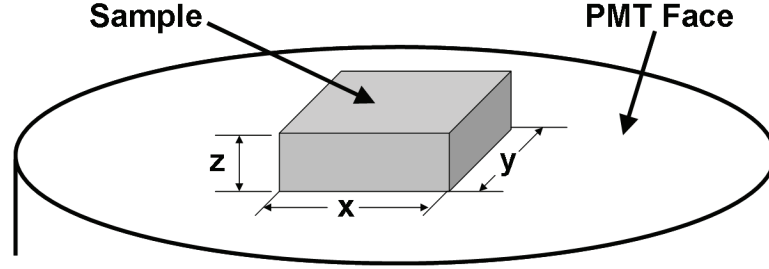


Figure 3.6. Illustration of sample orientation and referenced dimensions.

It is claimed that measured light yield data indicates that CeBr_3 absorbs its own light significantly more than $\text{LaBr}_3:\text{Ce}$ [69]. This claim, however, is based on a rather simplistic 1D model of light propagation dubbed the ‘2R’ model. The 2R model, introduced by Wojtowicz et. al. [73], describes the dependence of measured total light yield on sample height as

$$Y = Y_0 \frac{1 - \exp(-2\Lambda H)}{2\Lambda H}, \quad (3.8)$$

in which Y is the measured light yield of a sample of height H . Y_0 is the measured light yield in the limit of $H \rightarrow 0$ and Λ is a self-absorption attenuation parameter of the material.

A second model called the ‘2R+’ model accounts for some of the simplifications of the 2R model and was introduced by Drozdowski et. al.[74] not long after the introduction of the 2R model. The 2R+ model describes the dependence between measured light yield and sample height as

$$Y = Y_0 \frac{\mu_\gamma}{2(\exp(\mu_\gamma H) - 1)} \left[\frac{\exp((\mu_\gamma - \Lambda)H) - 1}{\mu_\gamma - \Lambda} + (1 - \beta) \frac{\exp((\mu_\gamma - \Lambda)H) - 1}{\mu_\gamma + \Lambda} \exp(-2\Lambda H) \right], \quad (3.9)$$

where μ_γ is the γ -ray attenuation coefficient of the material and β is the average reflectivity of the reflector material mated to the surfaces of the sample. H , Y_0 and Λ are as defined for the 2R model. While more sophisticated, the 2R+ model still predicts measured light yield as being dependent solely on sample height.

Analysis of the predicted light collection efficiency characteristics of cuboid-shaped scintillator samples with a Monte Carlo light propagation code shows a strong dependence of light collection efficiency on cuboid sample side dimensions, not just crystal length as hypothesized in the ‘2R’ and ‘2R+’ models. Figure 3.7 shows this dependency quite clearly. All samples simulated in the DETECT2000 program [75] were 10 mm long, but had square faces of differing lengths. Each set of data in Figure 3.7 was simulated with different self-absorption parameters. Mean free bulk absorption paths (MFP) ranged from 20mm to infinity, i.e. zero self-absorption. All sets were simulated with identical surface reflectivity conditions, rough ground with a reflection coefficient of 0.9. While the calculated light collection efficiencies in Figure 3.7 clearly show a dependence on side dimensions, both the 2R and 2R+ models contend that dependency on side dimensions are negligible.

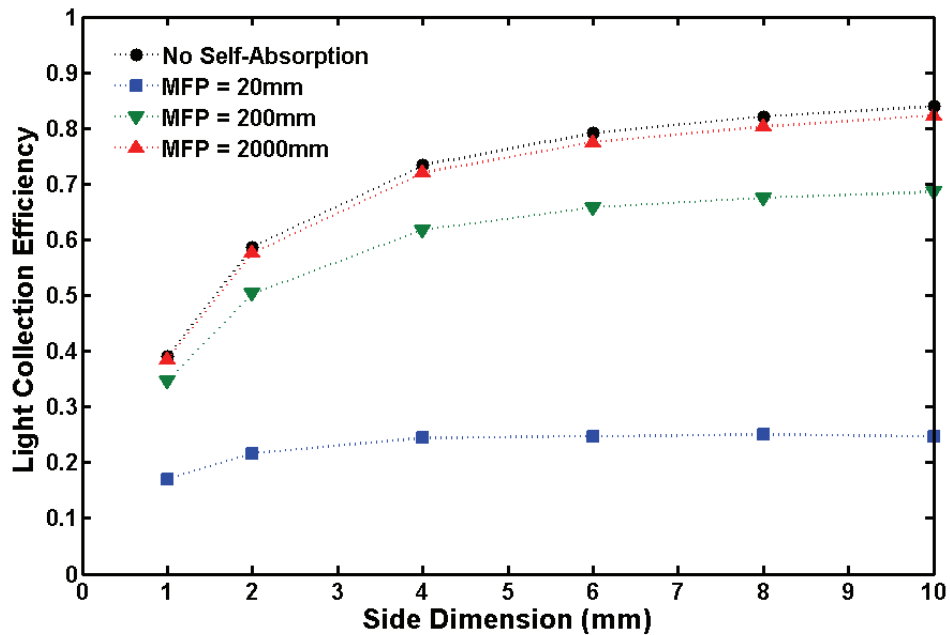


Figure 3.7. Light collection efficiencies calculated for cuboid CeBr_3 samples of length 10mm with the specified side dimension. All simulations were performed with identical surface conditions; the surface coupled to the light detector was optically smooth and coupled using optical grease while the other five surfaces were all simulated as ‘GROUND’ with a reflectivity constant of 0.9. All simulated bulk absorption mean free paths show an increase in LCE as side length is increased, contrary to that predicted by the 2R model.

It is interesting to note that simulated samples with higher MFPs (less bulk absorption) show a much stronger dependency on side dimensions than those with large bulk absorption

losses. This is enforced by the fact that lower bulk absorption losses allows emitted photons to travel farther in the crystal and increases the importance of surface conditions and the absorption occurring there.

The data presented by Drozdowski et. al. [69] as evidence that CeBr_3 is strongly self-absorbing is shown in Figure 3.8 below. The data is presented as the number of photoelectrons produced at the photocathode per MeV of energy absorbed in the scintillator. Presenting data in this format neglects the emission spectrum of the scintillator and the spectral sensitivity of the PMT. Nonetheless, the emission spectra of the samples and the spectral sensitivity of the PMT can be assumed constant in this case, thus providing a relative estimate of measured light yield.

Unfortunately, sample side dimensions were not reported. It is made clear though that the samples did not have similar side dimensions. Thus, little or no information can be gleaned from the data in Figure 3.8 leaving the question of whether CeBr_3 is strongly self-absorbing still wholly unanswered, since alternate explanations of the photoelectron yield dependency on sample thickness can be made based entirely on changes in sample side dimensions and surface preparations.

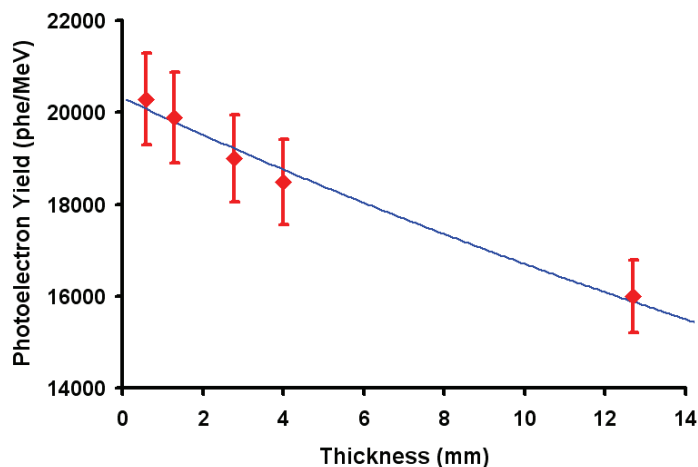


Figure 3.8. Plot of photoelectron yields published by Drozdowski et. al. [69] for samples of CeBr_3 of various heights.

Despite the obvious flaws in the 2R and 2R+ models, they still maintain some merit as a comparison device between samples of identical side dimensions. Figure 3.9 illustrates this fact, comparing the LCE of various samples of face size 1mm x 1mm and differing lengths. If sample side dimensions of two identically sized samples were held constant as thickness was varied,

then some measure of the self-absorption characteristics could be accomplished, at least yielding a semi-quantitative measure of the difference between the two samples.

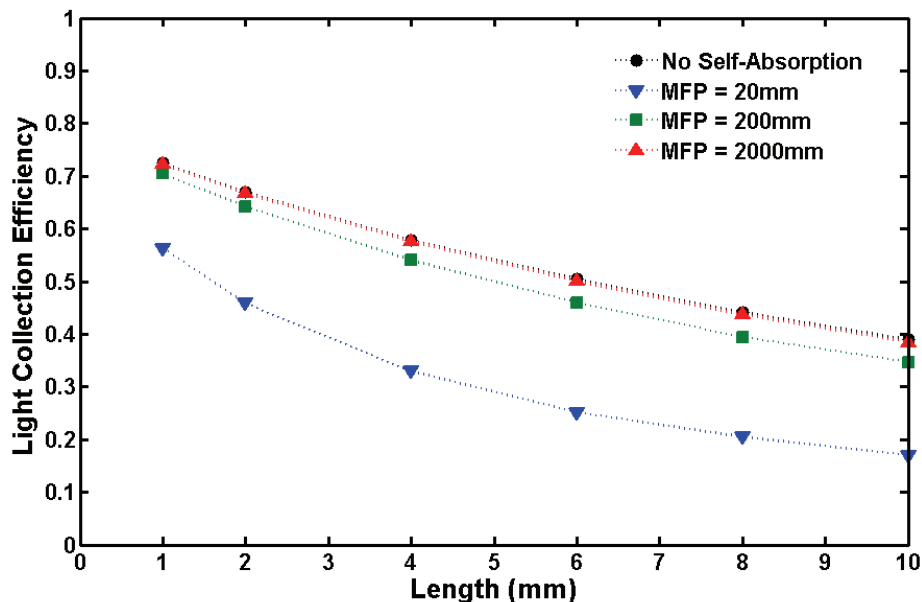


Figure 3.9. Light collection efficiencies calculated for cuboid CeBr_3 samples of face areas of 1mm x 1mm with the specified length. All simulations were performed with identical surface conditions; the surface coupled to the light detector was optically smooth and coupled using optical grease while the other five surfaces were all simulated as 'GROUND' with a reflectivity constant of 0.9. All simulated bulk absorption mean free paths show a decrease in LCE as length is increased.

The lack of a comprehensive model accurately describing the dependencies of measured light yield on geometry, reflector, and self-absorption characteristics presents difficulties in extracting the self-absorption characteristics from the uncertainties in geometry and reflector properties. Other means of determining self-absorption properties are thus necessary. Comparison of radioluminescence spectra and total light yields though can provide a quick indication of changes to self-absorption characteristics of a scintillator. In this work, the primary concern is whether a dopant alters the scintillation performance of undoped CeBr_3 . Any changes to the self-absorption characteristics of CeBr_3 will be apparent in comparing the radioluminescence spectrum of undoped CeBr_3 to that of doped CeBr_3 .

Absorption of scintillation photons is caused by energy states in the energy band gap of the crystal which can absorb light with energy equal to or greater than the absorbing energy state.

Thus, any absorbing energy states introduced into CeBr_3 by a dopant can cause one of two effects. If the absorbing energy state lies just below the Ce^{3+} 5d-4f transition energy, then the radioluminescence emission peak will likely shift towards the red end of the emission spectrum as illustrated in Figure 3.10.

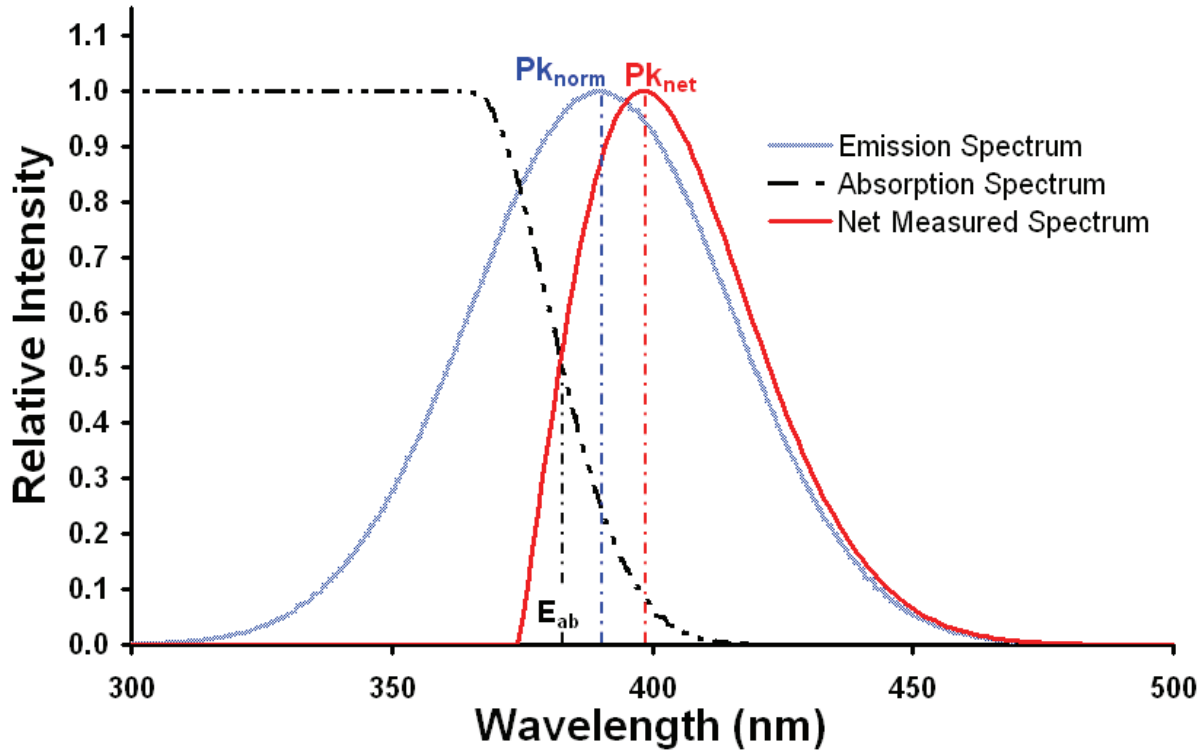


Figure 3.10. Example of how an added absorption energy state, E_{abs} , can cause the peak radioluminescence emission of an undoped scintillator, Pk_{norm} , to shift to a higher wavelength, Pk_{net} when introduced. As E_{abs} is shifted to lower energies, Pk_{net} shifts to even lower energies. Emission and absorption spectra shown here are normalized to their peak intensities.

If the absorbing energy state resides far below the Ce^{3+} 5d-4f transition energy, i.e. $E_{abs} \ll E(Pk_{norm})$, then the entire emission peak will be attenuated. In a normalized form, the radioluminescence spectra of doped and undoped samples may appear similar in this case. However, an absorbing energy state well below the emission peak will cause a decrease in total light yield and thus be detected in measuring the total light yield of identically sized and shaped, doped and undoped samples.

3.5.4 Proportionality of Light Yield

It is a well known fact that the light yield of scintillators is not constant for all deposited energies. NaI:Tl, in fact, varies substantially, on the order of 20% or more, over the range from a few keV to 1MeV. CeBr₃, though, is quite constant, varying just a few percent over the same range. While one might initially suspect that this effect only acts to cause the scaling between pulse height and energy deposited to be non-linear, the effect of non-proportionality has deeper consequences.

If all γ -rays were absorbed via the photoelectric absorption mechanism, then the only consequence of light yield (LY) non-proportionality would indeed be an inconvenient non-linear scaling between pulse height and energy deposition. Unfortunately, γ -rays can also Compton scatter one or more times before being finally photoelectrically absorbed. Summing the light luminosity created by multiple Compton scatters followed by a photoelectric absorption does not necessarily match the luminosity created by a single photoelectric absorption event. While the same total amount of energy may be deposited for the two different scenarios described above, the total amount of light emitted can differ due to the fact that the photon interactions occurred under differing light yield efficiencies. As a consequence, LY non-proportionality is recognized as being a significant factor in causing degradation in energy resolution. Of course, this effect is seen more prominently in larger crystals as the likelihood of fully absorbing energy from one or more Compton scatter events is increased.

The phenomena behind LY non-proportionality are still yet to be fully understood, but a few dependencies have been observed. Historically, it was thought that the non-linearities in the stopping power of energetic electrons as they slow down played a strong role in LY non-proportionality. While this still holds truth, it appears that other factors also play major roles in determining scintillator LY non-proportionality. Studies of undoped NaI at cryogenic temperatures (77K and below) resulted in non-proportionality curves very similar to those obtained with NaI:Tl at room temperature, indicating that non-proportionality is a function of the host crystal, not the dopants [7]. Contrarily, a recent study showed that impurity concentrations affect the non-proportionality of NaI [76], indicating that the host crystal is less at fault than originally thought. While host crystal and impurities both seem to play roles in non-proportionality, it ultimately seems the problem of non-proportionality is still in dire need of further investigation as no model fully unites the observed phenomena under a single theory.

3.5.5 Decay Times

The decay of scintillation light after the absorption of a quantum of ionizing radiation typically follows exponential distributions as would be expected assuming first-order kinetics in which the concentration of available luminescence centers is greater than the concentration of excited electrons and holes [7]. The decay of the scintillation light is then primarily dependent on the kinetics of the radiative centers and their relaxation.

Secondary decay modes may be added to a scintillator when new impurities are introduced into the lattice. The altered energy levels generated at the lattice site of an impurity/dopant may fall within the energy band gap of the matrix, producing a photon absorption site. Alternatively, an impurity may degrade light emission by trapping excited charge carriers or excitons. If a second radiative center were to become non-negligible in the participation of light emission, then two decay modes would be observed, such as may occur when doping a single decay mode compound like CeBr₃.

CeBr₃ exhibits a single mode of exponential rise and decay with time constants of approximately 0.1ns and 17ns respectively [45]. The light intensity $J(t)$ of scintillators with such kinetics follow [7]

$$J(t) = \frac{N_{ph}}{\tau_d - \tau_r} \left[\exp\left(-\frac{t}{\tau_d}\right) - \exp\left(-\frac{t}{\tau_r}\right) \right], \quad (3.10)$$

where N_{ph} is the number of photons emitted, τ_d is the decay time constant and τ_r is the rise time constant. CeBr₃ possesses short rise times, fast decays and high intensities. All are favorable properties for timing applications and/or applications requiring high count rates. For a scintillator with two decay modes with decay constants τ_1 and τ_2 , the kinetic equation can be written as

$$J(t) = J_1 \left[\exp\left(-\frac{t}{\tau_1}\right) - \exp\left(-\frac{t}{\tau_r}\right) \right] + J_2 \exp\left(-\frac{t}{\tau_2}\right) \quad (3.11)$$

in which J_1 and J_2 are the intensity contributions of the two modes respectively. Figure 3.11 plots Eqn. (3.10) and Eqn. (3.11) for undoped CeBr_3 and a fictitious, doped CeBr_3 sample in which a second, long-lived decay mode is present.

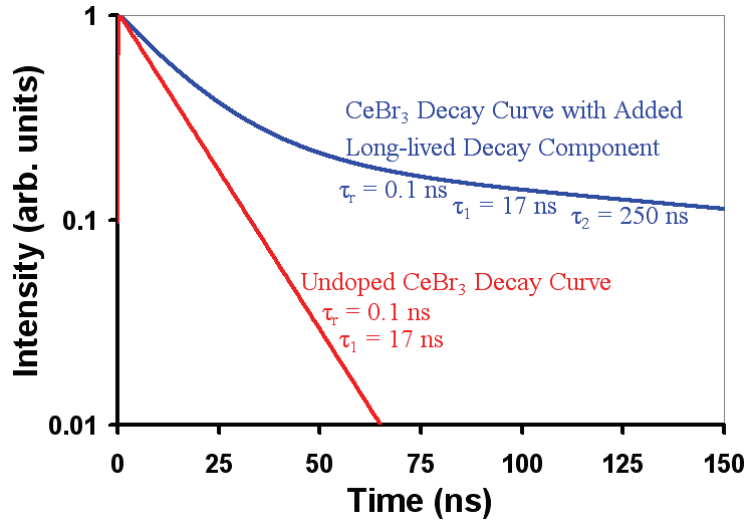


Figure 3.11. Light intensity plotted over time for single decay mode, undoped CeBr_3 and a fictitious, albeit potential, light decay curve for CeBr_3 with a second long-lived decay mode.

3.6 Summary

The signal generation process in scintillation spectrometers is initially quite similar to semiconductor spectrometers. Electrons and holes are excited across an energy band gap through some interaction with radiation. However, rather than simply drifting the charge carriers through the bulk before they can de-excite to their ground states such as is done in semiconductor spectrometers, charge carriers are forced to de-excite back to their ground state quickly. The kinetics of each material type are carefully controlled through doping to achieve different results. Material producers go to great lengths to eliminate impurities from semiconductors to reduce the density of deleterious charge traps and increase excitation life times. On the other hand, dopants are selectively added to scintillators to force charge carriers to de-excite quickly and, preferably, via radiative relaxation methods. Altering the chemistry of either material can have dire consequences to its performance.

In the following work, aliovalent dopants were added to CeBr_3 to improve the mechanical properties of the matrix. Unfortunately, the addition of these dopants could potentially alter the

scintillation performance of CeBr₃. Predicting dopant effects a priori is an arduous task best tackled by supercomputers, which still only provide rough approximations.

Trial and error experimentation can provide more accurate knowledge of the effects of dopants upon scintillation performance. However, trial and error experimentation requires many trials and much time. To reduce the number of trials, careful selection of dopants through past experimental knowledge provides a measure of protection against known scintillation “killers”, such as Pb and other elements possessing multiple stable valences [44]. The following work approaches the question of how aliovalent doping affects the scintillation performance of CeBr₃ through the trial and error method. Judicious selection of dopants from the available aliovalent candidates expected to provide potent strengthening effects without deleteriously affecting scintillation performance was used to reduce the number of trials to a reasonable size.

4 Experimental Methods

Based on the theory behind aliovalent strengthening, several dopants were chosen as candidates for study based on four general criteria. First, it was determined that only ions with valency ± 1 different than the ions in CeBr_3 would be considered. Second, cationic doping was chosen rather than anionic doping since the number of candidate aliovalent cations available was much greater. Third, of the available aliovalent cation dopants, only those possessing ionic radii near Ce^{3+} were considered. This third selection criterion was based on the fact that aliovalent ions possessing an ionic radius near that of Ce^{3+} minimized the chance that secondary phases would precipitate out rather than incorporate into the CeBr_3 lattice. Finally, the fourth criterion stipulated that the aliovalent cation not exhibit multiple stable valences, such as is the case for Pb in which stable Pb^{2+} and Pb^{4+} valences are observed [44]. Eliminating potential candidates based on these criteria left the potential dopant set with only seven cations, Ca^{2+} , Sr^{2+} , Ba^{2+} , Zn^{2+} , Cd^{2+} , Zr^{4+} and Hf^{4+} . Pb^{2+} was later added as a check against the fourth criterion.

Several complex steps were necessary to properly prepare and characterize samples doped with the above candidate dopants to experimentally determine their effects on CeBr_3 . First, accurately doped single crystal samples were prepared, which required proper handling techniques devoid of contamination, single crystals grown from the melt, and single crystalline samples harvested from the as-grown ingots. The difficulties in handling the raw materials, as-grown ingots and prepared samples were chiefly due to the fact that CeBr_3 is highly hygroscopic.

After a single crystalline sample was prepared, several measurements were made to determine the effect the dopants had on the scintillation properties of the material. The measurements conducted included radioluminescence spectra, estimation of the total light yield as compared to BGO, light yield non-proportionality, and γ -ray spectroscopy.

Each of the steps taken to determine the effects of aliovalently-doping CeBr_3 are described in detail in the following sections. Since it was necessary to design and construct all equipment required for the project, the design and construction steps are detailed as well.

4.1 Crystal Growth

The horizontal gradient freeze (HGF) method of crystal growth was chosen for growing single crystalline samples of CeBr_3 for several reasons that will be discussed later. Prior to crystal growth, ampoules with the proper amount of dopant and CeBr_3 were prepared. Next, crystals were grown via the HGF method in two electro-dynamic gradient (EDG) furnaces. As-grown ingots were extracted from the ampoule and single crystalline samples were cut from the ingots using a diamond wire saw. Cut samples were lapped flat and finally dry polished using 4000 grit SiC grinding paper in preparation for the characterization steps. Due to the large number of dopants and dopant concentrations to be investigated, focus was kept on quickly producing sufficient samples, rather than ingot yields.

4.1.1 Ampoule Preparation

A simple quartz ampoule design was chosen for the growth step to reduce costs. The ampoule was designed to have a simple hemispherical nose and plugged by a similarly shaped, but slightly smaller diameter quartz plug. Full dimensions are shown in the cross-sectional drawing of Figure 4.1. Prior to loading, each ampoule was “notched” at approximately 110 mm above the shoulder of the bottom hemisphere. This “notch” was simply an indentation in the ampoule side wall caused by softening the wall at a single spot with a $\text{H}_2\text{-O}_2$ torch while the ampoule was under vacuum. Notches were added to the ampoule to hold the plug above the powder surface during sealing. Since the feedstock CeBr_3 10 mesh beads have a packing fraction of roughly 50% ($\rho = 5.18\text{g} \cdot \text{cm}^{-3}$), a notch placed at 110 mm allowed the as-grown ingot to occupy the bottom 40-45% volume of the ampoule when laid horizontally. This step ensured that the ingot would be able to expand upward if needed during cooling without being inhibited by the quartz ampoule wall.

After notching, each ampoule was cooled and rinsed with isopropanol, then loaded into an anti-chamber of a Vacuum Atmospheres Co. Omni-Lab ultra-dry atmosphere (UDA) glove box. The anti-chamber was evacuated and purged three times with ultra-dry N_2 gas as was standard laboratory practice for transferring any object into the UDA glove box. The ampoules were allowed to dry overnight after entering the UDA glove box.

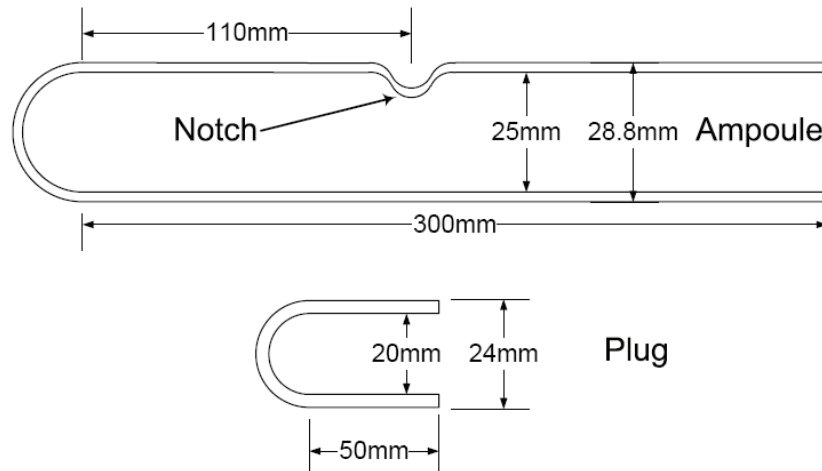


Figure 4.1. Cross-sectional sketch of the quartz crystal growth ampoule and plug.

Each ampoule was loaded with 140g of 99.999% pure, anhydrous beads of CeBr_3 (Aldrich APL) and the corresponding amount of dopant (Sigma Aldrich). CeBr_3 10 mesh beads were poured into tared, clean plastic Petri dishes atop an Ohaus Voyager Pro self-calibrating, electronic balance until $\sim 140\text{g}$ was reached. Accuracy of the CeBr_3 mass was far less crucial than that of the dopant. Using a plastic sheet rolled into a funnel, approximately half the beads were then transferred into the ampoule. A second plastic Petri dish was next tared and loaded with dopant to achieve a mass as near as possible the target mass. Dopants investigated included CaBr_2 (99.98% pure), SrBr_2 (99.995% pure), BaBr_2 (99.999% pure), ZrBr_4 (98% pure), HfBr_4 (99.99% pure), ZnBr_2 (99.999% pure), CdBr_2 (99.999% pure), and PbBr_2 (99.999% pure). Each dopant was then investigated at two concentration levels, 500ppm and 1000ppm atomic relative to Ce. The equivalent target masses for each dopant and concentration are provided in Table 1. The dopant beads or powder was then transferred to the ampoule using the funnel again. Finally, the remaining CeBr_3 beads were transferred to the ampoule.

Three key steps during ampoule loading were necessary to ensure proper loading. First, the Petri dishes were weighed with the beads or powder before and after transferring to the ampoule, since powder visibly adhered to the plastic Petri dish surfaces. The difference between the two readings was recorded as the mass having been loaded into the ampoule.

Second, it was noted that during the initial evacuation of the ampoule, a small amount of powder was sometimes swept into the vacuum system. To avoid loss of dopant in the event of such an accident, the dopants were loaded into the middle of the powder. A small loss of CeBr_3

powder mattered very little in determining dopant concentration, while a small loss of dopant could dramatically skew results. Placing the dopant far below the surface reduced that risk.

Thirdly, powder was noted to also adhere to the inside surface of the ampoule during the transfer process. A funnel was fabricated using a clear plastic sheet which extended below the sealing region to ensure no powder contaminated the seal between the plug and the inner ampoule wall.

Table 4.1. Target doping masses for each dopant at the two specified doping levels assuming 140g CeBr₃ charges.

Dopant	Mass (mg)	
	500ppm	1000ppm
CaBr ₂	39.5	78.9
SrBr ₂	48.9	97.7
BaBr ₂	58.7	117.3
ZrBr ₄	81.1	162.2
HfBr ₄	98.4	196.7
ZnBr ₂	44.5	88.9
CdBr ₂	53.8	107.5
PbBr ₂	72.5	144.9

Loaded ampoules were next labeled and sealed onto a QF Flange-to-Quick Connect Adapter Fitting and QF-flanged butterfly valve assembly. Later, the butterfly valve was replaced with a bellows valve to improve pressure control during opening. This adapter-valve assembly ensured normal atmosphere was not introduced into the ampoule during the transfer from the UDA glove box to the vacuum system. The valve-sealed ampoule assembly was then transferred out of the UDA glove box and attached to a vacuum system using QF couplers.

The vacuum system consisted of an Alcatel ATP80 turbomolecular pump backed by a BOC Edwards 5 rotary vane mechanical roughing pump. Pressure measurement across the range of 760 Torr to 1×10^{-7} Torr was accomplished using two different pressure gauges. A Teledyne Hastings DV-6M thermocouple-type pressure transducer was used to measure pressures between 2 Torr down to $\sim 1 \times 10^{-2}$ Torr. An MKS Model 423 cold-cathode ion pressure transducer covered pressures between 1×10^{-2} Torr and 1×10^{-7} Torr. The vacuum system was also plumbed to allow ultra-high purity (UHP) grade N₂ gas to be used as a purge gas. Finally, a Thermolyne 21100 single zone tube furnace was mounted so that the ampoule could be heated during the evacuation process. Ultimately, the sealing system was capable of easily reaching vacuum levels on the

order of 1×10^{-6} Torr or below, while the tube furnace was capable of maintaining ampoule temperatures in excess of 1100°C if ever necessary.

Flame-sealing ampoules required several steps. First, ampoules were securely attached to the vacuum system using a QF40 flange. The roughing pump was turned on and allowed to reach $<1 \times 10^{-1}$ Torr. The valve sealing the ampoule was then slowly opened to evacuate the ampoule to $<1 \times 10^{-1}$ Torr. Opening the valve was a critical step, since opening the valve too quickly caused the powder to be swept up into the vacuum system. Initially, a butterfly valve was used, but a bellows valve was later employed to allow the evacuation of the ampoule to be better controlled. Once the entire vacuum system had reached a pressure $<1 \times 10^{-1}$ Torr, the turbomolecular pump was started. The vacuum system was then monitored to ensure a sufficiently low pressure was reached ($<5 \times 10^{-6}$ Torr).

The furnace was next brought into position around the portion of the ampoule below the top edge of the plug, insulated between the ampoule and the furnace wall, and set to maintain 100°C . During this heating cycle, pressures were noted to increase into the 10^{-5} Torr range for a short period before dropping back to pressures $<5 \times 10^{-6}$ Torr. Presumably, this was due to evaporating adsorbed water. Finally, pressure (5×10^{-6} Torr) and temperature (100°C) were held overnight to ensure the loaded material was fully baked out.

After many hours (≥ 12) of baking out, the furnace was dropped away from the ampoule. The ampoule was then flame-sealed onto the quartz plug using an $\text{H}_2\text{-O}_2$ torch. During sealing, pressure was noted to increase up to 1×10^{-5} Torr, despite typically reaching the 10^{-7} Torr range after being baked out overnight.

4.1.2 Growth Process

Crystal growth of lanthanide halides is typically accomplished utilizing the vertical Bridgman melt growth technique. However, ingot cracking is a significant problem in growing lanthanide halides as they possess highly anisotropic thermal expansion characteristics. Consequently, large thermal stresses are developed within the ingot during the application of a thermal gradient not parallel to the c-axis, such as that found in melt growth. Since the vertical Bridgman method constrains the ingot so much, providing only a small free surface area for the ingot to expand and contract, stress levels are likely higher than in a horizontal arrangement where free surface area is significantly higher. Horizontal melt growth techniques therefore

appeared to be advantageous for growing large single crystals of lanthanide halides as the stress induced on the ingot during cooling is likely reduced.

Crystals were grown inside two nearly identical EDG furnaces. Two prepared ampoules were loaded nose-to-nose inside each furnace as shown in Figure 4.2. The entire furnace was heated above the melting point of CeBr_3 ($T_m = 733^\circ\text{C}$) and held for some time to ensure all material had fully melted. Outer zones were then cooled in succession to a temperature below the melting point. Monitoring of an internally mounted thermocouple was used the first time to determine that a temperature of 740°C was sufficient to fully melt the material, denoted as T_{hot} . After several trial and error attempts with the first ingot, it was found that 700°C was sufficient to act as the temperature below the melting point to which the ingot could be cooled, designated as T_{cold} . Temperature settings of $T_{hot} = 740^\circ\text{C}$ and $T_{cold} = 700^\circ\text{C}$ were used throughout the growth of all ingots. However, cooling rates and schemes were altered as an attempt to improve single crystal yields.

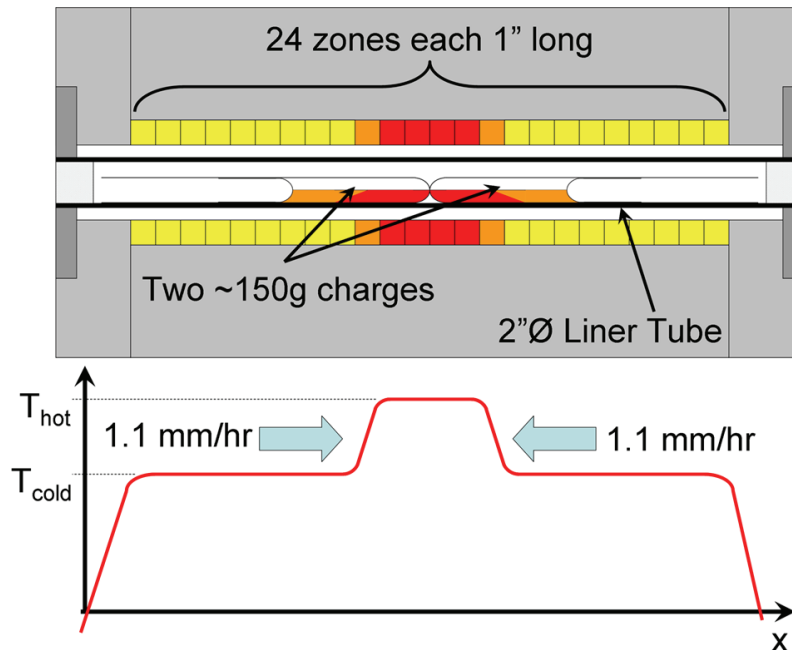


Figure 4.2. Prepared ampoules were laid nose-to-nose within each EDG furnace to speed crystal growth efforts. Ingots were cooled from the outside towards the center zones which propagated the freeze interface. Zones were programmed to cool from T_{hot} to T_{cold} such that growth progressed at an average rate of 1.06 mm/hr.

Initially, cooling was programmed to occur in each 1” long zone, in turn, from T_{hot} to T_{cold} over the course of 24 hrs. This recipe was designated the ‘single step’ method. Later, a study was done in which ‘two step’ and ‘four step’ recipes were developed to reduce the applied thermal gradient fluctuations and, hopefully, crystal cracking. The ‘two step’ recipe cooled two zones simultaneously, an inner zone from T_{hot} to $T_{1/2}$ and the outer zone from $T_{1/2}$ to T_{cold} over the course of 24 hrs, where $T_{1/2}$ was the temperature halfway between T_{hot} and T_{cold} . The ‘four step’ recipe thus cooled four zones simultaneously. From inside outward, the first zone was cooled from T_{hot} to $T_{3/4}$, the next zone from $T_{3/4}$ to $T_{1/2}$, the third zone from $T_{1/2}$ to $T_{1/4}$, and the final zone from $T_{1/4}$ to T_{cold} . For the T_{hot} and T_{cold} settings mentioned above, $T_{1/4} = 710^{\circ}C$, $T_{1/2} = 720^{\circ}C$, and $T_{3/4} = 730^{\circ}C$. While all three cooling schemes propagated the freeze interface at an average rate of 1.06 mm/hr, the ‘two step’ and ‘four step’ methods provided lower and more uniform thermal gradients. This fact is illustrated in comparing the cooling process as shown in Figure 4.3 to that shown in Figure 4.4. In both cases, the freeze interface moves one inch over 24 hrs. However, the applied thermal gradient at the freeze interface does not change in the ‘four step’ recipe. The ‘single step’ recipe applies differing thermal gradients at the freeze interface, likely causing a non-constant growth interface velocity with varying growth stability conditions.

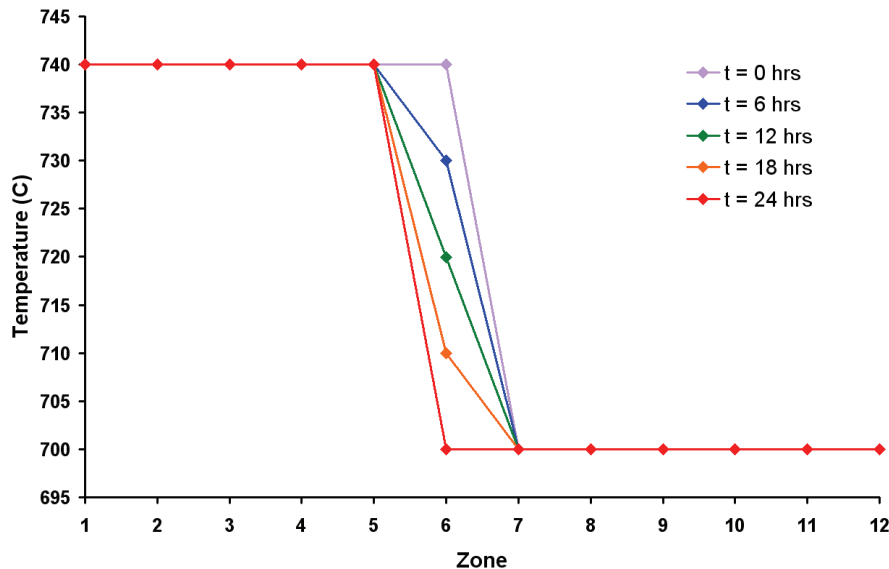


Figure 4.3. Periodic plot of zone set points during the course of propagating the freeze interface one inch in the ‘single step’ recipe. As crudely approximated here, the thermal gradient at the crystal growth interface (slightly below 733°C) changes throughout the growth step of 1”.

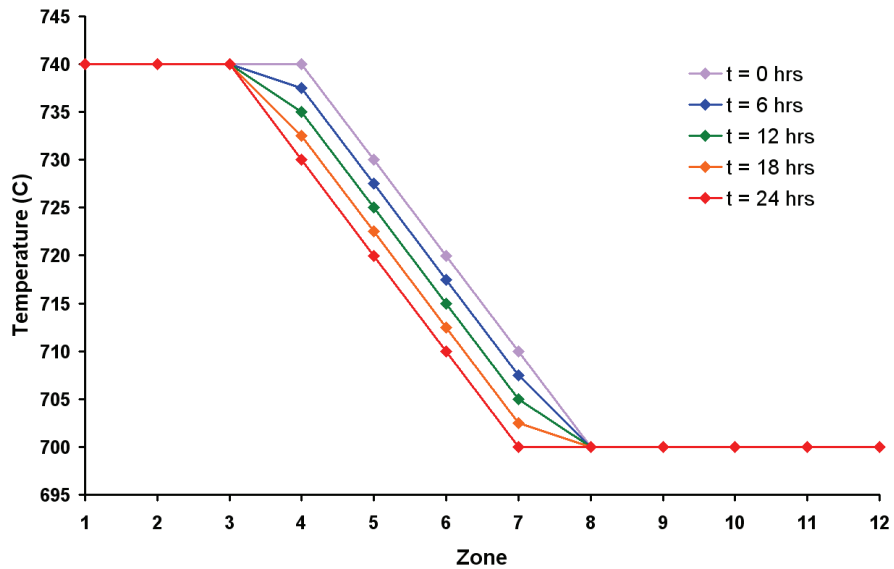


Figure 4.4. Periodic plot of zone set points during the course of propagating the freeze interface one inch in the ‘four step’ recipe. As opposed to the ‘single step’ growth recipe, the thermal gradient at the crystal growth interface (slightly below 733°C) remains constant throughout the growth step of 1”.

It was found that the ‘four step’ recipe produced perhaps slightly larger single crystals than did the ‘two step’ recipe, which was slightly improved over the ‘single step’ recipe. Results were not significantly different though, thus no clear conclusion could be drawn from the study. Presently, it is felt that, while the ‘four step’ recipe provided improved thermal gradient uniformity, applied thermal gradients were too low to maintain stable growth conditions. Ideally, the applied thermal gradient would be much greater than 10°C/inch and remain constant throughout the growth process. Horizontal Bridgman crystal growth does offer both of these features, but lack of equipment halted further investigation in that direction.

Once all zones had cooled to T_{cold} following growth, the EDG furnaces were programmed to cool all zones uniformly to RT at a cooling rate of 5°C/hr. Cooling was performed at such a low rate to avoid generating thermal gradients and, consequently, thermal stress. Past experience with a vertical Bridgman crystal growth system showed that a cooling rate of 5°C/hr was acceptable for maintaining single crystals of LaBr₃ of similar diameter in a vertical arrangement. Given the lower stress of a horizontal arrangement, the 5°C/hr cooling rate was deemed acceptable. Indeed, very little thermal cracking was noted to occur in CeBr₃ ingots grown using the ‘four step’ recipe with a cooling rate of 5°C/hr.

4.1.3 Sample Harvesting

As-grown ingots were typically about 12cm long and had a D-shaped cross-section. Extracting usable samples from each ingot required a large amount of ingot mounting and cutting.

Ampoules were pulled from the EDG furnaces after having fully cooled to room temperature (RT). A SiC disk saw was then used to cut the ampoule wall until vacuum was broken. The ampoules were subsequently wrapped in clean room towels and snapped in half by hand. The clean room towels prevented any shards from scattering around and potentially injuring personnel. The ingots slid easily from the quartz ampoule onto a clean work surface. The ingots were rinsed with isopropanol then quickly placed under mineral oil. Often, as-grown ingots were coated with liquid bromine, likely a by-product of O₂ and/or H₂O contamination. The isopropanol rinse removed most of this bromine liquid. Mineral oil is itself hydrophobic and proved to be an excellent barrier against contamination by O₂ and H₂O. Once immersed in mineral oil, the as-grown ingots were transferred into an UDA glove box for further processing.

As-grown ingots were next mounted to soft ceramic cutting blocks using low melting point wax. Despite being low temperature wax, heating and cooling rates were critical for maintaining ingot integrity. Small pieces of wax were placed atop a ceramic cutting block at least ½” thick. The ingot was placed on top of the wax pieces. The cutting block was next placed on a hot plate at RT. The hot plate was turned on to a setting just high enough to melt the wax after 15min of heating. Once the wax had completely melted, the ceramic block was removed from the hot plate and placed on a stainless steel surface for cooling. The mounted ingot and cutting block were placed inside a plastic container and immersed in mineral oil for transport to the diamond wire saw.

Cutting blocks were mounted to the diamond wire saw using a vise. Ingots were typically cut across the longitudinal axis at intervals ranging from 5 mm to 12 mm, depending on the crystal structure. Intervals were chosen to maximize the single crystal sample yield from each ingot. The saw was retrofit to use mineral oil as the cooling fluid and samples were wetted routinely by hand to maintain a surface coating of mineral oil. This added step minimized surface degradation from O₂ and H₂O throughout the sawing process.

Each slice containing single crystals of sufficient size were dismounted from the ingot cutting block and remounted to smaller sample cutting blocks using the same method of

mounting as described for the ingots. Cuboid samples were ultimately cut from each slice, dismounting and remounting as necessary. Care was taken to ensure the six surfaces were as close as possible to 90° from adjacent faces. Samples varied in size significantly, but were limited such that no side length was greater than 11 mm or less than 2 mm.

As-cut samples were next visually inspected for internal flaws and clarity. Samples of poor quality were discarded from the sample set. Of the remaining high quality samples, the highest quality samples for each dopant were set aside for further processing for characterization. Samples were stored under mineral oil inside the UDA glove box.

4.1.4 Sample Preparation

In preparation for characterization, each of the highest quality samples was wiped dry of mineral oil inside the UDA glove box. Each sample was carefully hand-polished on 4000 grit SiC paper until the surfaces were optically transparent. For samples with a large surface area to height ratio (aspect ratio), the lateral surfaces were often not finely polished due primarily to the fact that their polish was relatively unimportant in the photon transport process and secondarily due to the difficulties associated with polishing those small lateral surfaces. Nevertheless, the aspect ratio of each sample was recorded and corrected when necessary.

4.2 Characterization

Several measurements were performed to determine the overall scintillation performance of the doped and undoped samples of CeBr_3 . The measurement equipment setup, experimental procedure and analytical derivation of the results is presented for each measurement in the following sections.

4.2.1 Radioluminescence Spectra

The radioluminescence spectrum emitted by each of the doped materials was perhaps one of the most informative measurements performed. Changes to the relative spectral emission intensity directly indicated that the dopant are affected the light emission and propagation process. While not necessarily deleterious to scintillation performance, alterations to the spectral emission intensities are likely due to absorption effects caused by the dopants since none of the dopants used are known to radiatively emit with good efficiency.

Radioluminescence spectra were measured using an Ocean Optics USB4000 spectrophotometer. The spectrophotometer was calibrated for absolute irradiance measurements between wavelengths of 200nm and 800nm by the manufacturer using a NIST-calibrated black body light source. The optical fiber input to the spectrophotometer was coupled to a light-tight dark box where samples were mounted. Figure 4.5 below shows a sketch of the dark box setup.

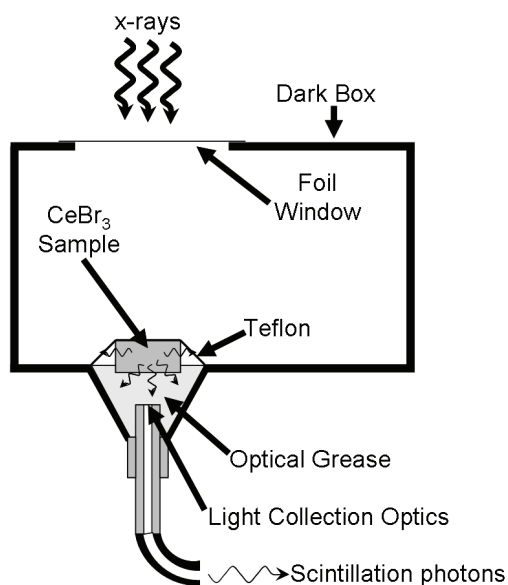


Figure 4.5. Cross-sectional sketch of the light-tight dark box used to collect radioluminescence spectra. The x-ray generator is external to the setup. The scintillation sample is placed in optical grease and covered with Teflon. Scintillation photons collected at the entrance window of the optical fiber are propagated to the Ocean Optics USB4000 spectrophotometer.

A X-CEL Model AP75 x-ray generator was used to excite the CeBr₃ samples at the sample face farthest from the light collection optics. Since absolute spectral emission intensities were not necessary, the x-ray generator was not calibrated nor tightly controlled during measurements. Absolute emission intensities were considered unimportant since total light yield was measured separately as described in Section 4.2.2. Irradiating the sample from the face farthest from the light collection optics ensured that emitted scintillation light must pass through the sample before collection, providing a better measure of any self-absorption energy states.

Measurements were conducted by placing a sample of the scintillator of interest into Bicon BC-630 optical coupling grease which filled the cavity between the sample and the entrance to the optical fiber. Teflon tape was placed on top of the scintillation sample to improve

light collection. All internal surfaces of the dark box were coated in flat black to minimize spectral reflectance issues which might skew spectral emission intensities. Collected light was then propagated to the diffraction grating of the USB4000 spectrophotometer which split the light spectrum into its components. A silicon charge-coupled device (CCD) array collected light between wavelengths of 200nm and 800nm. The number of counts collected at each CCD pixel was recorded over the specified integration time (typically 2s to 30s). Finally, the response spectrum of the CCD array was corrected for the spectral sensitivity of the CCD array as provided by the NIST-calibration from the manufacturer to produce a relative emission intensity spectrum. Since sample sizes varied widely as did the optical coupling between the sample and the optical fiber, the spectra collected could not be directly compared, thus were normalized to have a peak intensity of unity.

4.2.2 Total Light Yield Estimation and γ -ray Spectroscopy

Measuring the absolute number of photons emitted per unit energy is quite complicated. A detailed knowledge of the light propagation properties, spectral sensitivity and absolute response characteristics of a sample-light detector configuration is necessary to accomplish a direct measurement of the amount of light emitted per unit of energy. A slightly simpler method of estimating absolute light yield is accomplished by comparing the output response of a known material to the output response of an unknown, then correcting for their differences in light collection efficiency and radioluminescence spectra.

Total light yield was estimated for samples by comparing their ^{137}Cs spectra against a γ -ray spectrum obtained with identical settings with a BGO crystal. To estimate the total light yield of the sample, two key corrections were taken into account. First, the light collection efficiency (ratio of the number of photons incident on the photocathode to the total number of photons emitted during the scintillation event) was corrected for to compensate for varying sample sizes. Second, the spectral sensitivity of the photocathode must be taken into account to correct for changes in emission spectra between different scintillating materials.

To begin, the total charge collected at the anode of a PMT from light emitted by a scintillator can be estimated as

$$Q = E_{\gamma} Y \epsilon I G_{PMT}, \quad (4.1)$$

where E_γ is energy deposited by a γ -ray, Y is the total light yield of the scintillator in photons per unit energy, ε is the light collection efficiency, I is the integral quantum efficiency of the photocathode to the spectral emission of the scintillator and G_{PMT} is the gain of the photomultiplier. If two samples, an unknown and a known, are tested under identical gain settings, the ratio of their collected charges becomes

$$\frac{Q_x}{Q_s} = \frac{Y_x \varepsilon_x I_x}{Y_s \varepsilon_s I_s}, \quad (4.2)$$

where the subscripts x and s denote the unknown sample and the known standard respectively. Solving for the unknown sample's light yield, it is found

$$Y_x = Y_s \left(\frac{\varepsilon_s}{\varepsilon_x} \right) \left(\frac{I_s}{I_x} \right) \left(\frac{Q_x}{Q_s} \right). \quad (4.3)$$

Light collection efficiencies are difficult quantities to measure, especially when the absolute light yield is also in question. However, Monte Carlo photon transport simulations can provide rough estimates. To estimate the light collection efficiencies of the samples studied here, the program DETECT2000 [75] was used. Individual sample geometries and indices of refraction were used to estimate light collection efficiencies for each cuboid-shaped sample, including the known standard. The index of refraction for the doped CeBr_3 samples was assumed to be 1.95, near the index of refraction for $\text{LaBr}_3:\text{Ce}$ [77].

The geometries simulated were cuboids of scintillator material of size matching the sample dimensions, a $50\mu\text{m}$ thick layer of optical grease, and a 1mm thick layer of quartz to act as a PMT window. The top surface of the scintillator was specified as painted with a diffuse reflector (Teflon) with a reflection coefficient of 0.9. The outer, side surfaces of the scintillator material were specified as rough interfacing with vacuum, while the coupled face was specified as optically smooth. 250,000 photons were generated uniformly throughout the scintillation sample volume with uniformly distributed initial directions. The number of photons incident upon the backside of the quartz window (photocathode) were counted. The ratio of emitted

photons to incident photons was finally calculated and used as an estimate of light collection efficiency, ε , for each sample.

The integral quantum efficiency is a ratio of the number of ejected photoelectrons from a photocathode to the number of incident photons with non-monochromatic distribution, $\Phi_{e,\lambda}$. Recalling Eqns. (3.1) and (3.2), spectral quantum efficiency is estimated from the manufacturer's published spectral sensitivity curve and integral quantum efficiency can then be calculated by assuming $\Phi_{e,\lambda}$ is well approximated by the radioluminescence intensity spectrum as measured using the techniques described in Section 4.2.1. Notice that an assumption that the light collection efficiency is not spectrally sensitive has been made, thus ε can be considered a constant for all wavelengths and is not considered in the integration step. Figure 4.6 plots the spectral sensitivity of a Photonis XP5301 photocathode [71] alongside the radioluminescence spectrum of undoped CeBr₃ as an example.

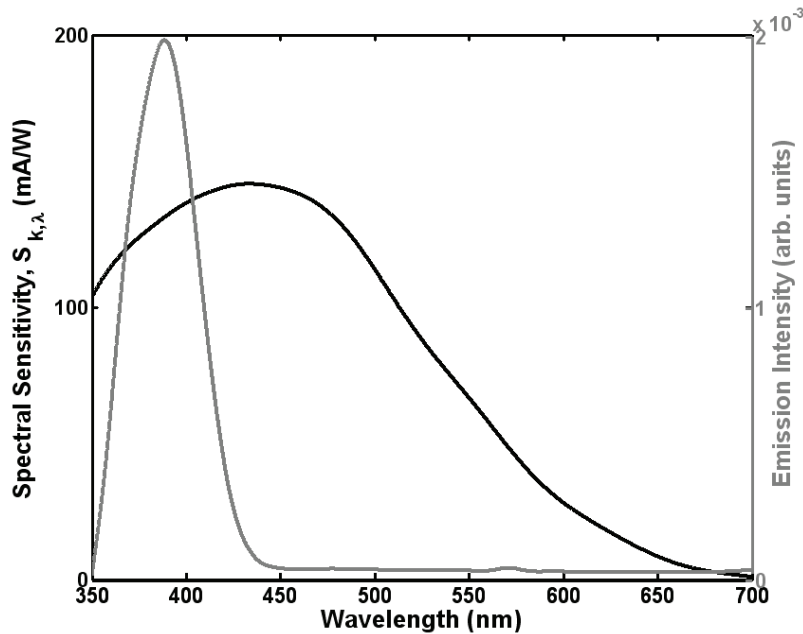


Figure 4.6. Spectral sensitivity of a Photonis XP5301 photocathode and the measured radioluminescence spectrum of undoped CeBr₃ plotted against wavelength.

The amount of charge collected at the anode of the PMT (Q) was assumed to be directly proportional to the peak height of the voltage pulse input (V) into the MCA. The response of an MCA (Pk), on the other hand, is linearly related to V by an equation of the form

$$Pk = MV + b, \quad (4.4)$$

where M is a gain coefficient and b is the offset. By calibrating the MCA with a precision pulser as shown in Figure 4.7, both M and b can be determined experimentally by a least squares fit. For the particular MCA used, a pulser calibration determined that $M = 745.26 \text{chns}/V$ and $b = -46.777 \text{chns}$. This knowledge then allows V to be determined from Pk through

$$V = \frac{Pk - b}{M}. \quad (4.5)$$

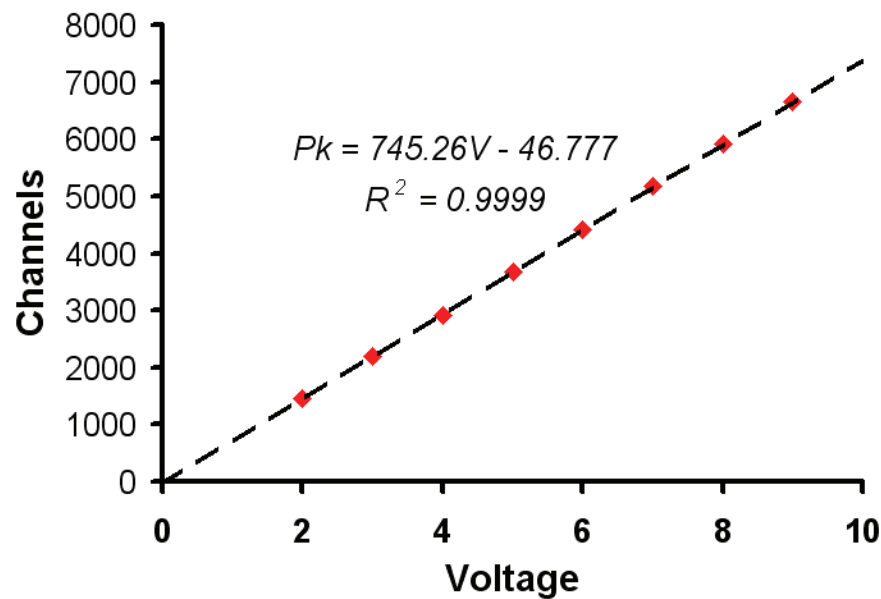


Figure 4.7. Calibration curve for the MCA.

Once V is known for both the unknown and known samples, the ratio of charges collected at the anode can be well approximated as the ratio of the input pulse heights since V and Q are directly proportional to one another, i.e.

$$\frac{V_x}{V_s} = \frac{Q_x}{Q_s}. \quad (4.6)$$

Eqn. (4.6) implies then that

$$Y_x = Y_s \left(\frac{\epsilon_s}{\epsilon_x} \right) \left(\frac{I_s}{I_x} \right) \left(\frac{V_x}{V_s} \right). \quad (4.7)$$

Eqns. (4.5) and (4.7), therefore, provide a method for estimating total light yield of an unknown sample of size differing from that of the standard known sample.

Estimating the light yield of an unknown thus required that γ -ray spectra with a known material and an unknown be acquired with identical gain settings and isotope. ^{137}Cs was chosen as the isotope as it is the standard energy to which relative light yields are referenced. BGO was chosen as the known standard as it is self-activated and well studied [72,78]. A self-activated, mature scintillator is ideal for comparison since the light yield is not likely to vary much from sample to sample.

The general procedure for estimating the light yield was rather simple. The known standard reference crystal was mounted to a PMT and a ^{137}Cs spectrum recorded. The known crystal was then removed and replaced with the unknown sample. A second ^{137}Cs spectrum was taken. All gain and high voltage settings used to acquire both spectra were held constant. The mode of the FEPs of each spectrum were recorded as Pk_s and Pk_x respectively. Previously computed light collection efficiency values and integral quantum efficiencies were finally used to calculate Y_x using Eqn. (4.7). The known reference BGO sample, which was 4mm thick, was assumed to have a total light yield of 6850 ph/MeV at 662keV as measured by Moszynski et al. [72].

Tested crystal samples included BGO, NaI:Tl, $\text{LaBr}_3\text{:Ce}$, undoped CeBr_3 and doped CeBr_3 . To measure a γ -ray spectrum, each sample was first dried, hand-polished and coupled to the center of a Photonis XP5301 PMT window with Saint Gobain BC-630 optical grease. The amount of grease used was minimized such that just enough grease was present to fully contact the bottom face of the sample with little to no excess at the bottom edges. Samples were next covered with a single 3" long strip of 2" wide, military-grade Teflon tape. The Teflon tape was pulled tight on either edge of the PMT to form a sort of "umbrella" over the sample with only the top surface of the sample contacting the Teflon tape. A black plastic cap was next placed over

the face of the PMT and sealed with black tape. The completed PMT assembly was removed from the UDA glove box and moved to the radiation laboratory for measurements. A sketch of the completed PMT assembly is provided in Figure 4.8.

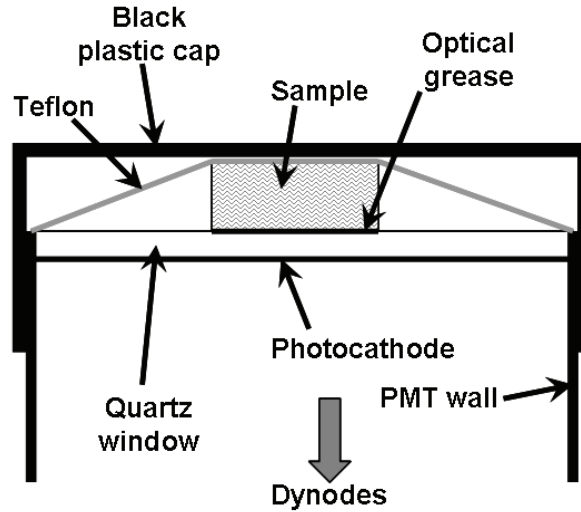


Figure 4.8. Cross-sectional sketch of a sample scintillator crystal mounted to the Photonis XP5301B PMT as used to estimate total light yield.

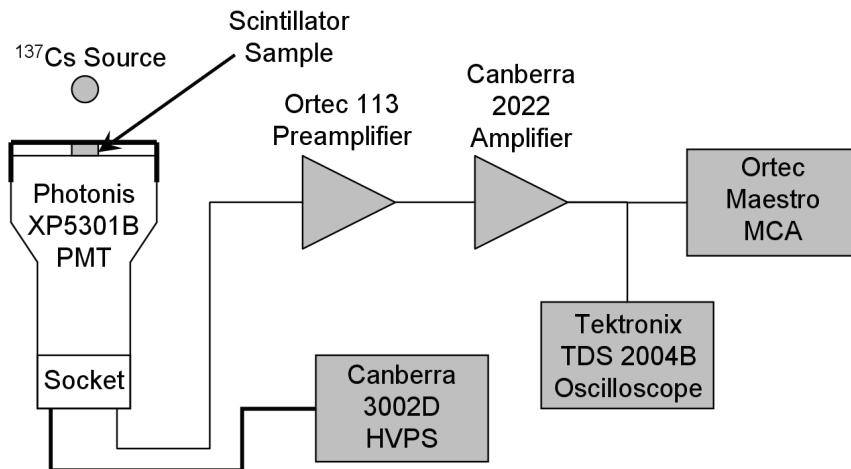


Figure 4.9. Diagram of the NIM setup used to collect γ -ray spectra for estimating the total light yield of an unknown.

Prior to measuring each γ -ray spectrum, the PMT assembly was connected to its voltage divider socket and wrapped entirely in aluminum foil. An aluminum foil wrap proved to be an excellent method to easily eliminate a significant amount of electro-magnetic interference, while

also helping to eliminate light leaks. The PMT/socket assembly was finally connected to the NIM system as shown in Figure 4.9.

A setting of 200pF on the variable-capacitance preamplifier was found to provide the best energy resolution. High voltage was always set to 800V as recommended by the PMT manufacturer. The amplifier gain was adjusted so that the FEP of the highest light yield sample (LaBr₃:Ce) was at ~85-90% of the full MCA range. Since the MCA is a quantized system, maximizing the gain helped to expand features and minimize measurement errors.

BGO is known to fluoresce under normal fluorescent lighting and have a long light decay constant on the order of hours. Therefore, the BGO sample was always stored in a light-tight container when room lights were on and mounted under red, incandescent lighting. This fluorescence phenomenon with BGO was observed when mounted under normal fluorescent lighting, but not observed when mounted under red, incandescent lighting. NaI:Tl and all Ce-activated or based materials were not observed to exhibit any long decay fluorescence, thus were mounted under normal fluorescent lighting.

Concurrent to total light yield estimations as described above, the collected γ -ray spectra also yielded information regarding each sample's energy resolution at 662keV. Coupling capacitance, PMT bias, and amplifier shaping times were all initially optimized for a sample of LaBr₃:Ce. Energy resolutions produced by the samples are ultimately a product of the sample preparation and mounting on top of the intrinsic properties of the material. Therefore, the energy resolutions collected were simply upper bounds to that achievable with a given material and not particularly useful in determining the effects of dopants.

4.2.3 Relative Light Yield Proportionality

The channel number recorded in an MCA (PH) is linearly related to the height of the pulse input into the MCA (V) in the manner

$$PH = MV + b. \tag{4.8}$$

Utilizing Eqn. (4.8) with experimentally determined gain M and offset b , the input pulse heights for any recorded count can be found. The height of the pulse, though, is directly proportional to the charge collected at the anode of the PMT (Q).

The pulse height V_L produced by a scintillator/PMT system when a γ -ray deposits energy E_{dep} is given by

$$V_L = E_{dep} Y(E_{dep}) \varepsilon I G_{PMT} G_{L,e}, \quad (4.9)$$

where $Y(E_{dep})$, ε and I are the total light yield at E_{dep} , light collection efficiency and integral quantum efficiency as previously defined. G_{PMT} is the PMT gain and $G_{L,e}$ is the cumulative gain in the NIM system up to the MCA input. First, it is recognized that $Y(E_{dep})$ can be split into two components,

$$Y(E_{dep}) = R(E_{dep}) Y(662keV) \quad (4.10)$$

where $R(E_{dep})$ is defined as

$$R(E_{dep}) = \frac{Y(E_{dep})}{Y(662keV)} \quad (4.11)$$

and $Y(662keV)$ is the absolute total light yield at 662keV and $Y(E_{dep})$ is the absolute total light yield at energy E_{dep} . Substituting Eqn. (4.11) into Eqn. (4.10) and defining

$$G'_L = \varepsilon I G_{PMT} G_{L,e} Y(662keV), \quad (4.12)$$

thus yields

$$V_L = E_{dep} G'_L R(E_{dep}). \quad (4.13)$$

A high purity germanium (HPGe) detector, on the other hand, produces a pulse height V_G when energy E_{dep} is deposited according to

$$V_G = \frac{E_{dep}}{E_w} \varepsilon_{CCE} G_{G,e} \quad (4.14)$$

where E_w is the average energy required to create an electron-hole pair, ε_{CCE} is the charge collection efficiency of the semiconductor device and $G_{G,e}$ is the cumulative gain of the HPGe NIM electronics through the MCA. Again, to simplify, define

$$G'_G = \frac{\varepsilon_{CCE} G_{G,e}}{E_w}, \quad (4.15)$$

so that Eqn. (4.14) becomes

$$V_G = E_{dep} G'_G. \quad (4.16)$$

G'_L can be readily determined experimentally by recognizing that for $E_{dep} = 662keV$,

$$G'_L = \frac{V_L(662keV)}{662keV} \quad (4.17)$$

since $R(662keV) \equiv 1$. Similarly, for the HPGe system,

$$G'_G = \frac{V_G(662keV)}{662keV}. \quad (4.18)$$

Since both $V_L(662keV)$ and $V_G(662keV)$ have some inherent variance, the mode pulse height is used, $\bar{V}_L(662keV)$ and $\bar{V}_G(662keV)$ respectively, which are simply the modes of the FEPs of each detector when irradiated with ^{137}Cs . Eqns. (4.17) and (4.18) thus become

$$G'_L = \frac{\bar{V}_L(662keV)}{662keV} \quad (4.19)$$

and

$$G'_G = \frac{\bar{V}_G(662keV)}{662keV}. \quad (4.20)$$

Once G'_L and G'_G have been determined by simply recording the FEP modes of ^{137}Cs spectra in each system, $R(E_{dep})$ can be measured for a range of energies by placing a scintillator/PMT system in coincidence with a HPGe system. The geometry between the two detector systems is designed such that γ -rays with energy E_γ from a stationary isotopic source enter into the scintillator and Compton scatter into the HPGe detector. For a successful coincident Compton scatter event, energy E_e is deposited in the scintillator while E'_γ is deposited in the HPGe detector volume. Compton scattering is an elastic process, thus

$$E_\gamma = E'_\gamma + E_e. \quad (4.21)$$

The energy deposited in the scintillator system produces a pulse height of

$$V_L = E_e G'_L R(E_e), \quad (4.22)$$

while the scattered γ -ray energy deposited in the HPGe system produces a pulse height of

$$V_G = E'_\gamma G'_G. \quad (4.23)$$

Both V_L and V_G are recorded for the coincident event. Finally, for each coincident event, $R(E_e)$ is found by substituting Eqn. (4.22) and Eqn. (4.23) into Eqn. (4.21),

$$R(E_e) = \frac{V_L}{G'_L \left(E_\gamma - \frac{V_G}{G'_G} \right)}. \quad (4.24)$$

Example A.1 in Appendix A illustrates the use of Eqn. (4.19) through Eqn. (4.24) to determine the relative light yield for a single pair of recorded coincident pulses.

A system was designed and constructed to record series of coincidence events. Since the above derivation eliminates the need to tightly control scattering angles, the system was designed to maximize the probability of capturing the scattered γ -ray. Two arrangements of the source and sample were utilized to capture data over the entire range of scatter angles from 0° to 180° .

The first geometry was designed to capture low angle scatters, ranging from 0° to approximately 115° and is illustrated in Figure 4.10. In this arrangement, the half-cylinder sealed source was placed directly next to the sample on the PMT window. The HPGe detector was then placed such that the scintillator sample lay directly between the source and itself. This arrangement proved to be advantageous to other published systems [79] as the solid angle between the source and sample was many times greater providing significantly improved efficiency. Further, the solid angle between the scintillator sample and the HPGe detector was also improved over conventional arrangements [79]. This simple improvement benefited the speed of acquisition in two ways. First, the larger solid angle ensured scattered γ -rays were more likely to enter the HPGe detection volume. Second, the larger solid angle provided data across a greater range of scatter angles. A typical $10 \times 10 \times 5$ mm sample placed at the center of the 3" PMT with the source 1 mm away allowed for scatter angles ranging from 0° to approximately 115° to be collected simultaneously.

Coincidence data for large scatter angles was collected using a second source-sample arrangement shown in Figure 4.11. In this second arrangement, the source was placed directly above the scintillator sample so that the mode scatter angle would be near 90° . However, the available scatter angles which would provide valid coincidence data ranged from about 15° up to 180° given to the close proximities of the source, sample and HPGe detector.

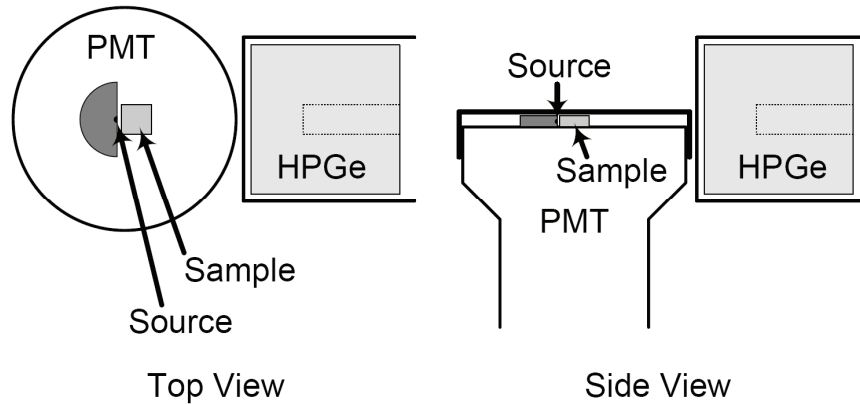


Figure 4.10. Top and side view sketches of the source-sample geometry for low angle scatter data acquisition.

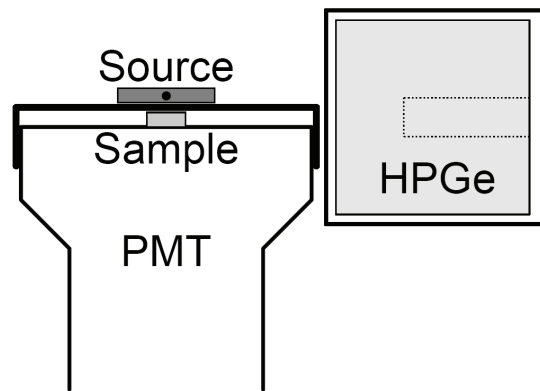


Figure 4.11. Sketch of the source-sample geometry for high angle scatter data acquisition.

The first source-sample arrangement, however, provided the bulk of the needed information since deposited energy in the scintillator does not change much with respect to scatter angle in the high angle regime as illustrated in Figure 4.12. The low angle arrangement was capable of providing data up to approximately 70° , which corresponds to a relative light yield energy range from 0keV to ~ 300 keV. Adding high angle scatter data only gains an additional 170keV of information. Furthermore, non-proportionality in light yield is generally not observed to be significant above about 100keV. The low angle scatter arrangement alone easily covered the interesting range of energies.

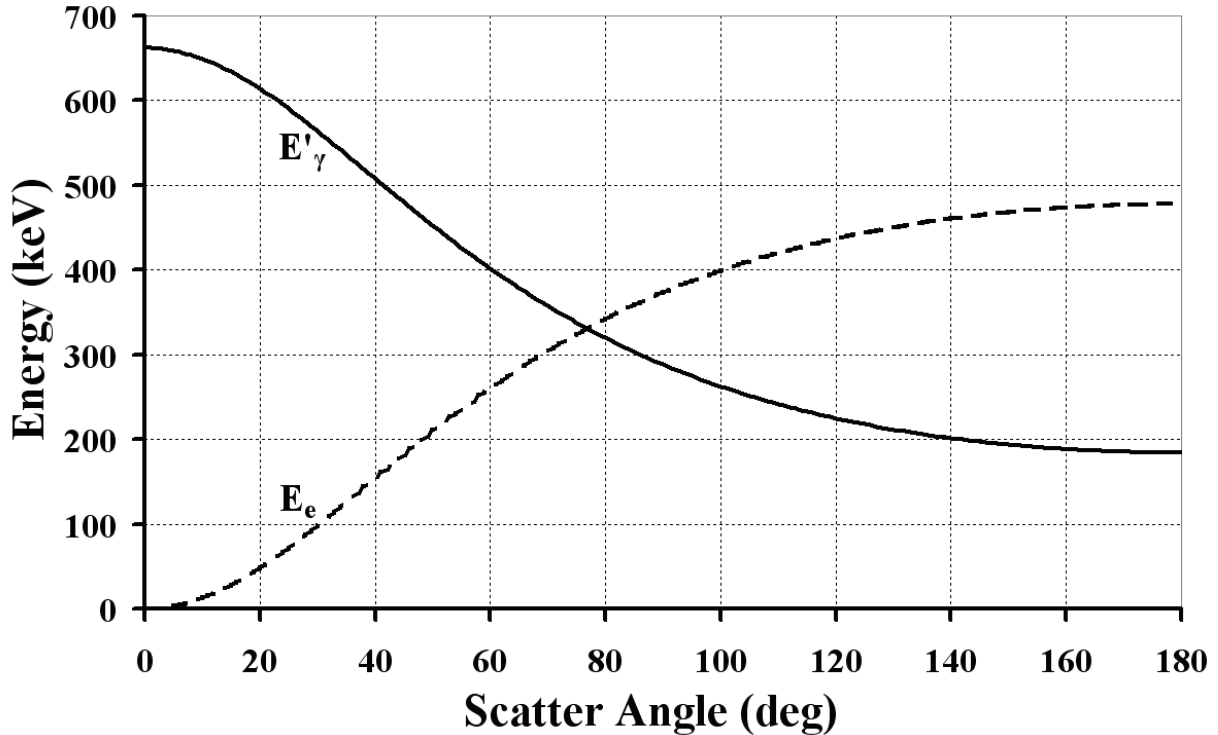


Figure 4.12. Plot of the energy deposited E_e and scattered γ -ray energy E'_γ against scatter angle for Compton scatters for an original γ -ray energy E_γ of 662keV.

NIM and CAMAC electronics were connected to a Canberra HPGe detector and a scintillator detector as shown in Figure 4.13 to form a system referred to as the relative light yield coincidence system (RLY system). The RLY system basically monitored the timing signals from each detector. When timing signals above a user set threshold value from both detectors fell within a specified time period, the events were considered 'coincident'. A coincidence event then triggered the ADC to capture and record the pulse heights of both spectroscopic signals and store them along with their time difference to a FIFO buffer in the CAMAC controller. Periodically, the personal computer (PC) queried the FIFO buffer, transferred the stored data sets and recorded the data in ASCII format to the hard drive. The ASCII formatted output file contained a single column of data. Every seven rows was a set of data providing a single relative light yield data point. The rows within each data set were designated as a header, the HPGe pulse height (chn), the PMT pulse height (chn), the HPGe time (clock cycles), the PMT time (clock cycles), and two internal diagnostic flags. Each clock cycle in the system was equivalent to 5ns.

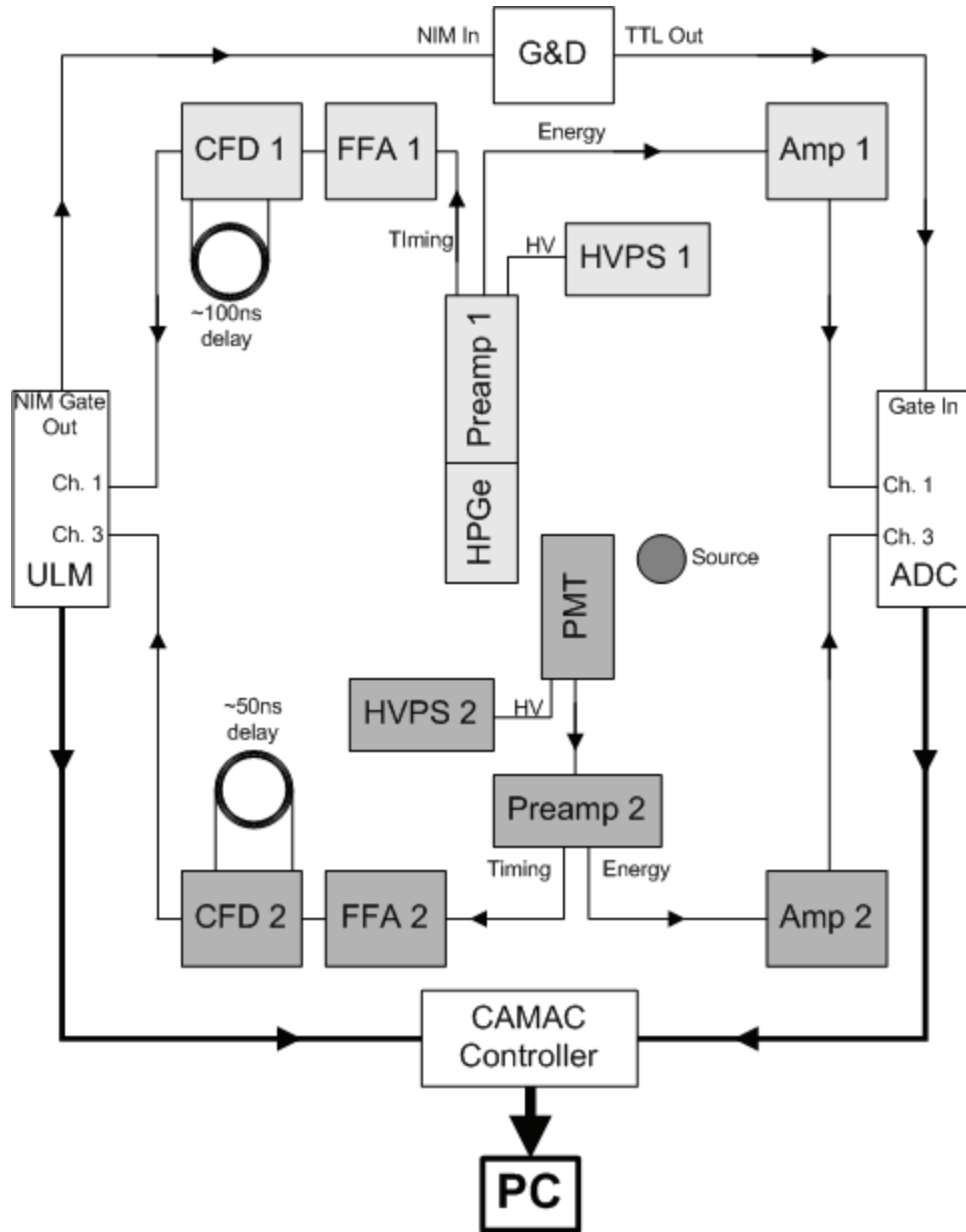


Figure 4.13. Connection diagram for the relative light yield coincidence system. Table 4.2 provides cross-references to equipment information for the above abbreviations.

A custom execution software code written by CMC controlled the data querying and storage process. The program allowed the user to either set the total data collection time or the number of desired data sets. Additionally, the execution software allowed the user to specify whether the system would capture coincidence data from both detectors for relative light yield measurements (Coinc), all pulse heights from the HPGe detector for G'_G measurements (HPGe singles), or all pulse heights from the PMT for G'_L measurements (PMT singles). Alternating

between the three types of measurements allowed the system gains (G'_G and G'_L) to be periodically recorded for long coincidence measurements in which gain drift in either system could become problematic.

Table 4.2. RLY Coincidence System Equipment List.

System	Make	Model	Description	Abbrev.
HPGe	Canberra	GC5020	HPGe Detector	HPGe
	Canberra	7600SI	Cryostat	(none)
	Canberra	2002CSI	Preamplifier	Preamp 1
	Canberra	3106D	NIM HVPS	HVPS 1
	Ortec	579	NIM Fast filter amplifier	FFA 1
	Ortec	583B	NIM Constant Fraction Discriminator	CFD 1
	Canberra	2022	NIM Amplifier	Amp 1
Scintillator	Photonis	XP5301B	3" OD Photomultiplier tube	PMT
	Mesytec	MPR-1	Charge Integrating Preamplifier	Preamp 2
	Canberra	3002D	NIM HVPS	HVPS 2
	Ortec	579	NIM Fast filter amplifier	FFA 2
	Ortec	583B	NIM Constant Fraction Discriminator	CFD 2
	Ortec	672	NIM Spectroscopy amplifier	Amp 2
Common	Ortec	416A	NIM Gate and Delay Generator	G&D
	CMC	CMC206	CAMAC Universal Logic Module	ULM
	Ortec	AD413A	CAMAC Quad 8K ADC	ADC
	CMC	CMC100	CAMAC Crate Controller	Controller
Not Shown	Sparrow	1000	CAMAC minirate	(none)
	Ortec	4001C	NIM bin	(none)

An example of how data sets were collected, corrected and concatenated is shown in Table 4.3. Collection typically occurred in cycles in which a set of HPGe Singles, PMT Singles and Coinc data were collected immediately following one another. In this example, four collection cycles were completed with a total of four hours of coincidence data collected. Gain data was collected at 65 min intervals. Each row in the table in **Error! Reference source not found.** was saved as a single ASCII formatted data file. The data collected in each of the Singles rows was plotted in a γ -ray spectrum. Examples of Singles spectra for the PMT and the HPGe detector are shown in Figure 4.14 and Figure 4.15. A peak-finding algorithm was then applied and a cubic smoothing spline fit to the data near the peak to find $Pk_L(662keV)_{(i)}$, or

$Pk_G(662keV)_{\{i\}}$ for that time period. $Pk_L(662keV)_{\{i\}}$ or $Pk_G(662keV)_{\{i\}}$ were then used to calculate $G'_{L,\{i\}}$ or $G'_{G,\{i\}}$ respectively for the i^{th} collection cycle denoted by the bracketed subscript.

Table 4.3. Diagram illustrating how four collection cycles are used to collect data sets which are subsequently corrected for gain drift and concatenated to produce a final set of relative light yield data as a function of deposited energy.

Mode	Exit	Measurement
HPGe Singles	5 min	$Pk_{G,\{1\}} \Rightarrow G'_{G,\{1\}}$
PMT Singles	5 min	$Pk_{L,\{1\}} \Rightarrow G'_{L,\{1\}}$
Coincidence	60 min	$PH_{G,\{1\}}, PH_{L,\{1\}}, \bar{t}_{G,\{1\}}, \bar{t}_{L,\{1\}}$
HPGe Singles	5 min	$Pk_{G,\{2\}} \Rightarrow G'_{G,\{2\}}$
PMT Singles	5 min	$Pk_{L,\{2\}} \Rightarrow G'_{L,\{2\}}$
Coincidence	60 min	$PH_{G,\{2\}}, PH_{L,\{2\}}, \bar{t}_{G,\{2\}}, \bar{t}_{L,\{2\}}$
HPGe Singles	5 min	$Pk_{G,\{3\}} \Rightarrow G'_{G,\{3\}}$
PMT Singles	5 min	$Pk_{L,\{3\}} \Rightarrow G'_{L,\{3\}}$
Coincidence	60 min	$PH_{G,\{3\}}, PH_{L,\{3\}}, \bar{t}_{G,\{3\}}, \bar{t}_{L,\{3\}}$
HPGe Singles	5 min	$Pk_{G,\{4\}} \Rightarrow G'_{G,\{4\}}$
PMT Singles	5 min	$Pk_{L,\{4\}} \Rightarrow G'_{L,\{4\}}$
Coincidence	60 min	$PH_{G,\{4\}}, PH_{L,\{4\}}, \bar{t}_{G,\{4\}}, \bar{t}_{L,\{4\}}$

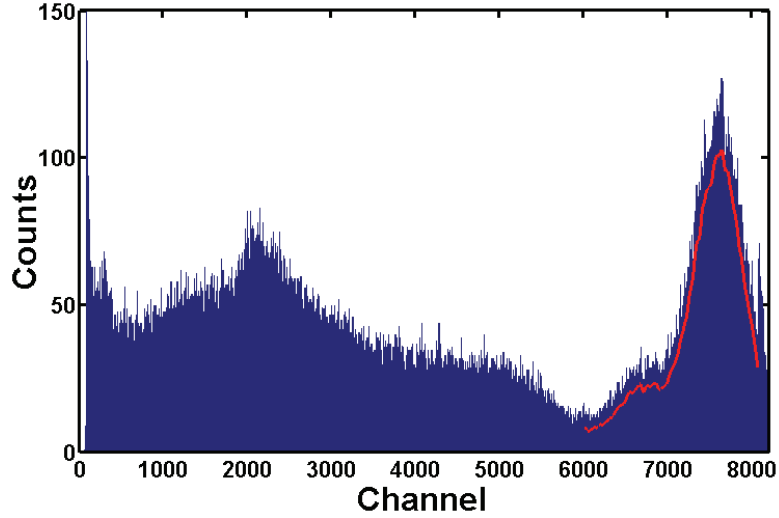


Figure 4.14. Example singles spectrum collected from the PMT. A smoothing spline (red) has been fit to the experimental data (dark blue) to more accurately determine the FEP mode.

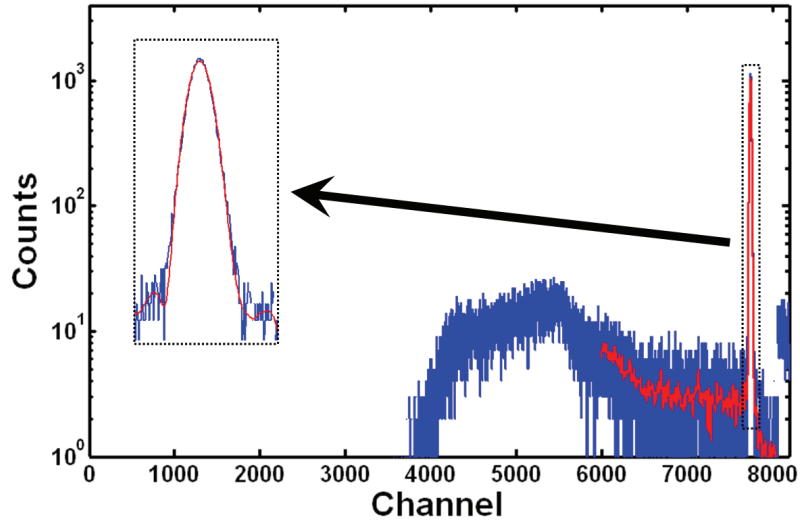


Figure 4.15. Example singles spectrum collected from the HPGe detector. A smoothing spline (red) has been fit to the experimental data (blue) to more accurately determine the FEP mode. An inset of the FEP is shown in the upper left to better show the FEP curve fit.

Coincident collections in each cycle produced arrays of $\overline{PH}_{G,\{i\}}$, $\overline{PH}_{L,\{i\}}$, $\bar{t}_{G,\{i\}}$, and $\bar{t}_{L,\{i\}}$. Here $\bar{t}_{G,\{i\}}$ and $\bar{t}_{L,\{i\}}$ were used to further sort data down even tighter coincidence limits than set manually in the electronics setup. $\overline{PH}_{G,\{i\}}$ and $\overline{PH}_{L,\{i\}}$ were used in conjunction with MCA calibration data and $G'_{L,\{i\}}$ and $G'_{G,\{i\}}$ to calculate arrays of relative light yield data $\bar{R}(E_e)_{\{i\}}$. Finally, all $\bar{R}(E_e)_{\{i\}}$ from each collection cycle were concatenated to form the final output data

array of $\bar{R}(E_e)$. These calculations were performed using a custom MATLAB code that is attached in Appendix A.

The final output data set $\bar{R}(E_e)$ was simply two columns of data with the first column being \bar{E}_e and the second being a corresponding value of $\bar{R}(E_e)$. Once data pairs of $\bar{R}(E_e)$ and \bar{E}_e were calculated, extensive data reduction was necessary. A two dimensional histogram of the data pairs, bins being defined in both the $\bar{R}(E_e)$ and \bar{E}_e dimensions, produced plots similar to the example shown in Figure 4.16 in which the frequency of counts in a single bin, $y_{cts}(E_e, R)$, are plotted. The data set clearly exhibits defined features, including a ridge. At higher energies, the ridge dies away to give way to a low RLY shelf due to events in which the scattered γ -ray entering the HPGe deposits only a portion of its energy via Compton scattering before escaping. A sharp peak near 180keV due to Compton scattering events which first occur in the HPGe detector before backscattering into the scintillator sample is also readily observable.

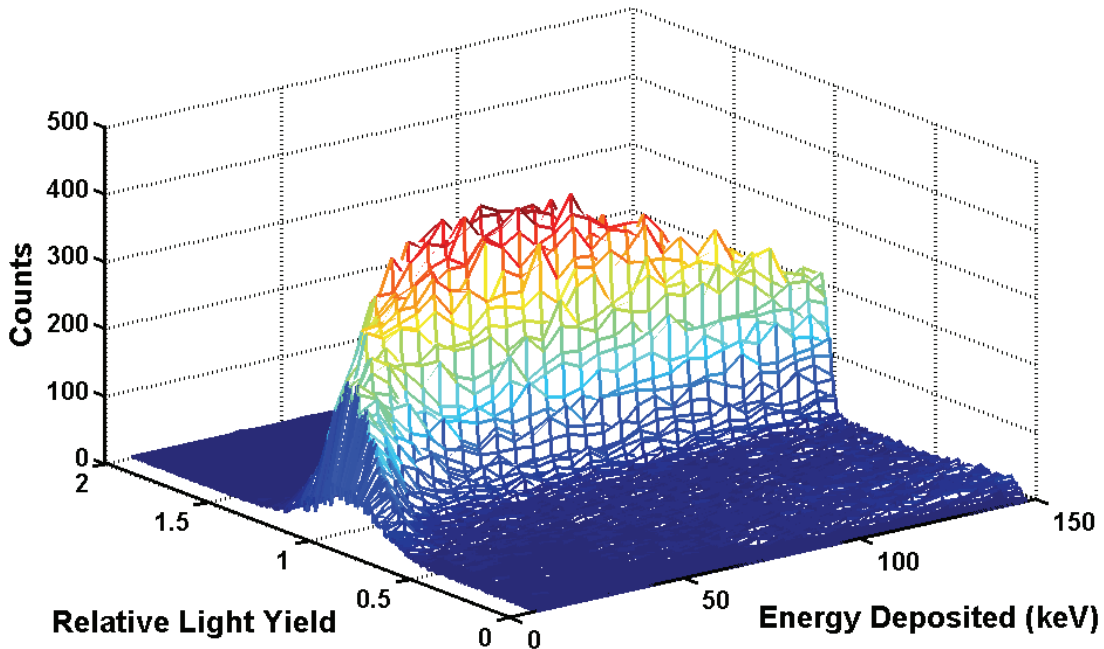


Figure 4.16. Example three dimensional surface plot of the data point density for 14hrs of coincidence data collected for BGO.

Taking single \bar{E}_e bins and plotting $y_{cts}(R)$ produced spectra like that shown in Figure 4.17. Since the data exhibits a stochastic spread, a smoothing spline was fit to each of the single \bar{E}_e bin data sets. The smoothing spline was used to determine first order estimates of the magnitude, mean and standard deviation of a Gaussian distribution. For the first order estimate of distribution mean, the mode of the smoothing spline was used. Figure 4.17 plots both the original histogrammed data and the smoothing spline for a single \bar{E}_e bin data set. The estimates for the Gaussian fit parameters garnered from the smoothing spline are denoted as well in Figure 4.17.

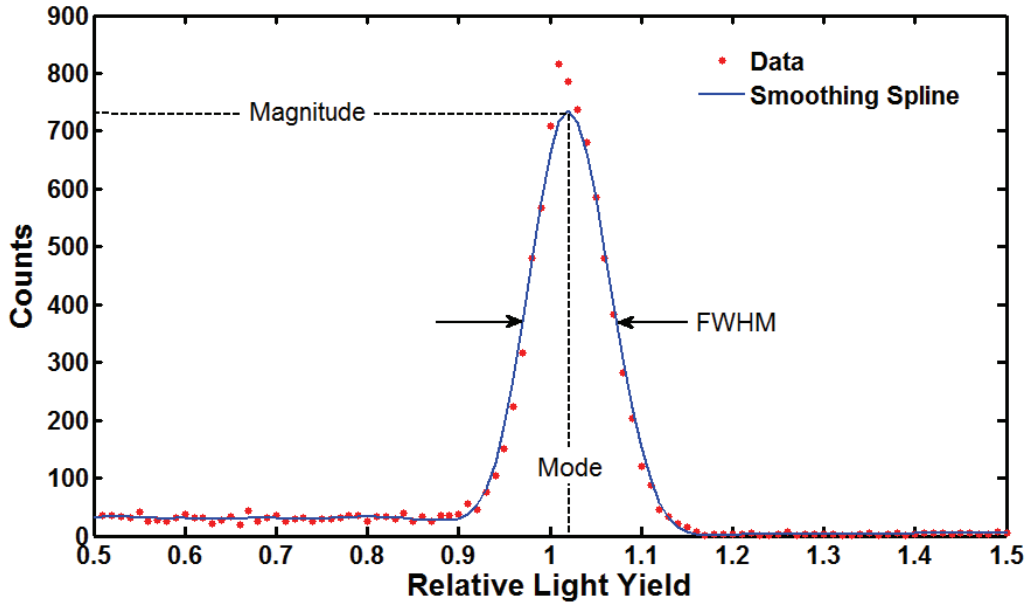


Figure 4.17. Example plot of the data from a single \bar{E}_e bin. Also shown are the corresponding smoothing spline fit.

In the next step of data reduction, a Gaussian distribution with a linear background was fit to each data set using [80]

$$y = a_1 \exp \left[-\frac{1}{2} \left(\frac{R - a_2}{a_3} \right)^2 \right] + a_4 + a_5 R \quad (4.25)$$

as the model equation, where a_1 , a_2 and a_3 represent the magnitude, the mean and standard deviation of the Gaussian distribution respectively. a_4 and a_5 are the offset and slope of the linear background. Eqn. (4.25) was fit to the data by minimizing the quantity [80]

$$\chi^2 = \sum \left[\frac{(y_{cts,i} - y(R_i))^2}{\text{var}(y_{cts,i})} \right], \quad (4.26)$$

where $y_{cts,i}$ are the number of counts collected in the RLY bin R_i , $\text{var}(y_{cts,i})$ is the variance about each $y_{cts,i}$ and $y(R_i)$ is the calculated number of counts in each RLY bin R_i as determined using Eqn. (4.25).

The minimization of χ^2 over the five-term parameter space was accomplished by repeated minimizations of χ^2 along each fitting parameter in turn. In this manner, χ^2 was first minimized by varying a_1 , then a_2 , a_3 , a_4 and lastly a_5 . This sequence of minimizations along each parameter was subsequently repeated until a local minimum was located. Finally, the values of a_2 and a_3 found to minimize χ^2 were determined to be the mean (μ_R) and standard deviation (σ_R) of the RLY at \bar{E}_e . The uncertainty in the estimate of the mean was calculated using

$$\sigma_{\bar{R}} = \frac{\sigma_R}{\sqrt{N}} \quad (4.27)$$

in which N is the number of counts as determined by numerical integration of Eqn. (4.25) minus the background counts. Figure 4.18 is a plot of $y_{cts}(R)$ alongside the theoretical fit of Eqn. (4.25) to the same data set presented in Figure 4.17.

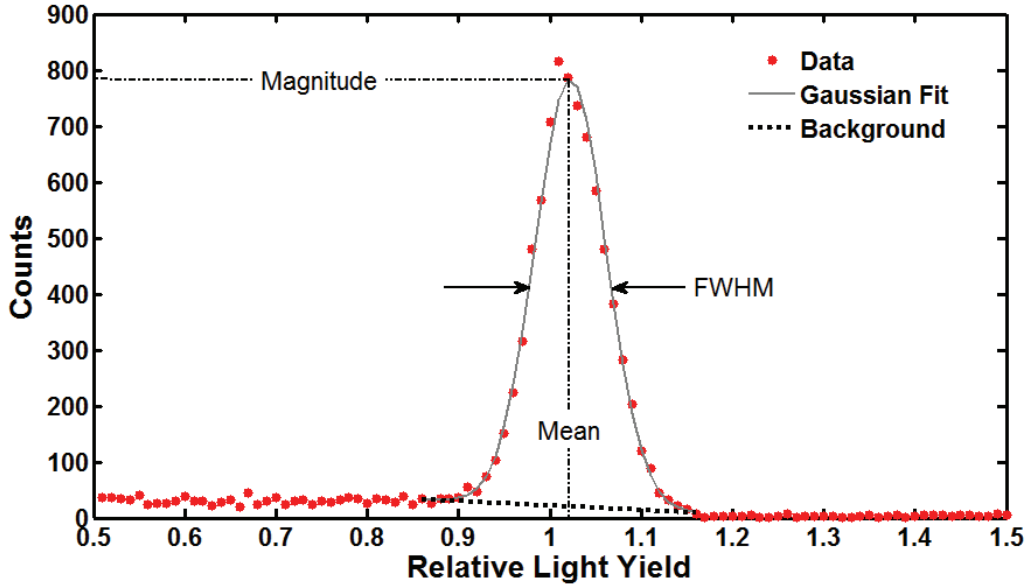


Figure 4.18. Example plot of the data from a single \bar{E}_e bin plotted alongside the best fit of Eqn. 4.25.

In Figure 4.19, the $\bar{R}(E_e)$ and \bar{E}_e data pairs were plotted in a scatter plot, then overlaid with points indicating μ_R and σ_R at each defined \bar{E}_e bin. Figure 4.20, on the other hand, plots the determined μ_R and $\sigma_{\bar{R}}$.

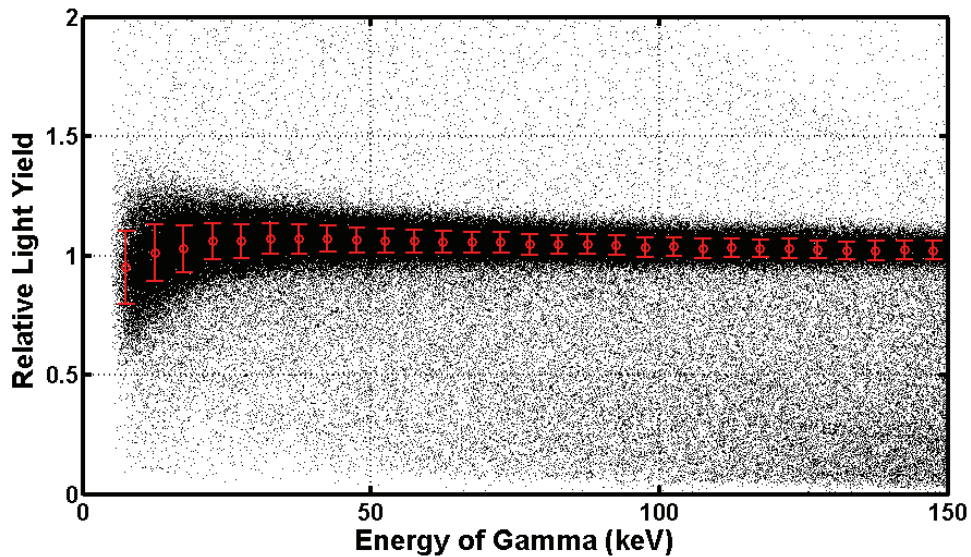


Figure 4.19. Example scatter plot of a final data set collected after analyzing several collection cycles of data from NaI:Tl. Also plotted are the estimated sample means for each \bar{E}_e bin along with the sample distribution standard deviation.

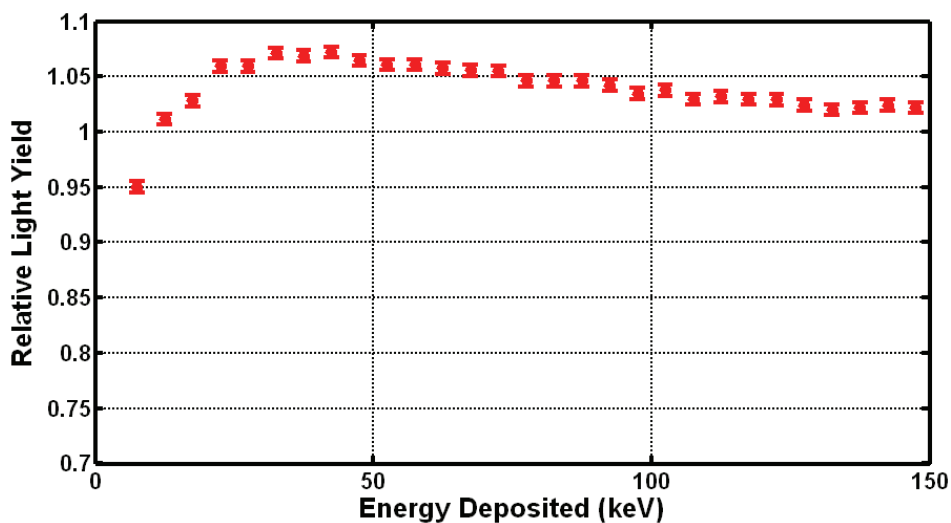


Figure 4.20. Example plot of relative light yields calculated at 5keV \bar{E}_e bin intervals for NaI:Tl. Error bars indicate the uncertainty in the estimated sample mean.

4.2.4 Decay Constants

A cursory check of the decay of the scintillation light pulse was performed for NaI:Tl, LaBr₃:Ce, undoped CeBr₃ and doped CeBr₃ samples. Absolute measurements of decay characteristics are typically performed using the Thomas-Bollinger method in which two PMTs are used to collect light from a single irradiated sample. The first PMT in such an experiment is tightly coupled to the scintillation crystal to collect a large amount of light. In contrast, the second PMT is very poorly coupled to the scintillation crystal, such that less than one photoelectron per scintillation event is produced. The well-coupled PMT is used to trigger the start of a timer, which records the time lapse until the coincident single photoelectron pulse from the poorly-coupled PMT is noted. Recording the time difference between pulses thus yields a series of data with a statistical distribution following the decay characteristics of the scintillator. While this method is preferable and most accurate, it requires a rather extensive experimental apparatus.

A simpler, less accurate method of determining decay characteristics is to observe the output pulse from a single PMT on an oscilloscope. The rise and fall of the pulse observed at the output of the PMT is strongly influenced by the scintillation crystal, assuming the PMT has a sufficiently fast response. While not an accurate method to directly measure the decay constant(s) of a scintillator material, observing the pulse output by a fast PMT does provide a

degree of material screening. A “fast” PMT has a short transit time, the time necessary to accelerate a photoelectron from the photocathode through the multiplying dynodes and reach the anode.

One key concern in doping a known high performance scintillator is whether the dopants adversely affect the timing characteristics. Directly observing the pulse from a PMT allows a quick check whether a dopant strongly influenced decay characteristics of a material. For instance, Figure 4.21 shows a comparison between a NaI:Tl pulse and an undoped CeBr₃ pulse. Indeed, for the data presented in Figure 4.21, a single decay constant equation fit to the decaying portions of the two pulses yields $\tau \approx 26ns$ for undoped CeBr₃ and $\tau \approx 285ns$ for NaI:Tl. Both decay constants are higher than published values (17ns and 250ns respectively) for each material as determined by Thomas-Bollinger measurements [45,70]. Nevertheless, it is quite easy to see that this simple method provides a quick check of decay characteristics and capable of detecting drastic changes to them.

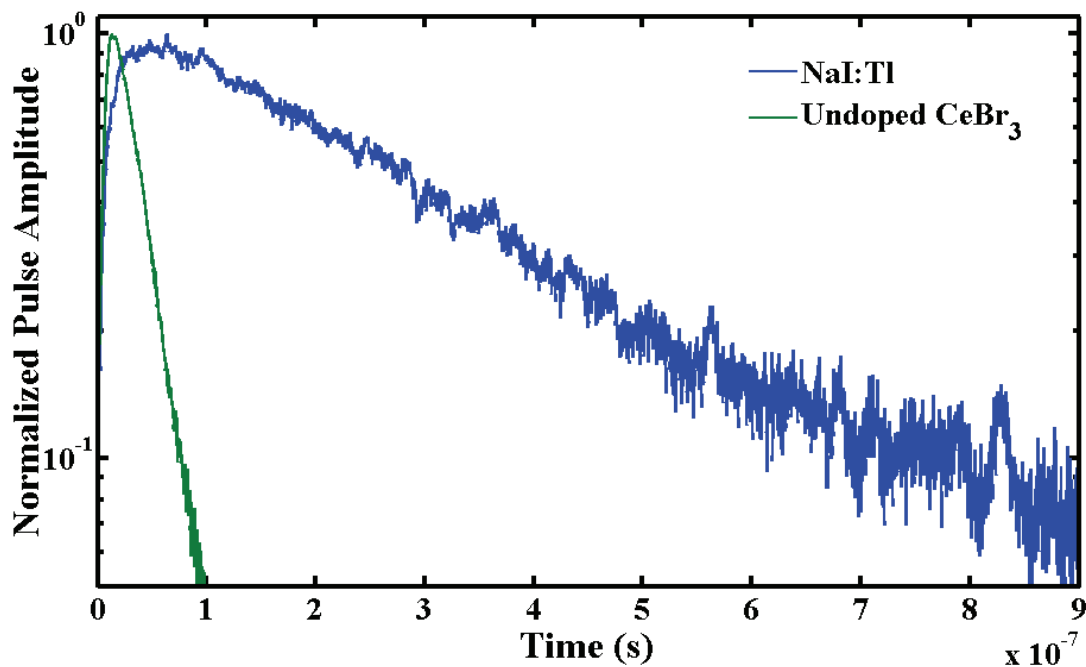


Figure 4.21. Comparison of the pulse shapes of NaI:Tl and undoped CeBr₃ as observed at the output of a Photonis XP5301B PMT.

Each sample was mounted to a Photonis XP5301B PMT as described previously and irradiated with ¹³⁷Cs. Bias was applied using a Canberra 3002D high voltage power supply. The

PMT output was then directly connected to the input of a Tektronix TDS2004B oscilloscope. The oscilloscope was set to only trigger on full energy pulses, i.e. above the Compton edge. Several pulses were acquired and saved to memory in comma-separated value (.csv) format. Finally, pulses were plotted and compared to undoped CeBr_3 to determine whether the dopants exhibited any strong effects on the decay dynamics of light emission.

5 Experimental Results

Observations and trends in the crystal growth and sample preparation processes are given in Section 5.1. Section 5.2 provides the measurements conducted on the various samples. Several results were surprising, such as crystal growth being so dramatically improved by the dopants. Other results were expected, such as the Pb^{2+} dopant quenching scintillation.

5.1 Crystal Growth

The horizontal gradient freeze (HGF) method of crystal growth was originally chosen for growing single crystalline samples of CeBr_3 as was expected to induce less thermal stress on the growing ingot. Unfortunately, several key flaws in the process hindered yields, despite initially promising results.

The first ingot grown to test the HGF method was $\text{LaBr}_3:\text{Ce}$ sealed in an ampoule by Aldrich APL. The ingot, HB1, exhibited crystal grains of reasonable size as shown in Figure 5.1. Often, ingots were photographed under UV lighting as the fluorescence of the ingot made the internal crystalline structure far easier to see. As a first trial, the HGF method appeared quite promising.

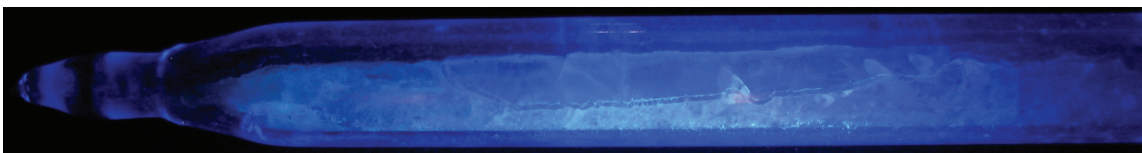


Figure 5.1. First ingot grown, HG1, with HGF method under UV lighting.

The first two trial growth runs with in-house sealed CeBr_3 , however, yielded significantly different results as shown in Figure 5.2. Ingot HB2 exhibited an orange discoloration, while HB3 was blackened. After several test ingots of CeBr_3 were prepared and processed, it was determined that the black discoloration in HB3 was the result of O_2 contamination during the sealing process. With greater care during sealing, the O_2 contamination issue was easily resolved.

The orange contamination, on the other hand, proved quite difficult to troubleshoot. X-ray fluorescence measurements showed the orange discoloration of HB2 was Br_2 , but the cause remained elusive for quite some time despite several attempts to eliminate potential causes. The orange discoloration, while not ideal, was deemed to be acceptable as the single crystals harvested from lightly discolored ingots exhibited no internal discoloration, i.e. the orange discoloration appeared to be only a surface problem, not internal. Therefore, the experiment was continued without resolution of the orange discoloration issue.



Figure 5.2. Ingots HB2 and HB3 under normal lighting.

Undoped ingots of CeBr_3 proved to be particular difficult to grow as large single crystals. Figure 5.3 shows a photograph of the crystalline structure of the highest yielding undoped ingot grown. Internal cracking was abundant in undoped CeBr_3 ingots and caused ingot yields to be incredibly low.



Figure 5.3. Ingot HB6, undoped CeBr_3 under normal light. Internal cracking prohibited harvesting useable samples.

Doped ingots of CeBr_3 , to the contrary, possessed far better crystalline structure. Figure 5.4 shows a photograph of one such doped ingot, HB22. Typically, doped ingots exhibited a single crystal across the entire cross-section at the tail, which had propagated and grown in cross-section from the nose. Figure 5.4 shows the single crystal at the tail in ingot HB22.

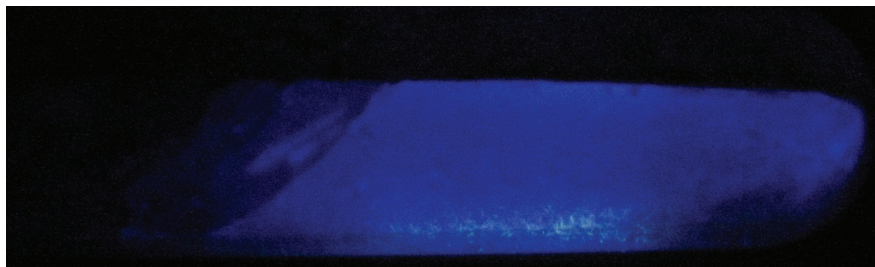


Figure 5.4. Ingot HB22, 1000ppm HfBr₄ doped CeBr₃ as photographed under UV lighting.

Overall, 32 ingots of doped and undoped CeBr₃ were grown. Dopant masses in Table 4.1 were targeted to achieve either 500ppm or 1000ppm of each dopant, but actual masses loaded varied due to the granularity of the dopants in many cases. Actual loaded masses and the resulting dopant atomic concentrations are given in Table 5.1. One run, designated as BHB1, used a much larger and longer ampoule, but was otherwise loaded and grown identically to the others. Ingot designations were not sequential as can be seen in Table 5.1, since a few other crystal growth runs were performed for other reasons.

Included in Table 5.1 are the number of samples harvested from each ingot and the overall quality of the samples. Many runs failed for various reasons, including oxygen contamination during sealing and equipment failures. Some ingots yielded no useable samples because of excess Br₂ liquid being entrained within the solid crystal, yielding orange-tinted crystals. Small amounts of Br₂ were tolerable as they did not affect crystalline transparency, but large excesses contaminated the melt and produced translucent crystals. It was not until after the crystal growth runs that the problem of Br₂ evolving out of the melt was solved.

In an effort to resolve the Br₂ contamination issue, a 200g sample of originally 99.999% pure CeBr₃ was loaded into a multi-chamber ampoule and vacuum distilled. The CeBr₃ powder, located in the lowest ampoule chamber as shown in Figure 5.5, was initially melted and held at 1030°C under a high vacuum ($<1 \times 10^{-5}$ Torr) for many hours. Indeed, Br₂ was observed to condense out of the turbo pump foreline in a LN₂ cold trap. CeBr₃ evaporated and condensed inside the second chamber, located just above the furnace. After six hours, approximately 160g of CeBr₃ was vacuum distilled into the second chamber. The furnace was then cooled to RT and dropped away from the ampoule. The bottom-most chamber containing residual material and low vapor pressure impurities was first flame sealed from the ampoule and removed. Next, the second chamber containing the distilled CeBr₃ was flame sealed and removed from the ampoule.

Table 5.1. Ingot masses, resulting dopant concentrations, and ingot results.

HB	Dopant	Concentration	Mass CeBr ₃	Mass Dopant	Samples	Quality
#		(ppm)	(g)	(mg)	#	
HB1	LaBr ₃ :Ce ampoule prepared by Aldrich APL				-	High
HB 2	None	0	150.004	-	0	Failed*
HB 3	Ca ²⁺	551	150.001	43.5	0	Failed**
HB 4	None	0	75.7	-	0	Failed*
HB 5	Ca ²⁺	558	150.005	44.0	2	Poor
HB 6	None	0	151.045	-	1	Poor
HB 7	Sr ²⁺	502	149.900	49.0	8	Good
HB 8	Zr ⁴⁺	580	149.900	94.1	7	Good
HB11	Hf ⁴⁺	714	139.931	131	0	Failed*
HB12	Zn ²⁺	577	139.943	47.9	0	Failed*
HB13	Cd ²⁺	595	139.973	59.7	0	Failed*
HB14	Hf ⁴⁺	574	139.964	105.2	1	Poor
HB15	Zn ²⁺	543	139.951	45.0	6	Good
HB17	Cd ²⁺	512	140.016	51.4	14	Good
HB18	Pb ²⁺	555	139.72	74.9	3	Good
HB19	Ca ²⁺	1016	140.112	74.9	2	Mediocre
HB20	Sr ²⁺	1145	140.317	104.7	0	Failed*
HB21	Zr ⁴⁺	1033	140.033	156.4	6	Good
HB22	Hf ⁴⁺	934	140.084	171.5	1	Mediocre
HB23	Zn ²⁺	1099	140.008	91.2	3	Poor
HB24	Cd ²⁺	1011	140.065	101.4	7	Good
HB26	None	0	140.001	-	0	Failed*
HB27	Ba ²⁺	824	140.017	90.2	8	Good
HB28	Ba ²⁺	505	140.099	55.3	0	Failed*
HB34	Ca ²⁺	934	140.026	68.8	5	Good
HB35	Sr ²⁺	1203	140.038	110.0	5	Good
HB36	Hf ⁴⁺	1093	140.015	200.8	3	Good
HB38	None	0	140.000	-	0	Failed***
HB39	None	0	140.143	-	0	Failed***
HB40	Ca ²⁺	475	140.125	35.0	1	Failed*
HB41	Ba ²⁺	502	140.453	55.1	4	Good
HB42	Ca ²⁺	973	140.502	71.9	5	Good
BHB1	Sr ²⁺	501	500	163.0	10	Good

* Ingot failed due to Br₂ evolution.

** Ingot failed due to O₂ contamination.

*** Ingot lost due to equipment failure.

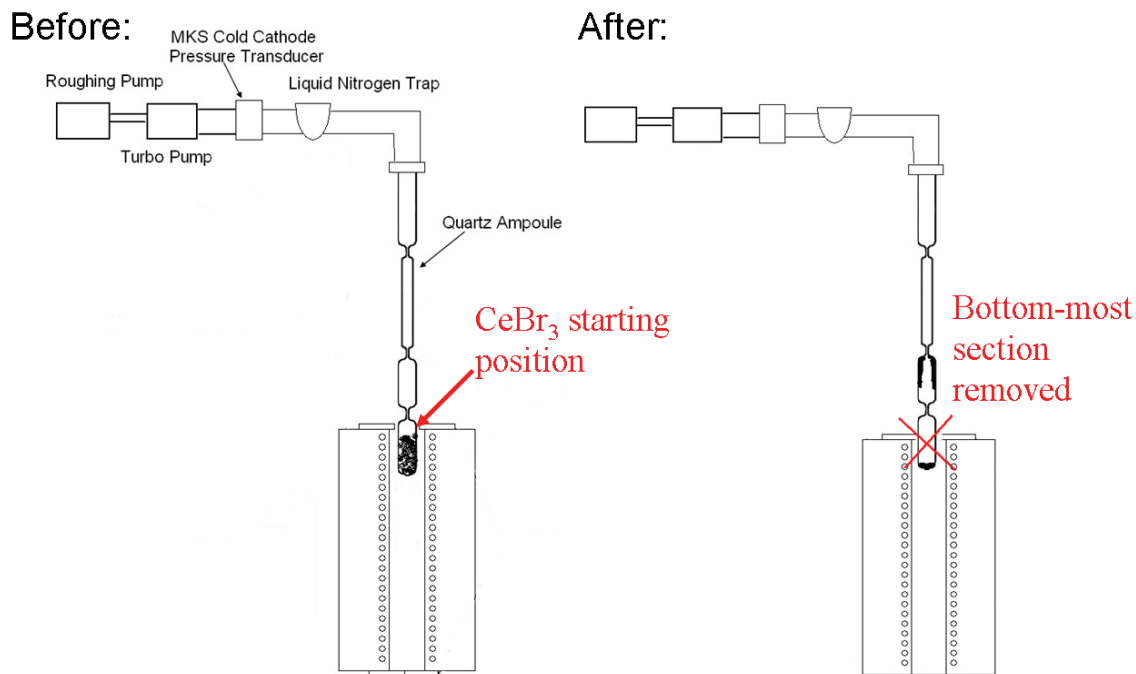


Figure 5.5. Sketch of the before distillation and after distillation states of the vacuum distillation system and ampoule.

The sealed second chamber was then placed inside a HGF EDG furnace and melted. A HGF crystal growth run was executed. Absolutely no Br_2 was observed in the as-grown, vacuum distilled ingot, indicating an unknown impurity was responsible for causing Br_2 to evolve from the melt during growth. Thermogravimetric studies [50] suggest Br_2 may be the by-product of water contamination decomposing the CeBr_3 to CeO_2 . Eradicating H_2O contamination from the ampoule prior to and during sealing therefore appears to be the key to eliminating Br_2 contamination of the as-grown ingot. If the above decomposition method is indeed occurring, vacuum distillation is likely an excellent method to remove the by-products of H_2 , Br_2 , HBr and CeO_2 from CeBr_3 as each possesses a vapor pressure many orders of magnitude different than CeBr_3 at distillation temperatures.

5.2 Characterization and Measurements

From the sample sets harvested from each ingot, the one or two highest quality samples from each dopant and concentration were further tested for scintillation performance. Radioluminescence spectra were first recorded from which $\Phi_{e,\lambda}$ could be estimated. Next, the

total light yield of each sample was estimated by comparing the γ -ray response to a BGO sample. Simultaneously, each sample's decay characteristics were observed and recorded on a digital oscilloscope. Finally, a representative sample from each dopant was selected for light yield proportionality measurement. The results of the measurements are provided in the following sections.

5.2.1 Radioluminescence Spectra

Radioluminescence data indicated that some dopants did in fact alter the emission spectrum of CeBr_3 . Emission spectra for BGO, NaI:Tl and $\text{LaBr}_3:\text{Ce}$ are shown in Figure 5.6. Emission spectra for each dopant type are provided in Figure 5.7 through Figure 5.14. Finally, a comparison between the radioluminescence spectra of HGF-grown, undoped CeBr_3 and vertical Bridgman-grown, undoped CeBr_3 is given in Figure 5.15.

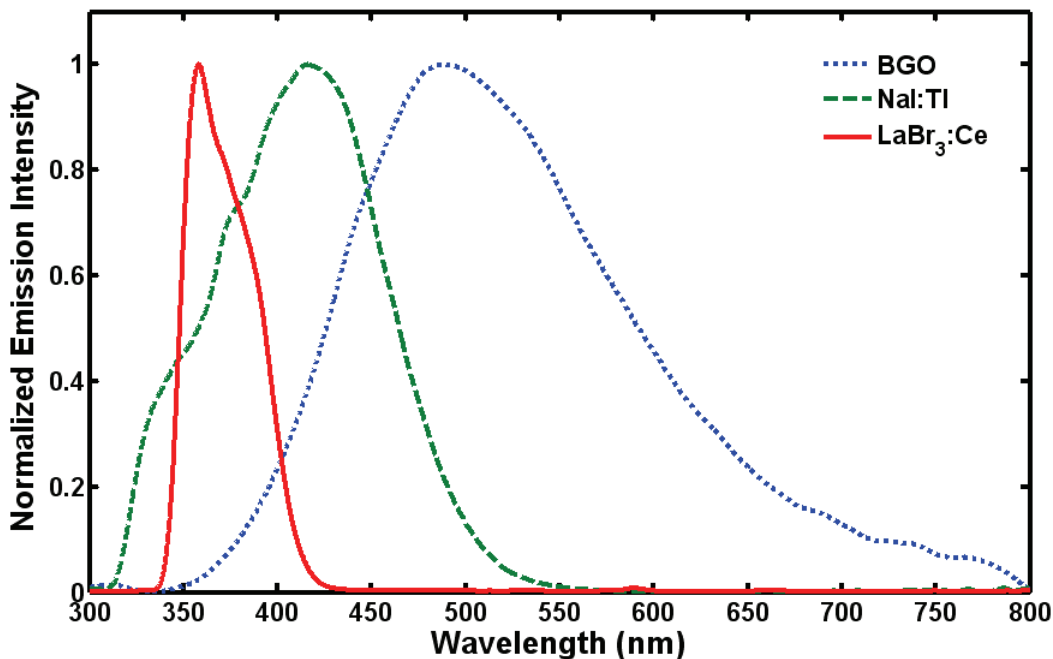


Figure 5.6. Collected radioluminescence emission spectra for BGO, NaI:Tl and $\text{LaBr}_3:\text{Ce}$

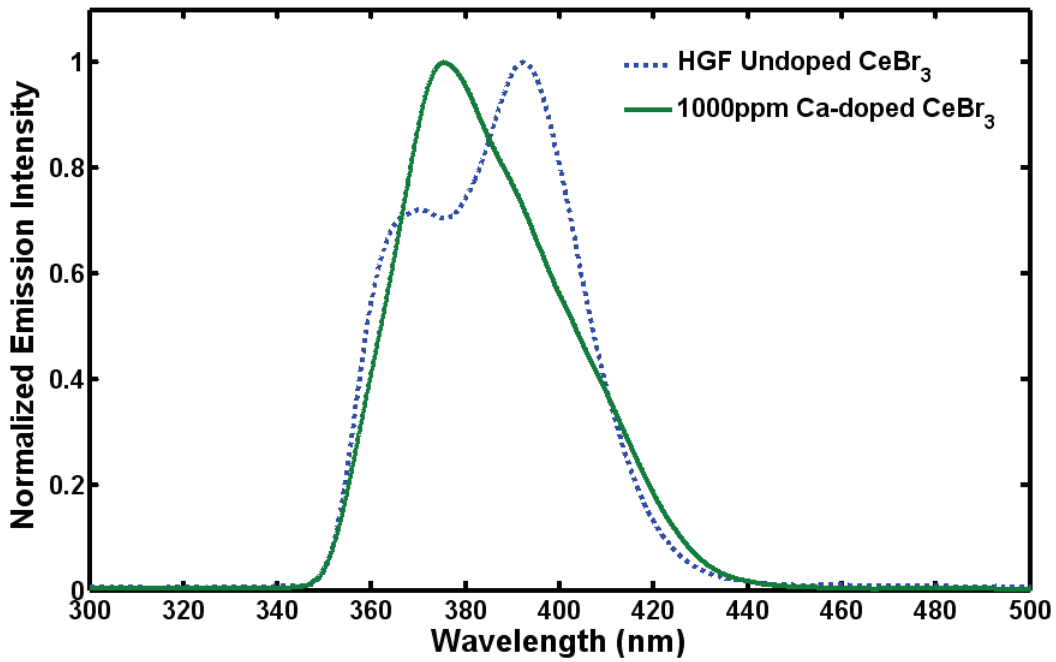


Figure 5.7. Collected radioluminescence emission spectra for 1000ppm Ca-doped and undoped CeBr₃.

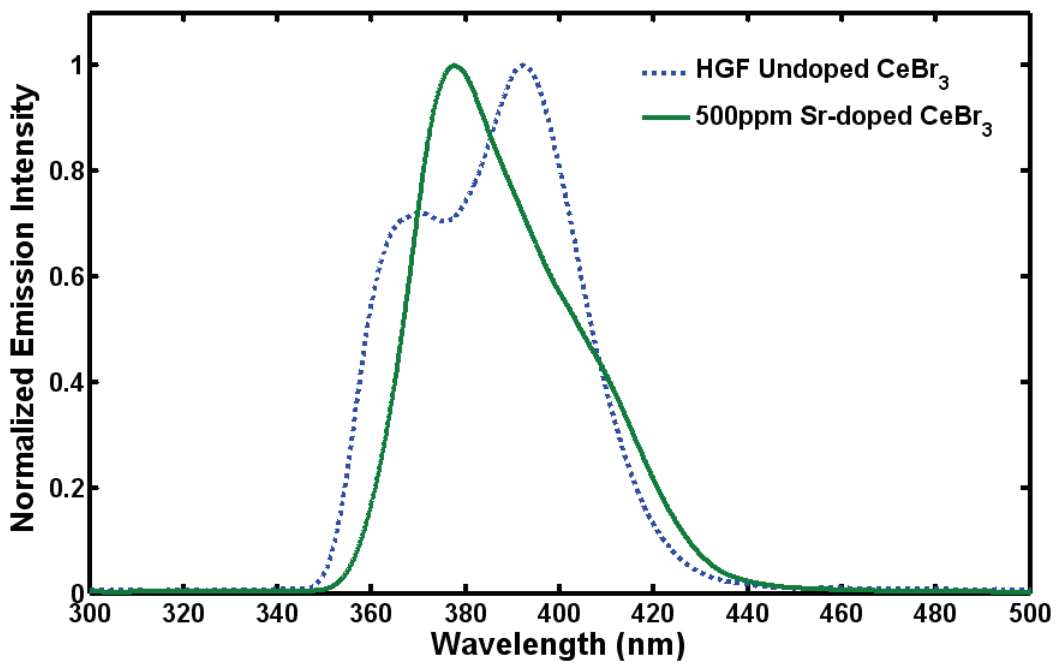


Figure 5.8. Collected radioluminescence emission spectra for 500ppm Sr-doped and undoped CeBr₃.

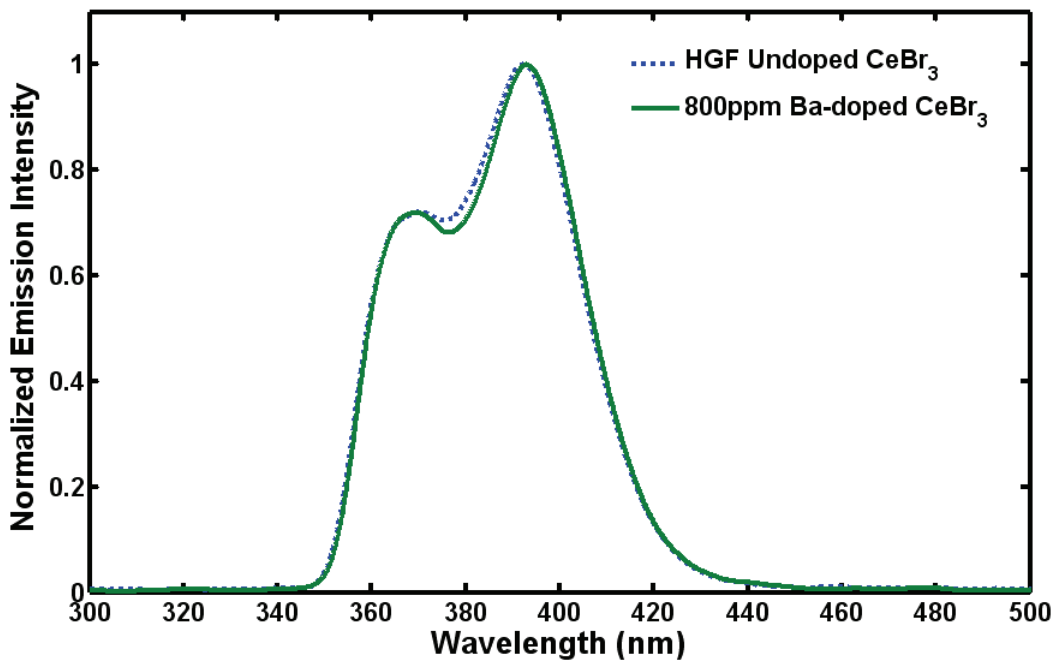


Figure 5.9. Collected radioluminescence emission spectra for 800ppm Ba-doped and undoped CeBr_3 .

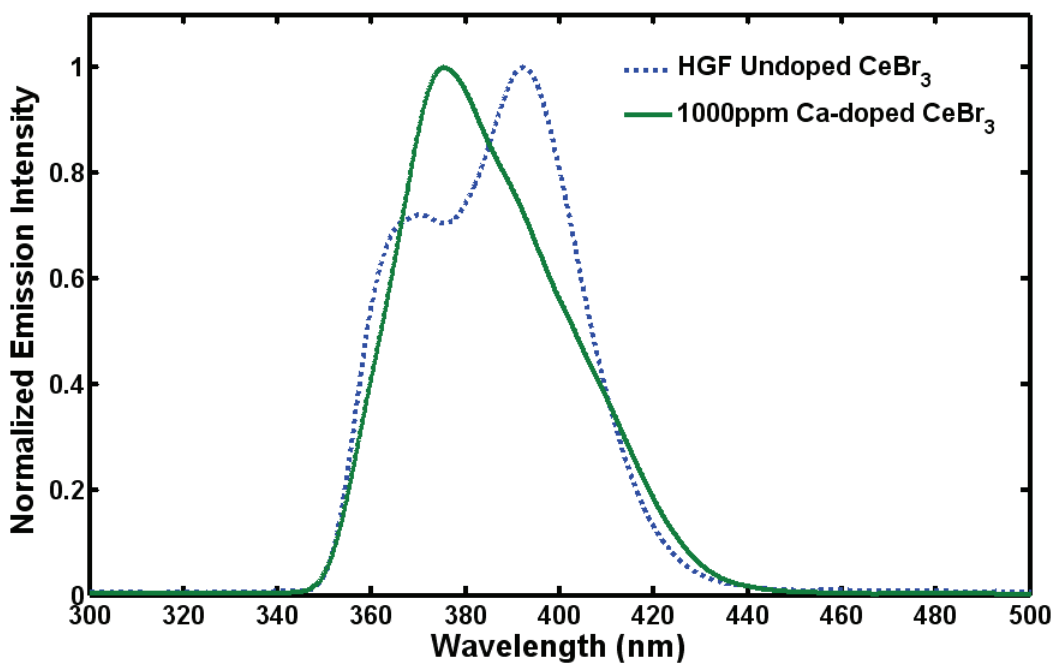


Figure 5.10. Collected radioluminescence emission spectra for 600ppm and 1000ppm Ca-doped and undoped CeBr_3 .

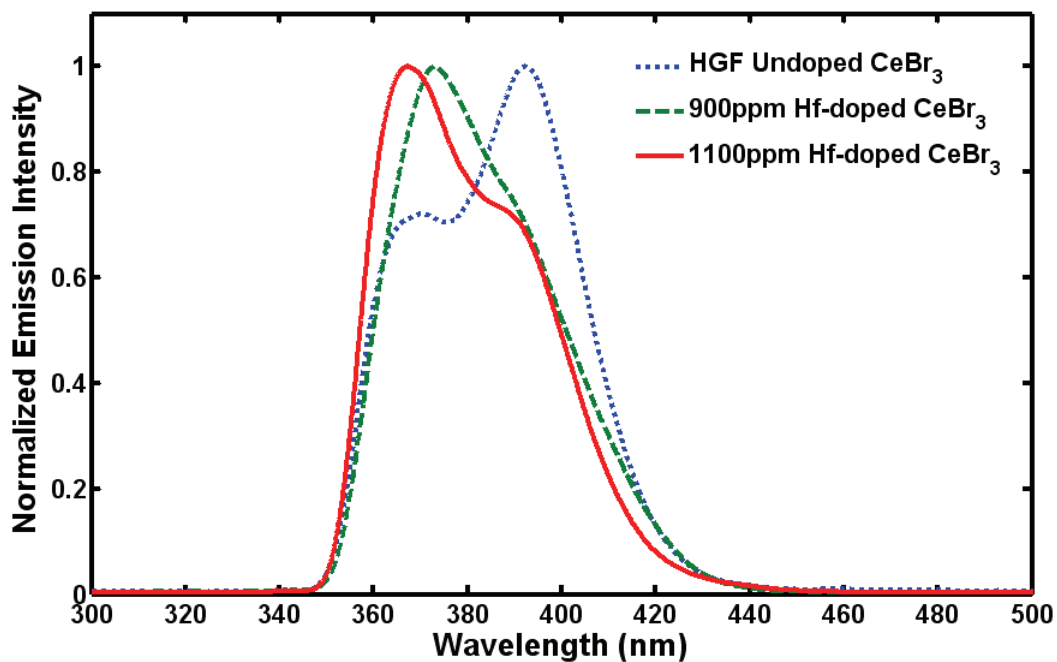


Figure 5.11. Collected radioluminescence emission spectra for 900ppm and 1100ppm Hf-doped and undoped CeBr_3 .

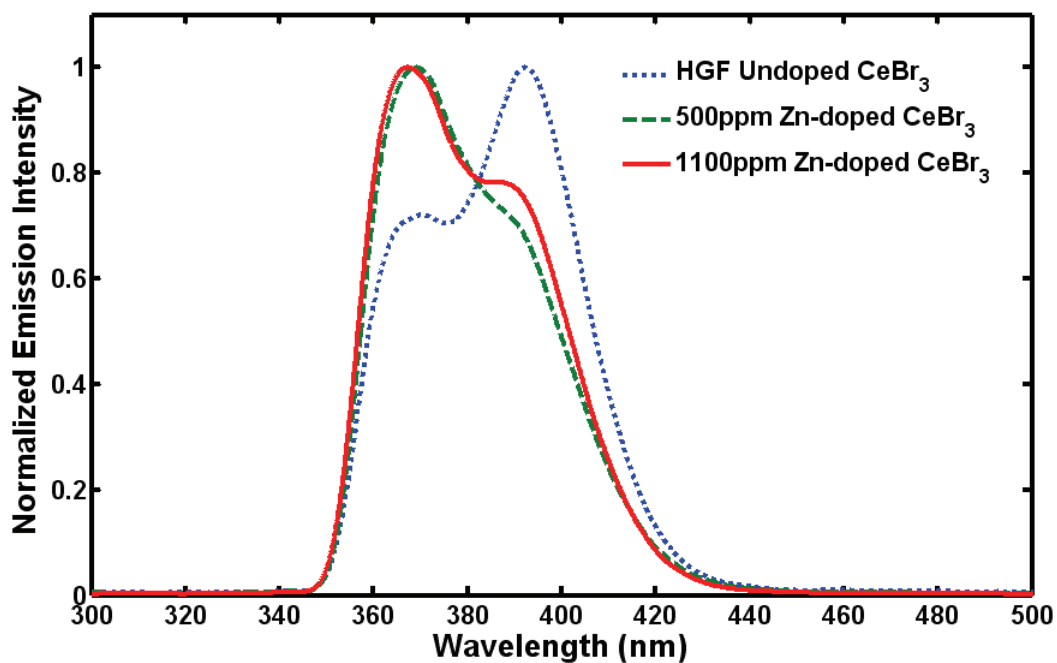


Figure 5.12. Collected radioluminescence emission spectra for 500ppm and 1100ppm Zn-doped and undoped CeBr_3 .

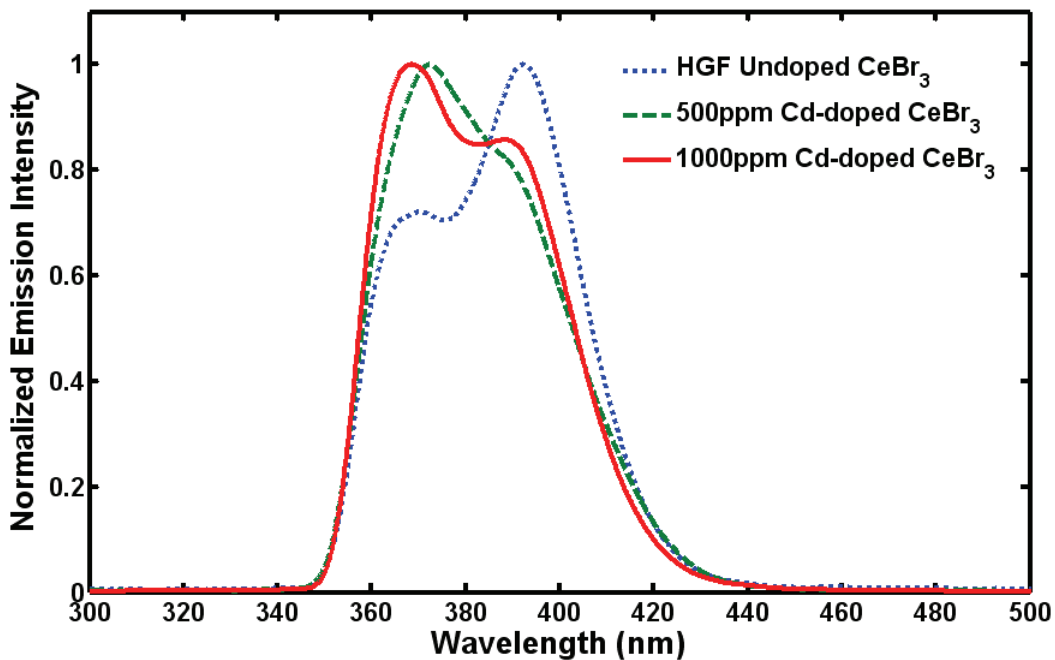


Figure 5.13. Collected radioluminescence emission spectra for 500ppm and 1000ppm Cd-doped and undoped CeBr₃.

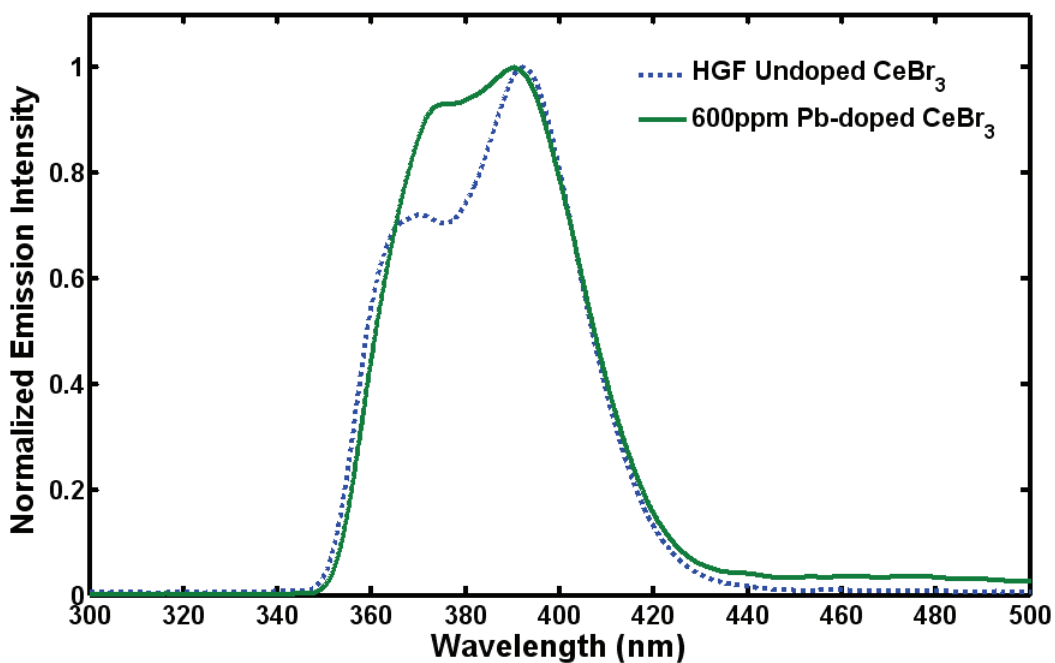


Figure 5.14. Collected radioluminescence emission spectra for 600ppm Pb-doped and undoped CeBr₃.

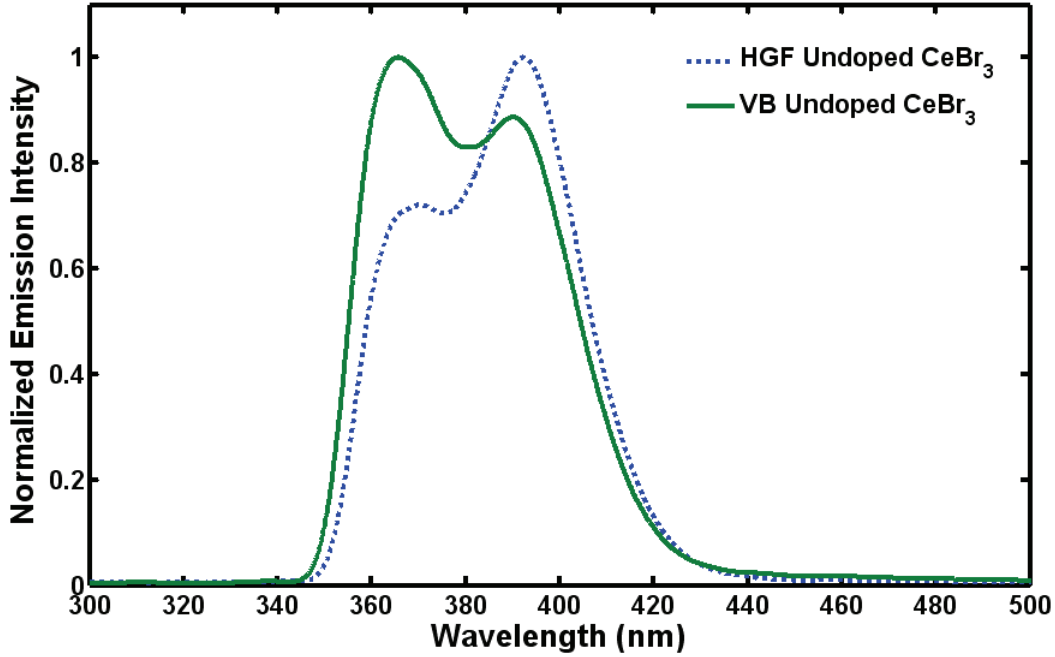


Figure 5.15. Collected radioluminescence emission spectra for undoped CeBr_3 grown by the horizontal gradient freeze (HGF) method and by the vertical Bridgman (VB) method.

5.2.2 Total Light Yield and γ -ray Spectroscopy

Integral quantum efficiencies calculated from the radioluminescence spectra in Figure 5.6 through Figure 5.15 for the doped and undoped CeBr_3 samples as well as equivalent radioluminescence data taken for BGO, NaI:Tl and $\text{LaBr}_3:\text{Ce}$ coupled to the Photonis XP5301B PMT are given for each dopant in Table 5.2.

Table 5.2. Estimated integral quantum efficiencies (IQE) for the materials

Material	IQE
BGO	20.80%
NaI:Tl	38.76%
$\text{LaBr}_3:\text{Ce}$	38.77%
Undoped CeBr_3	39.75%
Ca^{2+} -doped CeBr_3	40.68%
Sr^{2+} -doped CeBr_3	40.77%
Ba^{2+} -doped CeBr_3	40.13%
Zr^{4+} -doped CeBr_3	40.37%
Hf^{4+} -doped CeBr_3	40.14%
Zn^{2+} -doped CeBr_3	40.17%
Cd^{2+} -doped CeBr_3	40.59%
Pb^{2+} -doped CeBr_3	37.19%

DETECT2000 produced rough estimates of the light collection efficiency. The dimensions of the samples used to estimate total light yields as well as those estimated light collection efficiencies are provided in Table 5.3. The largest faces of each sample were optically coupled to the PMT window during the measurements. Finally, the estimated total light yields of each sample are provided in Table 5.4 along with their energy resolution (FWHM) at 662keV. Figure 5.16 is an example of γ -ray spectra collected for estimating total light yield.

Table 5.3. Dimensions of total light yield samples and their corresponding estimated light collection efficiencies.

Sample	Dimensions (mm)			LCE (%)
	x	y	z	
BGO 1	10.4	10.1	3.9	82.3%
BGO 2	10.7	10.4	4.1	82.3%
NaI:Tl SS1	10.9	10.6	4.5	82.9%
NaI:Tl SS2	10.3	10.2	4.0	83.5%
TG9 SS2	10.6	10.1	3.8	83.5%
TG9 SS5	10.8	7.6	2.9	84.6%
TG9 SS6	11.0	7.7	1.7	87.3%
UN1 SS1	8.2	3.8	1.0	85.3%
HB6 SS1	5.4	4.0	3.2	81.0%
HB42 SS1	5.2	5.0	4.3	79.4%
HB42 SS4	9.4	6.5	5.0	80.7%
HB7 SS3	8.2	4.9	2.2	84.7%
HB7 SS5	8.3	5.0	2.7	83.6%
BHB1 SS9	7.5	7.4	3.3	83.1%
BHB1 SS10	9.8	6.3	3.9	82.4%
HB27 SS2	5.6	3.7	3.2	80.8%
HB27 SS4	6.8	5.3	3.0	82.9%
HB27 SS5	4.7	4.1	3.1	80.9%
HB21 SS1	10.8	6.5	2.9	84.4%
HB21 SS3	5.7	6.1	2.8	83.0%
HB21 SS5	10.6	7.0	3.2	83.8%
HB36 SS1	6.1	6.1	3.9	81.2%
HB36 SS2	5.8	5.5	4.4	80.1%
HB36 SS3	6.5	3.9	3.5	80.7%
HB15 SS3	7.0	6.0	2.1	85.2%
HB23 SS2	8.0	6.0	5.9	78.7%
HB23 SS3	9.2	4.7	3.0	83.2%
HB17 SS4	6.5	6.3	2.6	83.8%
HB17 SS10	9.7	8.0	2.9	84.6%
HB24 SS2	5.2	5.1	4.0	80.2%
HB18 SS1	10.7	12.7	3.6	83.9%
HB18 SS2	11.9	10.7	2.8	85.4%

Table 5.4. Estimated total light yields and energy resolution (FWHM) of each sample.

Sample	Material	FWHM	LCE	IQE	Total LY	Max LY
		(%)	(%)	(%)	(ph/MeV)	(ph/MeV)
BGO 1	BGO	9.0%	82.3%	20.80%	6,850*	6,850*
BGO 2		9.4%	82.3%	20.80%	6,850*	
NaI:Tl SS1	NaI:Tl	6.5%	82.9%	38.76%	49,600	50,000
NaI:Tl SS2		6.4%	83.5%	38.76%	50,000	
TG9 SS2	LaBr ₃ :Ce	5.0%	83.5%	38.77%	57,100	59,600
TG9 SS5		4.5%	84.6%	38.77%	63,300	
TG9 SS6		3.1%	87.3%	38.77%	64,300	
UN1 SS1	Undoped CeBr ₃	15.2%	85.3%	39.75%	37,600	37,600
HB6 SS1		10.4%	81.0%	39.75%	26,200	
HB42 SS1	Ca-doped CeBr ₃	11.4%	79.4%	40.68%	23,600	28,100
HB42 SS4		20.3%	80.7%	40.68%	21,600	
HB7 SS3	Sr-doped CeBr ₃	8.3%	84.7%	40.77%	37,800	45,600
HB7 SS5		5.5%	83.6%	40.77%	43,600	
BHB1 SS9		4.6%	83.1%	40.77%	44,800	
BHB1 SS10		5.1%	82.4%	40.77%	44,400	
HB27 SS2	Ba-doped CeBr ₃	7.9%	80.8%	40.13%	31,300	31,300
HB27 SS4		9.8%	82.9%	40.13%	25,600	
HB27 SS5		16.5%	80.9%	40.13%	29,000	
HB21 SS1	Zr-doped CeBr ₃	6.8%	84.4%	40.37%	45,500	46,100
HB21 SS3		5.6%	83.0%	40.37%	46,100	
HB21 SS5		6.4%	83.8%	40.37%	45,400	
HB36 SS1	Hf-doped CeBr ₃	4.5%	81.2%	40.14%	49,000	49,000
HB36 SS2		4.8%	80.1%	40.14%	48,200	
HB36 SS3		4.4%	80.7%	40.14%	46,500	
HB15 SS3	Zn-doped CeBr ₃	4.6%	85.2%	40.17%	45,900	49,500
HB23 SS2		6.5%	78.7%	40.17%	42,200	
HB23 SS3		4.6%	83.2%	40.17%	49,500	
HB17 SS4	Cd-doped CeBr ₃	6.2%	83.8%	40.59%	32,500	39,100
HB17 SS10		7.1%	84.6%	40.59%	39,100	
HB24 SS2		4.7%	80.2%	40.59%	51,200	
HB18 SS1	Pb-doped CeBr ₃	9.0%	83.9%	37.19%	23,400	26,700
HB18 SS2		10.1%	85.4%	37.19%	26,700	

* BGO absolute light yield value assumed to be equal to that measured by Moszynski, et. al. [72] for a similarly sized sample.

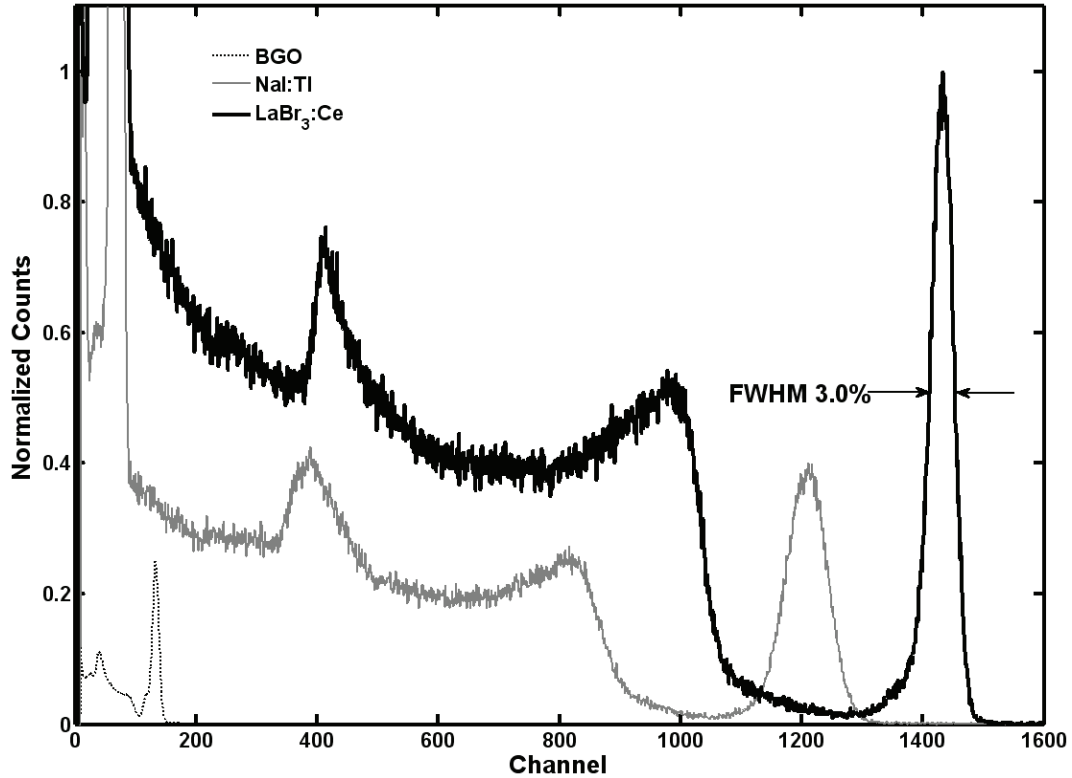


Figure 5.16. Example γ -ray spectra collected for estimating total light yield of unknown samples by comparing to the known BGO sample.

5.2.3 Light Yield Nonproportionality

The samples exhibiting the best energy resolution in Section 5.2.2 for each dopant were also tested for light yield nonproportionality. Fig. 5.12 is a plot of the relative light yield curves for NaI:Tl, LaBr₃:Ce and undoped CeBr₃ which were compared to literature results to ensure the RLY system was accurate. Figure 5.17 through Figure 5.21 plot the resulting relative light yield plots for the CeBr₃-based samples which resulted for each group of dopants. The solid lines in Figure 5.17 through Figure 5.21 are not theoretical lines of best fit, but are provided to simply better illustrate the trends in the data sets only. Despite a small offset in the RLY curves between the undoped case and the various doped cases, all CeBr₃ curves display the same trends indicating little or no change in the response dynamics.

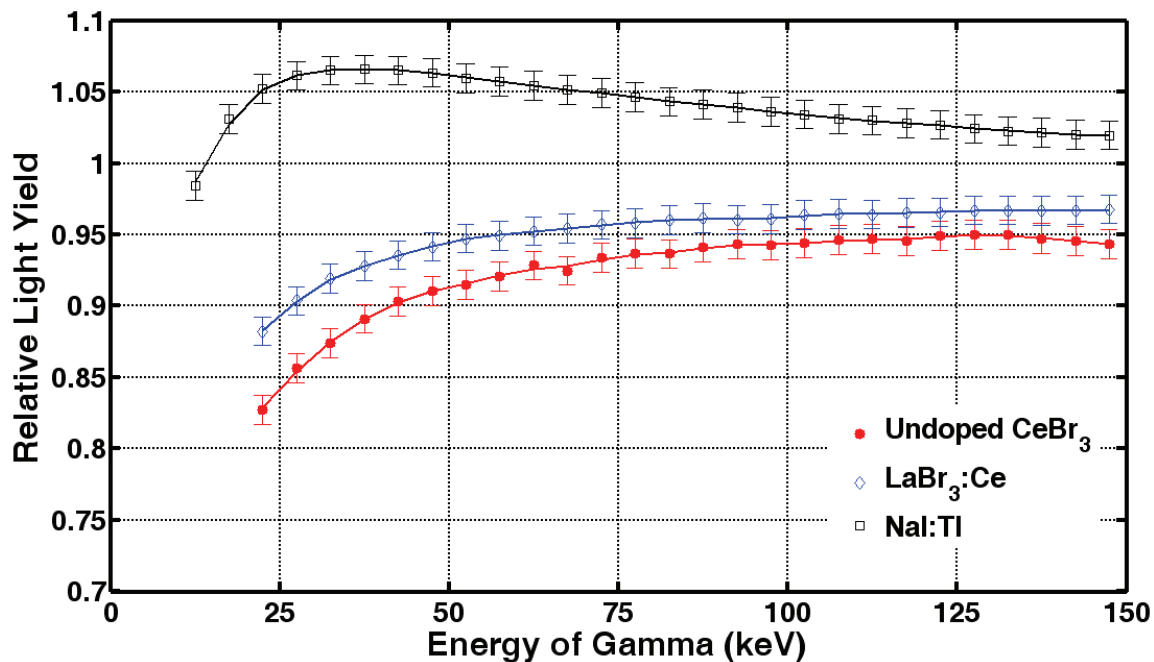


Figure 5.17. Relative light yield curves for NaI:Tl, LaBr₃:Ce and undoped CeBr₃.

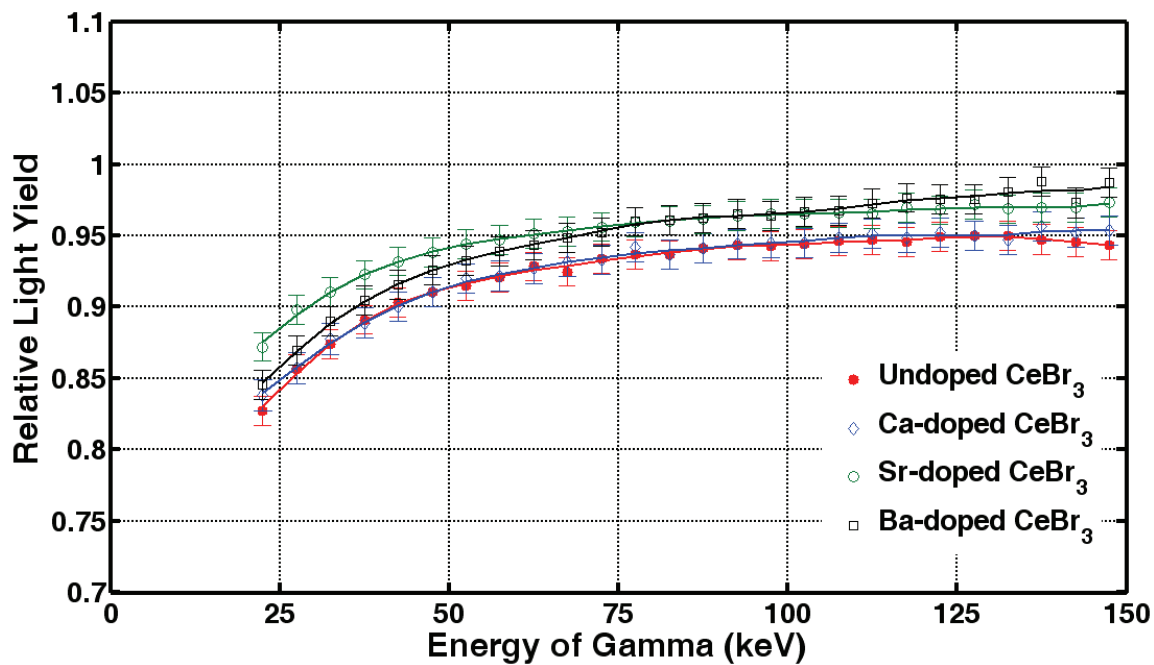


Figure 5.18. Relative light yield curves for undoped CeBr₃ and CeBr₃ doped with Group IIA cations.

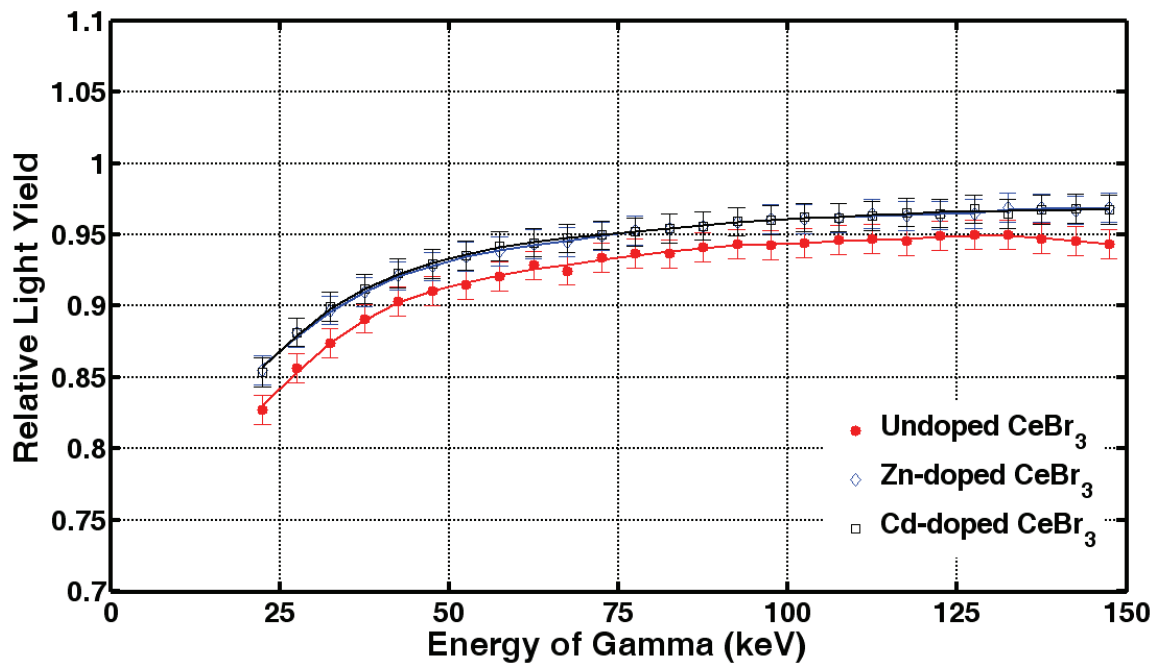


Figure 5.19. Relative light yield curves for undoped CeBr₃ and CeBr₃ doped with Group IIB cations.

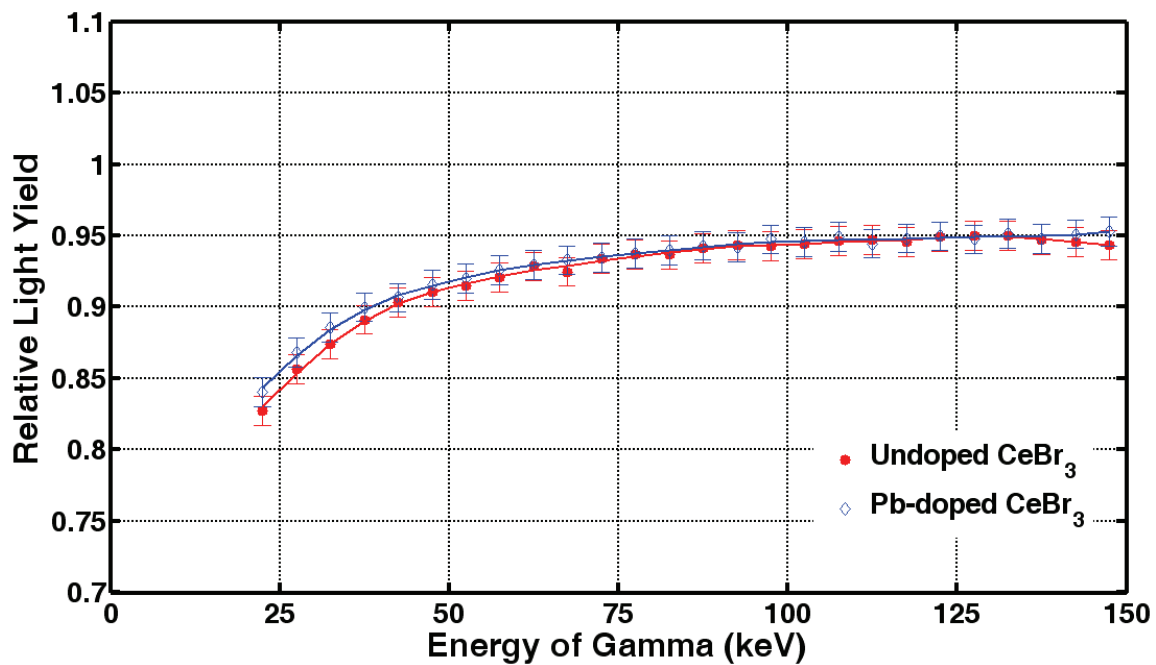


Figure 5.20. Relative light yield curves for undoped CeBr₃ and CeBr₃ doped with Group IVA cations.

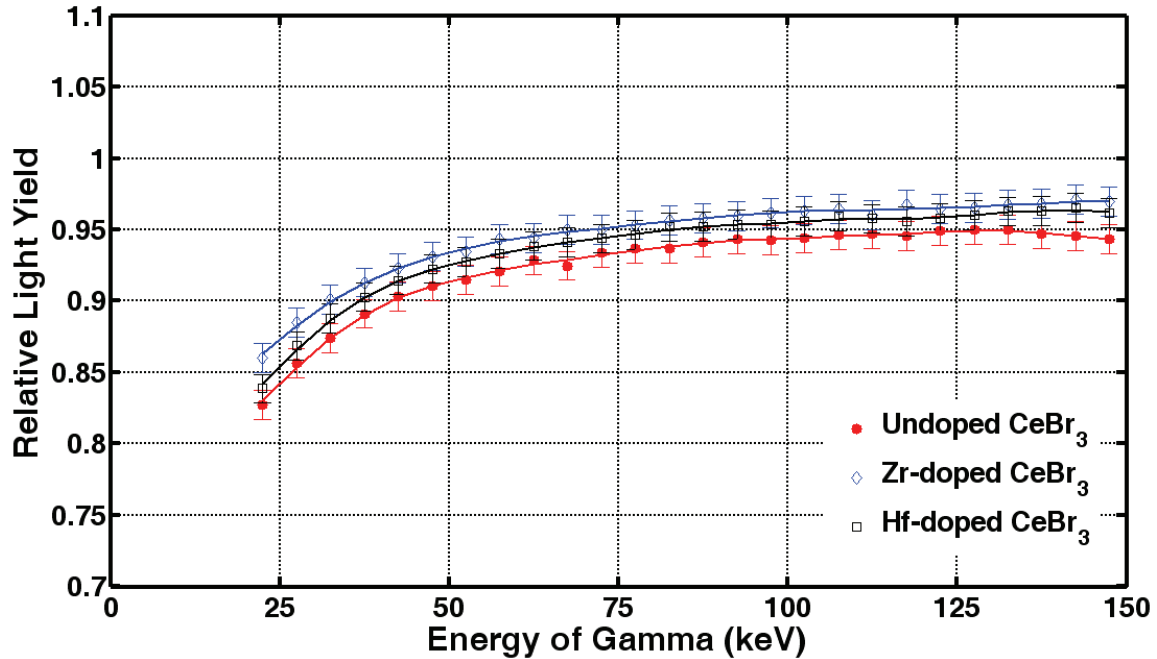


Figure 5.21. Relative light yield curves for undoped CeBr₃ and CeBr₃ doped with Group IVB cations.

5.2.4 Decay Constants

Single event pulses captured from an oscilloscope for the various dopants were plotted against the undoped CeBr₃ case in Figure 5.22 through Figure 5.25. While the time response of the PMT utilized to amplify the observed signals did contribute to the overall responses shown, the 2ns response time of the PMT was small compared to the kinetics of light intensity decay ($\tau \approx 30ns$).

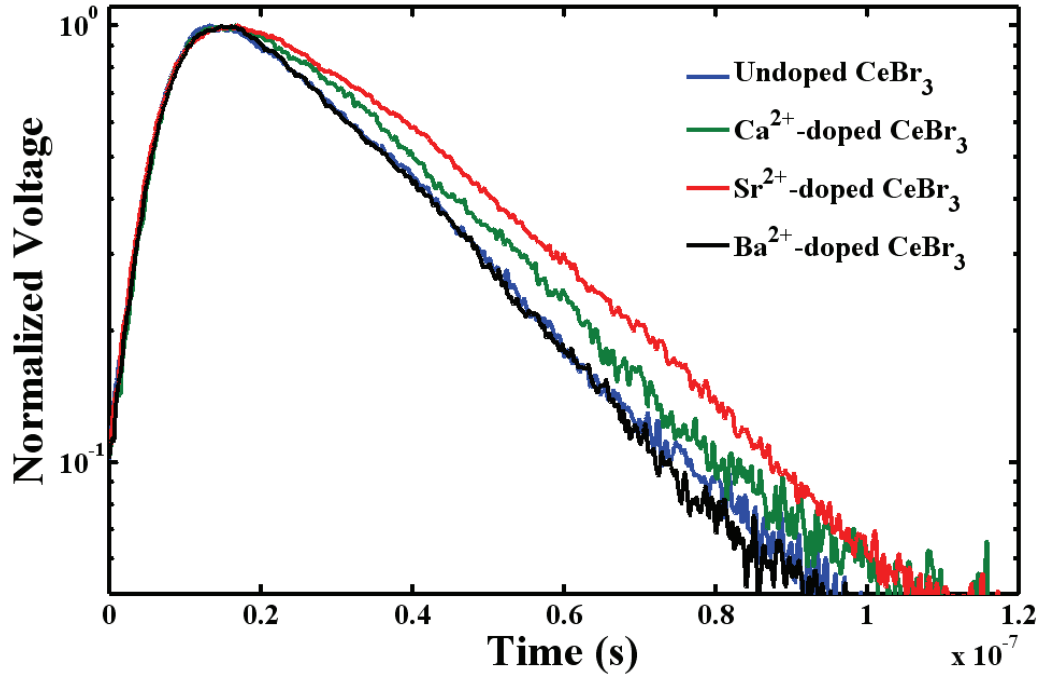


Figure 5.22. Voltage pulses as collected at the Photonis XP5301B PMT output for the various Group IIA samples under ^{137}Cs irradiation.

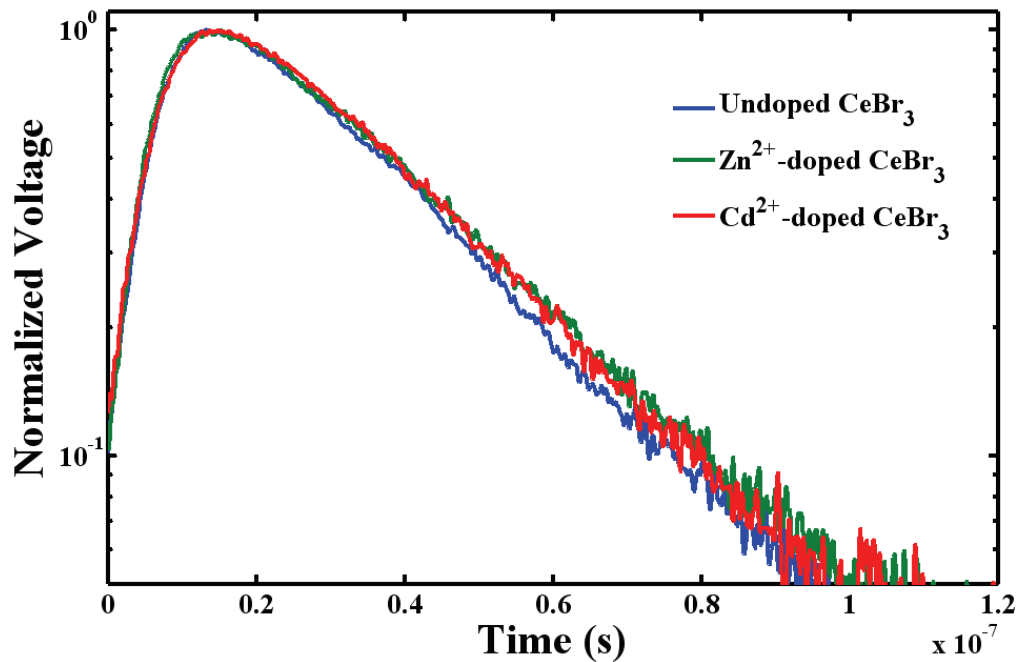


Figure 5.23. Voltage pulses as collected at the Photonis XP5301B PMT output for the various Group IIB samples under ^{137}Cs irradiation.

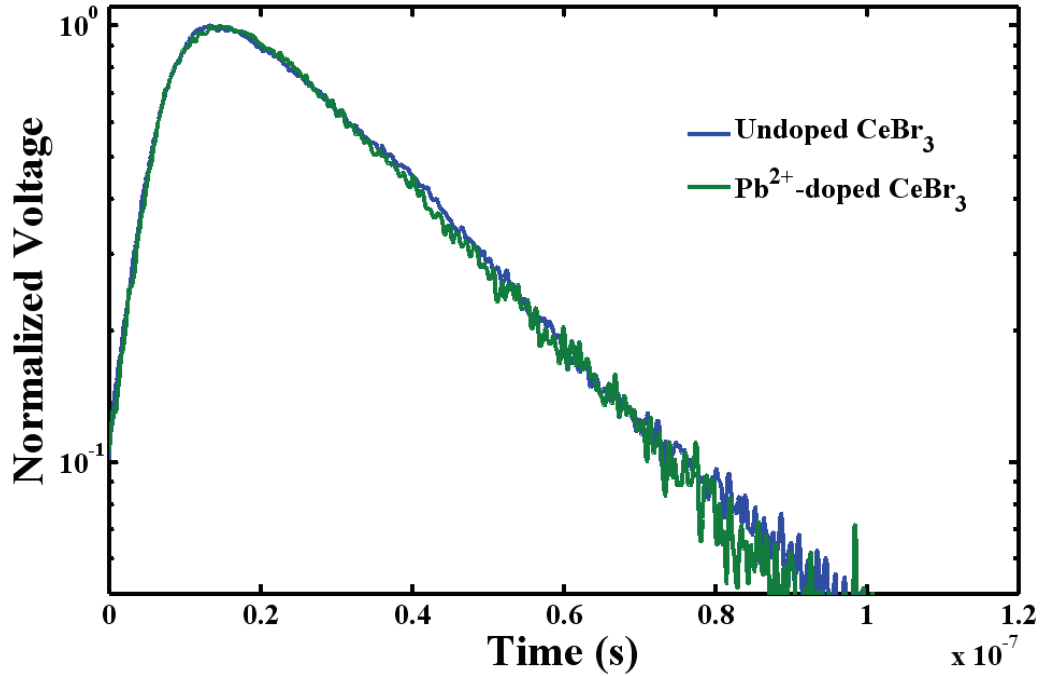


Figure 5.24. Voltage pulses as collected at the Photonis XP5301B PMT output for the various Group IVA samples under ^{137}Cs irradiation.

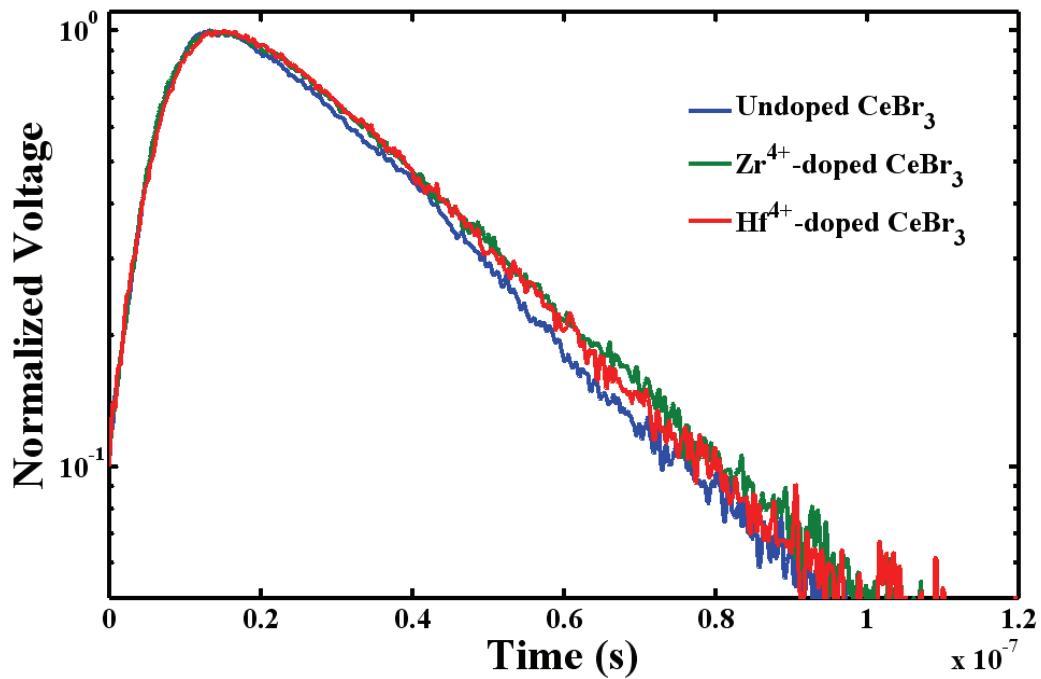


Figure 5.25. Voltage pulses as collected at the Photonis XP5301B PMT output for the various Group IVB samples under ^{137}Cs irradiation.

6 Conclusions and Discussion

Several important conclusions can be drawn from the experimental work and theory described in preceding chapters. In the following sections, the results from each area are discussed and conclusions are drawn.

6.1 Crystal Growth

Based on the size of the single crystals in each ingot, aliovalently-doping CeBr_3 dramatically improved ingot yields as compared to the undoped case. The horizontal gradient freeze method utilized for growing single crystals was non-ideal; growth rates were either non-constant or thermal gradients were low. These undesirable features of the method resulted in poor growth conditions which were insufficient for growing large single crystals of undoped CeBr_3 , since no undoped ingot yield large ($>1\text{cm}^3$) single crystals. On the other hand, large single crystals were readily achieved when the CeBr_3 charges were doped, indicating an improvement in ease of growth or, rather, a relaxation of the tolerances on growth conditions which produce large single crystals.

6.1.1 Ampoule Preparation

The first methods used to store raw CeBr_3 powder and prepare ampoules for crystal growth proved to be poor. H_2O contamination of feedstock CeBr_3 was a primary cause of Br_2 contaminating as-grown ingots, finally prevented by storing the raw CeBr_3 powder in sealed quartz vessels up to the moment of loading. Initially, the raw CeBr_3 powder was stored in “air-tight” high density polyethylene (HDPE) bottles inside the UDA glove box. Despite the UDA glove box atmosphere being maintained at $<10\text{ppm}$ H_2O , the raw CeBr_3 stored in the HDPE bottles became contaminated over time with H_2O .

Removing the H_2O contamination proved difficult too. Unexpectedly, baking ampoules under vacuum did not remove the water as had been suggested in previous studies [46]. However, vacuum distilling the contaminated raw CeBr_3 powder prior to sealing did remove the

contaminants and prevent the formation of Br_2 liquid over the ingot, at least below visual detection limits.

6.1.2 Growth Processes

The growth process proved inadequate for achieving large, single, unstrained crystals of CeBr_3 , doped or undoped. Large single crystals of undoped CeBr_3 simply did not withstand the growth induced strain and were reduced to small shards. Large single crystals of aliovalently-doped CeBr_3 , however, did not fracture under the growth induced strain, yet clearly showed signs of being stressed. Internally arrested cracks were often visible in doped CeBr_3 samples. Figure 6.1 shows a sample of Hf-doped CeBr_3 under UV illumination which clearly shows the internal cracks and strains typical of doped CeBr_3 crystals.



Figure 6.1. Photograph showing the strain in the single crystals of doped CeBr_3 .

Based on the size of the single crystals in each ingot, it can be concluded that aliovalently-doping CeBr_3 dramatically improved ingot yields. The horizontal gradient freeze method utilized for growing single crystals was non-ideal in that growth rates were either non-constant, thermal gradients were low at the freeze interface or stress induced in the just-grown section were too high. These undesirable features of the method resulted in poor growth conditions which were insufficient for growing large single crystals of undoped CeBr_3 . Yet, large single crystals were readily achieved when the CeBr_3 charges were doped, indicating an improvement in ease of growth.

Indeed, measured temperature profiles indicate that the thermal environment placed on the ampoule during growth was non-ideal. The single step recipe, as plotted on the left in Figure 6.2, did provide a higher thermal gradient at the growth interface, but thermal gradients in the

solidified section of the ingot were also high. Large thermal gradients in the solidified area created unacceptably high thermal stress.

The four step recipe, plotted to the right in Figure 6.2, provided a more consistent growth rate, but a lower thermal gradient at the freeze interface, possibly creating unstable growth conditions. Nevertheless, thermal gradients in the solidified portion of the ampoule were slightly improved as compared to the single step recipe. This feature of the four step recipe may be the root reason ingot yields were noted to be slightly improved over the single step recipe.

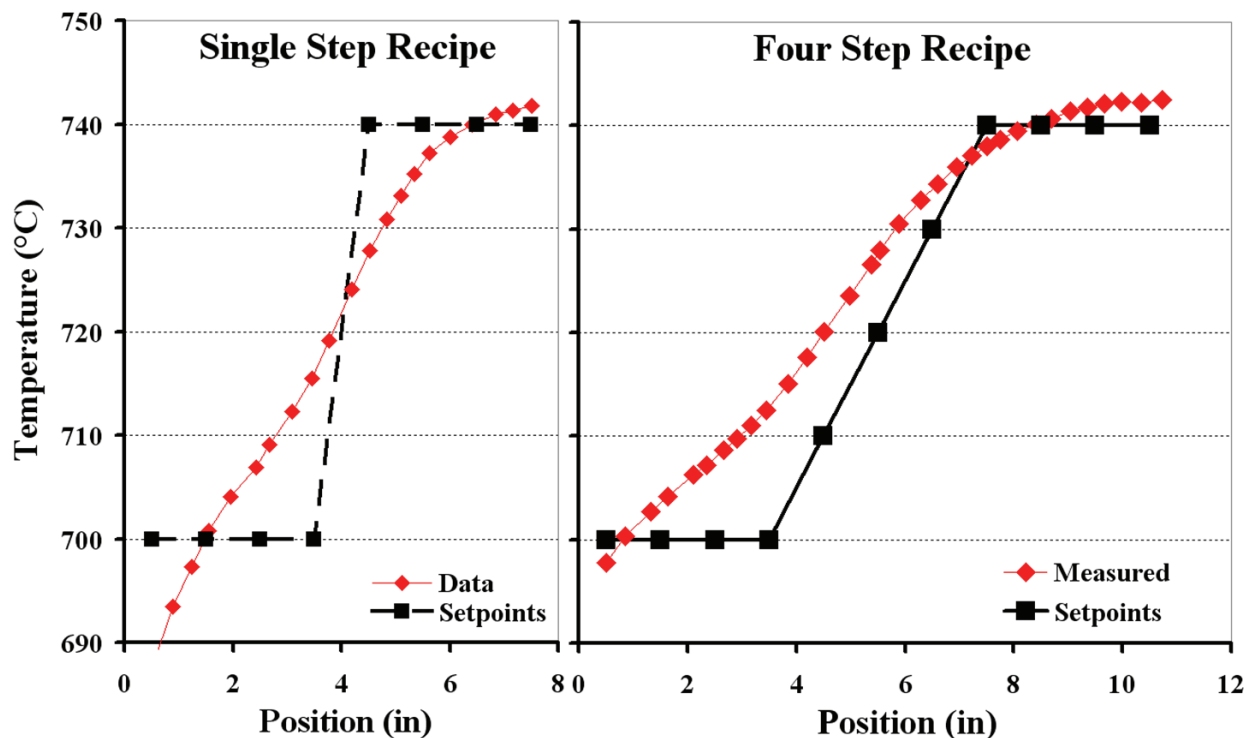


Figure 6.2. Measured temperature profiles of the EDG furnaces executing both the single step recipe and the four step recipe.

6.1.3 Sample Preparation and Preservation

The development of the processes required for properly preparing and preserving single crystal samples was iterative. Several steps were found necessary to producing high quality samples. Primary to preservation was the storage of samples under mineral oil. Mineral oil provided an excellent barrier against moisture and oxygen. Samples immersed in mineral oil were routinely left under normal atmosphere for many days with no visible surface degradation. In fact, samples wetted with just a thin film of mineral oil were often handled under normal

atmosphere without degradation. Mineral oil also proved to be an excellent lubricant for lapping samples.

6.2 Characterization

Characterization of the prepared samples revealed much information regarding the effects of the dopants. In general, however, only Pb-doping exhibited strong effects on the scintillation characteristics of CeBr₃. Under UV light, all other doped CeBr₃ samples produced a visibly blue fluorescence, while Pb-doped CeBr₃ emitted a pink fluorescence. These effects of Pb-doping were nonetheless expected. The following sections detail the observed effects of the dopants on each characteristic of scintillation.

6.2.1 Radioluminescence Spectra

A peak fitting MATLAB routine [81] was used to fit each of the radioluminescence curves in Figure 5.6 through Figure 5.15. An example fit for the Ba-doped CeBr₃ case is shown in Figure 6.3. Each peak presumably corresponds to the split 4f energy states $^2F_{5/2}$ and $^2F_{7/2}$. The higher energy emission peak mean, lower energy emission peak mean, their FWHM values and their ratios were recorded for each radioluminescence sample tested. Table 6.1 provides those values. Figure 6.4 plots the peak locations as determined by the fitting routine, while Figure 6.5 plots the area fractions of each peak. The area fractions are simply the fraction of the total emission spectrum which is attributed to each Gaussian peak and are indicators of the relative frequency of radiative decay occurring to each of the split 5d energy states.

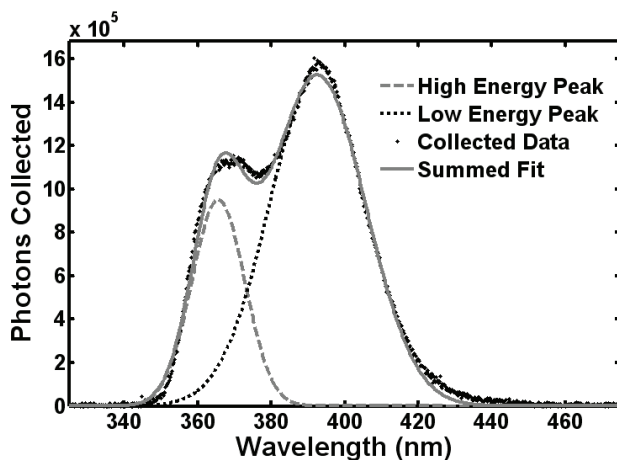


Figure 6.3. Two Gaussian peaks fit to the Ba-doped CeBr₃ radioluminescence data set.

Table 6.1. Radioluminescence data analysis.

Material	Dopant	Sample	High Energy Peak			Low Energy Peak		
			Position	FWHM	Area Fraction	Position	FWHM	Area Fraction
			(nm)	(nm)		(nm)	(nm)	
LaBr ₃	Ce	TG9 SS1	356.5	17.3	0.30	378.2	37.5	0.70
		TG9 SS3	356.3	18.5	0.27	379.5	38.2	0.73
		TG9 SS6	355.1	18.8	0.37	377.7	38.0	0.63
CeBr ₃	none	HB6 SS1	365.1	16.8	0.24	391.6	31.8	0.76
		UN1 SS1	364.0	17.6	0.34	388.8	32.9	0.66
CeBr ₃	Ca	HB19 SS1	374.2	22.9	0.41	394.5	39.0	0.59
		HB19 SS2	372.9	24.1	0.42	393.9	39.2	0.58
CeBr ₃	Sr	BHB1 SS1	375.5	21.3	0.40	395.8	38.9	0.60
		BHB1 SS10	376.1	20.3	0.40	396.3	38.4	0.60
CeBr ₃	Ba	HB27 SS2	365.6	17.0	0.25	392.6	31.0	0.75
CeBr ₃	Zr	HB8 SS3	368.2	20.2	0.26	388.5	38.1	0.74
		HB21 SS2	366.6	17.3	0.25	387.4	35.8	0.75
		HB21 SS4	365.0	17.4	0.27	387.6	36.1	0.73
CeBr ₃	Hf	HB22 SS2	369.8	20.2	0.34	389.2	37.4	0.66
		HB36 SS3	365.5	16.5	0.32	386.4	35.2	0.68
CeBr ₃	Zn	HB15 SS5	366.1	17.3	0.32	386.6	36.1	0.68
		HB23 SS2	366.0	18.1	0.32	386.8	37.1	0.68
		HB23 SS3	365.1	16.7	0.31	387.2	35.4	0.69
CeBr ₃	Cd	HB17 SS3	367.5	19.3	0.28	387.9	37.7	0.72
		HB24 SS3	365.6	16.4	0.28	387.8	34.9	0.72
CeBr ₃	Pb	HB18 SS1	368.1	17.8	0.22	390.2	34.3	0.78

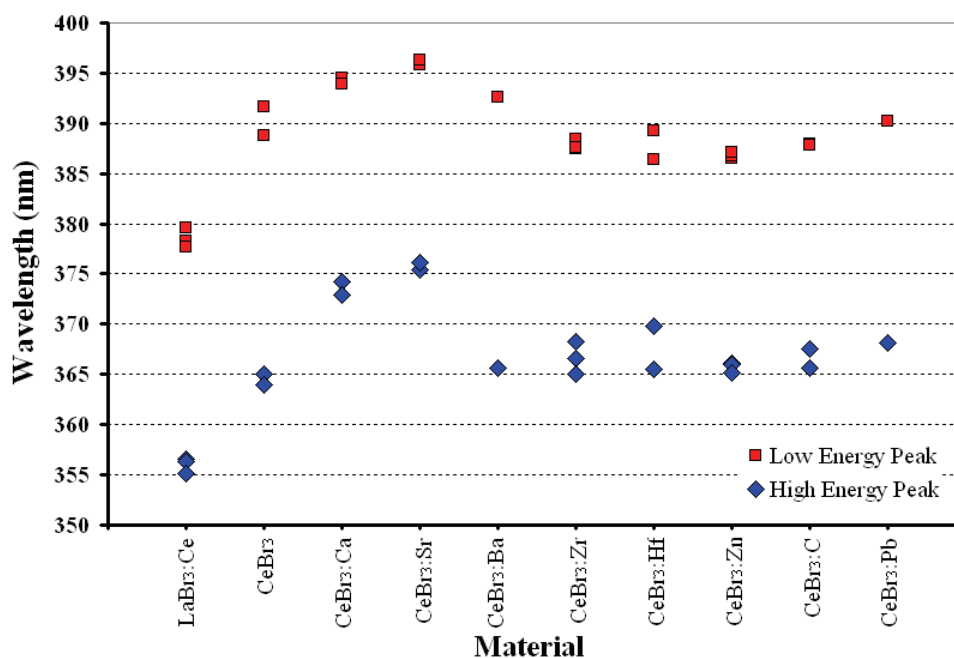


Figure 6.4. Radioluminescence emission peak locations.

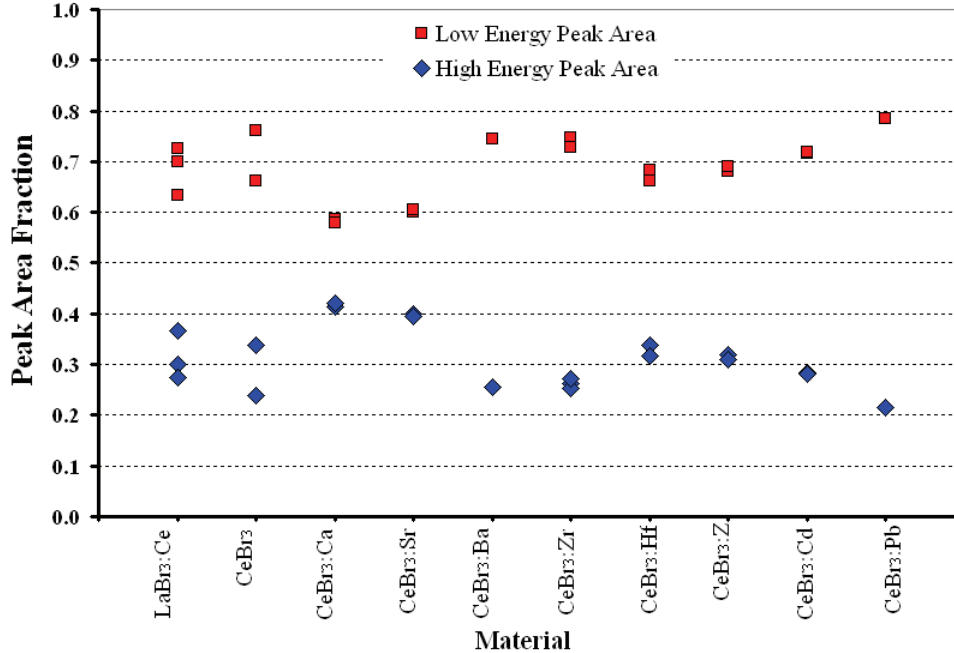


Figure 6.5. Radioluminescence emission peak area fractions.

The plots in Figure 6.4 through Figure 6.5 illustrate several interesting effects of aliovalent doping. Ca- and Sr-doping clearly causes the emission spectrum to red shift, possibly indicating an increase in self-absorption. Ba-doping, on the other hand, does not appear to affect the peak locations of the radioluminescence spectrum of CeBr₃. The remaining dopants, Zr, Hf, Zn, Cd, and Pb, all exhibited slightly blue-shifted low energy peak locations and slightly red-shifted high energy peak locations. The undoped CeBr₃ emission peaks were on average 25.7nm apart while the Zr-, Hf-, Zn-, Cd-, and Pb-doped CeBr₃ emission peaks were only 20 – 22nm apart.

Ca- and Sr-doping also appeared to cause the relative intensities of emission of the two peaks to shift more towards the high energy peak. Pb-doping increased the relative intensity of the low energy peak decay mode though. The remaining dopants did not appear to have any significant effect on the decay mode of CeBr₃.

6.2.2 Total Light Yield and γ -ray Spectroscopy

Hf- and Zn-doped CeBr₃ were measured to produce the highest light yield of the aliovalently-doped samples. Ca- and Pb-doping, alternatively, appeared to quench light production severely in CeBr₃ as compared to the highest light yield samples. Pb is a known

scintillation quencher as it exhibits stable valences of Pb^{2+} and Pb^{4+} , which interfere with the Ce radiative decay mechanism, and was expected to behave in this manner. However, Ca was not expected to quench light output. Ba-doping also appeared to quench scintillation, but not to the degree observed in Pb- or Ca-doping. Sr-, Zr-, and Cd-doping only mildly quenched scintillation. These conclusions, however, are drawn from comparison with Hf- and Zn-doped samples, not against undoped samples.

The undoped samples produced in this work failed to produce light yields equivalent to published values, therefore it seems the undoped samples were substandard quality. Only Ca-, Ba- and Pb-doped samples were measured to have light yields lower than the undoped samples. All other dopants appeared to have improved light yields as compared to the undoped samples, substantially in some cases. If it is assumed that the HGF method utilized in this work produced poor quality material, then it seems that doping with SrBr_2 , ZrBr_4 , HfBr_4 , ZnBr_2 and CdBr_2 not only improved ingot yields, but also single crystal quality and scintillation performance.

6.2.3 Relative Light Yield Proportionality

The relative light yield data in Figure 5.18 through Figure 5.21 indicate that no tested dopants had any significant effect on light yield proportionality of CeBr_3 . This data contradicts previously reported results [76] in which impurities were thought to be a root cause of nonproportionality in scintillators. The impurity concentrations in this work were far greater than those utilized in [76], thus may be beyond some saturation phenomenon yet to be understood. While not deleterious to the goals of this work, the data in Figure 5.18 through Figure 5.21 indicate that control of nonproportionality can not be achieved by addition of impurities.

6.2.4 Decay Constants

Based on the collected scintillation pulses, no significant change to the decay mode of CeBr_3 was observed for any dopants. Only Ca^{2+} and Sr^{2+} doping exhibited any noticeable deviation from the undoped CeBr_3 case in the scintillation decay. However the decay slopes of both curves in the range of 0.4×10^{-7} s to 1.0×10^{-7} s were nearly identical to the undoped CeBr_3 case. The deviation, instead, results from a delay in the decay or rather a broadening of the peak intensity. The undoped CeBr_3 pulse exhibited peak intensity near 0.17×10^{-7} s which then rapidly transitioned to a single mode exponential decay curve by 0.2×10^{-7} s. Sr^{2+} and, to a lesser extent, Ca^{2+} -doped samples both slowly transitioned from their peaks at 0.17×10^{-7} s to single mode

exponential decay by approximately 0.4×10^{-7} s and 0.3×10^{-7} s respectively, resulting in their decay curves being shifted slightly. While an added slow rise time component to the scintillation kinetics may potentially explain the shift in decay, the shifts are more likely a product of electronic noise contributions. Regardless, the impact of these minor effects is relatively negligible on the timing performance of CeBr₃.

6.3 Summary

While it was previously stated that all dopants improved ingot yield, Ca²⁺ improved the single crystal yield the least of all tested dopants. Sr-, Ba-, Zr-, and Zn-doping all moderately improved ingot yields, while Hf- and Cd-doping increased ingot yields quite substantially. Pb²⁺, perhaps, improved ingot yield the most.

The Group IIA dopants, Ca²⁺, Sr²⁺, and Ba²⁺, did seem to alter the scintillation characteristics of CeBr₃. Ca²⁺ and Sr²⁺ both strongly altered the emission wavelengths of the radioluminescence spectrum of CeBr₃. Likewise, Ca²⁺ and Sr²⁺ also seem to have slightly slowed the decay of CeBr₃. Strangely, Ba²⁺ did not affect the emission spectrum or the decay characteristics of CeBr₃ at all though. As previously noted, none of the Group IIA dopants altered the light yield proportionality curve. Ca²⁺ and Ba²⁺ caused the measured absolute light yield to drop significantly, while Sr²⁺ only mildly quenched light output.

The Group IIB dopants, Zn²⁺ and Cd²⁺, were less deleterious to the scintillation performance of CeBr₃ than were the Group IIA dopants. Both Zn²⁺ and Cd²⁺ slightly blue-shifted the low energy radioluminescence emission peak, but did not appreciably alter the relative emission intensity ratio between the two peaks as compared to undoped CeBr₃. Neither dopant exhibited any effects on decay characteristics, nor on the light yield nonproportionality of CeBr₃. Zn-doped CeBr₃ exhibited the highest light yield of any doped sample. Cd²⁺ moderately quenched light output.

The sole Group IVA dopant, Pb²⁺, strongly altered the scintillation characteristics of CeBr₃. Absolute light yield was strongly quenched by the addition of Pb. While the decay constant and light proportionality of CeBr₃ did not appear to change when Pb²⁺ was added, the radioluminescence spectrum of Pb-doped CeBr₃ showed added light emission occurring at the red end of the spectrum.

Finally, the Group IVB dopants, Zr^{4+} and Hf^{4+} , only slightly affected the scintillation characteristics of $CeBr_3$. The radioluminescence spectra of both show minor red-shifting of the high energy peak and blue-shifting of the low energy peak. While the two dopants exhibited different relative emission intensities of each peak, both fell within the range measured in the undoped $CeBr_3$ samples. Hf-doped $CeBr_3$ was measured to have a very high light yield, while Zr-doped $CeBr_3$ showed only moderately lower light yields. Neither dopant appeared to alter the decay characteristics of $CeBr_3$, nor did they change the light proportionality characteristics.

Overall, based on the growth and scintillation characteristics, Zn^{2+} and Hf^{4+} dopants appear to be ideal candidates for further study. They exhibited the highest observed light yields with little to no effect on scintillation kinetics, radioluminescence emission spectra, and light yield proportionality. In addition, both dopants appeared to improve ingot yields significantly over the undoped case.

Note that the concepts introduced here to strengthen typically brittle scintillation materials is likely applicable to other materials, such as $LaBr_3:Ce$ or $NaI:Tl$. While $NaI:Tl$ is already quite rugged as compared to the lanthanide halide scintillator family, an increase in strength and improvement in ease of growth only further help to increase availability and decrease production costs. Newer scintillators, such as the lanthanide halides have thus far been available on the commercial market in limited quantities and carry a high expense. Increasing their strength via aliovalent doping may in fact bring these new technologies to the commercial market.

References

- [1] R. Hofstadter, "Alkali Halide Scintillation Counters," *Phys. Rev.*, vol. 74 (1948) pp. 100.
- [2] D. C. Northrop and O. Simpson, "Semiconductor Counters. I. Theory," *Proc. Phys. Soc.*, vol. 80 (1962) pp. 262-275.
- [3] P. E. Gibbons and D. C. Northrop, "Semiconductor Counters. II. Experiment," *Proc. Phys. Soc.*, vol. 80 (1962) pp. 276-285.
- [4] eV Products Website, <http://www.evproducts.com/>, June, 2008.
- [5] F. Wilkinson, "Alpha Spectra, Inc." June, 2008. Personal communication.
- [6] G. F. Knoll, *Radiation Detection and Measurement*, 3rd ed., Wiley: London, 2000.
- [7] P. Rodnyi, *Physical Processes in Inorganic Scintillators*. CRC Press: New York, 1997.
- [8] M. J. Weber and R. R. Monchamp, "Luminescence of Bi₄Ge₄O₁₂: Spectral and Decay Properties," *J. Appl. Phys.*, vol. 44 (1973) pp. 5495.
- [9] C. H. Boissevain and W. F. Drea, "Luminescence Excited by X-Rays in Colloidal Alkaline Earth Salts," *Phys. Rev.*, vol. 31 (1928) pp. 851-857.
- [10] P. Dorenbos, C. W. E. Van Eijk, H.-U. Gudel, K. W. Kramer, and E. V. D. Van Loef, "Scintillator crystals, method for making same, use thereof," U.S. Patent 7,250,609, Apr. 28, 2006.
- [11] P. Dorenbos, C. W. E. Van Eijk, H.-U. Gudel, K. W. Kramer, and E. V. D. Van Loef, "Scintillator crystals, method for making same, use thereof," U.S. Patent 7,067,816, Feb. 16, 2001.
- [12] H. Becquerel, "Recherches sur les phénomènes de phosphorescence produits par le rayonnement du radium," *C. R. Hebd. Seances Acad. Sci.*, vol. 129 (1899) pp. 912.
- [13] W. C. Röntgen, "On a New Kind of Rays," *Sitzgber. Physik. -Med. Ges. Würzburg*, vol. 137, Dec. 1895.
- [14] W. Crookes, "The Emanations of Radium," *Proc. Phys. Soc.*, vol. 71 (1903) pp. 405.
- [15] E. Rutherford and H. Geiger, "α-particles from Radio-active Substances," *Proc. Roy. Soc.*, vol. A81 (1908) pp. 141-161.
- [16] E. Rutherford and H. Geiger, "Charge and Nature of α-particle," *Proc. Roy. Soc.*, vol. A81 (1908) pp. 162-173.
- [17] E. Regener, "Über Zählung der α-Teilchen durch die Szintillation und über die Größe des elektrischen Elementarquantums," *Verh. d. D. Phys. Ges.*, vol. 19 (1908) pp. 78.
- [18] E. Regener, "β-Ray Spinthariscopes," *Verh. d. D. Phys. Ges.*, vol. 19 (1908) pp. 351.
- [19] E. Regener, "Über Zählung der α-Teilchen durch die Szintillation und über die Größe des elektrischen Elementarquantums," *Sitzungsberichte der Preussischen Akademie der Wissenschaften zu Berlin*, vol. 38 (1909) pp. 948-965.

- [20] B. Karlik, "Relation between the Scintillations and the Structure of Zinc Sulphide. The Cause of the Scintillation Process," *Wien. Ber.*, vol. 136 (1927) pp. 531.
- [21] B. Karlik and E. Kara Michailova, "Luminescence Excited by α -Rays and Its Relation to the Energy of the α -Particles," *Wien. Ber.*, vol. 137 (1928) pp. 363.
- [22] B. Karlik and E. Kara Michailova, "Zur Kenntnis der Szintillationsmethode," *Zeit. f. Phys.*, vol. 48 (1928) pp. 765.
- [23] J. Chariton and C. A. Lea, "Some Experiments concerning the Counting of Scintillations Produced by Alpha Particles. Part I," *Proc. Roy. Soc.*, vol. A122 (1929) pp. 304.
- [24] E. Rutherford, J. Chadwick and C. D. Ellis, *Radiations from Radioactive Substances*. Macmillan: New York, 1930.
- [25] J. B. Birks, *The Theory and Practice of Scintillation Counting*. Pergamon Press: New York, 1964.
- [26] A. T. Krebs, "Ein Demonstrationsversuch zur Emanationsdiffusion," *Ann. Physik.*, vol. 39 (1941) pp. 330.
- [27] S. C. Curran and W. R. Baker, Nov. 1944, University of California, classified report.
- [28] S. C. Curran and W. R. Baker, "Photoelectric Alpha-Particle Detector," *Rev. Sci. Instr.*, vol. 19 (1948) pp. 116.
- [29] M. Blau and B. Dreyfus, "The Multiplier Photo-Tube in Radioactive Measurements," *Rev. Sci. Instr.*, vol. 16 (1945) pp. 245.
- [30] H. Kallman, *Natur Und Technik*, July, 1947.
- [31] E. Rutherford and E. N. C. da Andrade, "Wave-length of the Soft γ -rays from Radium," *Phil. Mag.*, vol. 27 (1914) pp. 854.
- [32] O.R. Frisch, "Isotope Analysis of Uranium Samples by Means of Their α -ray Groups," *Unpublished report, BR-49 British Atomic Energy Project*, (1944).
- [33] P. Villard, "Sur la réflexion et la réfraction des rayons cathodiques et des rayons déviés du radium," *Comptes rendus hebdomadaires des séances de l'Académie des sciences*, vol. 130 (1900) pp. 1010,1178.
- [34] A. Pais, *Inward Bound: Of Matter and Forces in the Physical World*. Clarendon Press: Oxford, 1986.
- [35] B. Busby, <http://www.hps.org/publicinformation/ate/q654.html>, June, 2008.
- [36] R. H. Gillette, "Calcium and Cadmium Tungstate as Scintillation Counter Crystals for Gamma-Ray Detection," *Rev. Sci. Instrum.*, vol. 21 (1950) pp. 294.
- [37] W. Van Sciver and R. Hofstadter, "Scintillations in Thallium-Activated CaI_2 and CsI ," *Phys. Rev.*, vol. 84 (1951) pp. 1062.
- [38] J. Bonanomi and J. Rossel, "Scintillations de luminescence dans des iodures d'alcalins," *Helv. Phys. Acta.*, vol. 25 (1952) pp. 725.
- [39] W. Van Sciver and R. Hofstadter, "Gamma- and Alpha-Produced Scintillation in Cesium Fluoride," *Phys. Rev.*, vol. 87 (1952) pp. 552.
- [40] J. Schenck, "Activation of Lithium Iodide by Europium," *Nature*, vol. 171 (1953) pp. 518.

- [41] P. Brinkman, "CsI(Na) Scintillation Crystals," *Phys. Lett.*, vol. 15 (1965) pp. 305.
- [42] J. Menefee, C. F. Swinehart and E. E. O'Dell, "Calcium Fluoride as an X-ray and Charged Particle Detector," *IEEE Trans. Nucl. Sci.*, vol. NS-13 (1966) pp. 720.
- [43] P. Dorenbos, J. T. M. de Haas, and C. W. E. van Eijk, "Gamma Ray Spectroscopy With a $\text{\O}19 \times 19 \text{ mm}^3$ $\text{LaBr}_3 : 0.5\% \text{ Ce}^{3+}$ Scintillator", *IEEE Trans. Nucl. Sci.*, vol. 51 (2004) pp. 1289-1296.
- [44] P. Lecoq, A. Annenkov, A. Gektin, M. Korzhik and C. Pedrini, *Inorganic Scintillators for Detector Systems*. Springer: Berlin, 2006.
- [45] K. S. Shah, J. Glodo, W. Higgins, E. V. D. van Loef, W. W. Moses, S. E. Derenzo and M. J. Weber, "CeBr₃ Scintillators for Gamma-Ray Spectroscopy," *IEEE Trans. Nucl. Sci.*, vol. 52 (2005) pp. 3157-3159.
- [46] F. P. Doty, D. S. McGregor, M. J. Harrison, K. Findley and R. Polichar, "Structure and properties of lanthanide halides," *Proceedings of SPIE--the International Society for Optical Engineering*, vol. 6707 (2007) pp. 670705.
- [47] Burle Industries, Inc., *Photomultiplier Handbook*, 1980.
- [48] J. T. M. de Haas and P. Dorenbos, "Advances in Yield Calibration of Scintillators," *IEEE Trans. Nucl. Sci.*, vol. 55 (2008) pp.1086-1092.
- [49] M. Moszynski, J. Zalipska, M. Balcerzyk, M. Kapusta, W. Mengesha, and J. D. Valentine, "Intrinsic Energy Resolution of NaI(Tl)," *Nucl. Instrum. Methods A*, vol. 484 (2002) pp. 259-269.
- [50] D. Brown, *Halides of the Transition Elements: Halides of the Lanthanides and Actinides*. Wiley: London, 1968.
- [51] T. H. Courtney, *Mechanical Behavior of Materials*, 2nd ed., McGraw-Hill, New York, 2000.
- [52] M. N. Sinha and P.S. Nicholson, "Effect of impurities on the strengthening of CaF₂ single crystals," *J. Mat. Sci.*, vol. 12 (1977) pp. 1451-1462.
- [53] T. Kataoka and T. Yamada, "Yield strength and dislocation mobility of KCl-KBr solid solution single crystals," *Jap. J. Appl. Phys.*, vol. 16 (1977) pp. 1119-1126.
- [54] G. Blasse, "Luminescence of inorganic solids: from isolated centres to concentrated systems," *Prog. Solid State Chem.*, vol.18 (1988) pp. 79-171.
- [55] B. Morosin, "Crystal Structures of Anhydrous Rare Earth Chlorides," *J. Chem. Phys.*, vol. 49 (1968) pp. 3007-3012.
- [56] C. Kittel, *Introduction to Solid State Physics*, 8th ed., New York: Wiley, 2005.
- [57] G. S. Rohrer, *Structure and Bonding in Crystalline Materials*, New York: Cambridge University Press, 2001.
- [58] Hilger Crystals NaCl technical data sheet, January 2009, Margate, England: Hilger Crystals, <http://www.hilger-crystals.co.uk/>.
- [59] M. Meier, *The Ionic Bond*, April 18, 2005, ENG-45L Class Notes, University of California, Davis, <http://www.matsci.ucdavis.edu/MatSciLT/ENG-45L/Files/Experiment-1.pdf>.

- [60] A. G. Evans and T. G. Landon, "Structural Ceramics", *Prog. Mat. Sci.*, vol. 21 (1976) pp. 171-441.
- [61] G. I. Taylor, "Plastic Deformation of Crystals," *Proc. Royal Soc. London*, vol. 145 (1934) pp. 362-404.
- [62] E. Orowan, "Plasticity of Crystals," *Zeit. Physik.*, vol. 89 (1934) pp. 605-659.
- [63] M. Polyani, "Lattice Distortion which Originates Plastic Flow," *Zeit. Physik*, vol. 89 (1934) pp. 660-662.
- [64] J. Frenkel, "Theory of the Elasticity Limits and Rigidity of Crystalline Bodies," *Zeit. Physik.*, vol. 37 (1926) pp. 572-609.
- [65] R. Peierls, "The Size of a Dislocation", *Proc. Phys. Soc.*, vol. 52 (1940) pp. 34-37.
- [66] F. R. N. Nabarro, "Dislocations in a Simple Cubic Lattice," *Proc. Phys. Soc.*, vol. 59 (1947) pp. 256-272.
- [67] A. Kelly and R. B. Nicholson, "Precipitation Hardening," *Prog. Mat. Sci.*, vol. 10 (1963) pp. 149-391.
- [68] S. Ra, S. Kim, H. J. Kim, H. Park, S. Lee, H. Kang, and S.-H. Doh, "Luminescence and Scintillation Properties of a CeBr₃ Single Crystal," *IEEE Trans. Nucl. Sci.*, vol. 55 (2008) pp.1221-1224.
- [69] W. Drozdowski, P. Dorenbos, A. J. J. Bos, G. Bizarri, A. Owens and F. G. A. Quarati, "CeBr₃ Scintillator Development for Possible Use in Space Missions," *IEEE Trans. Nucl. Sci.*, vol. 55 (2008) pp.1391-1396.
- [70] *Photomultiplier Tubes: Principles and Applications*, ed. S. O. Flyckt and C. Marmonier, Brive, France: Photonis, 2002.
- [71] Photonis photomultiplier XP5301 technical data sheet, October 2007, Brive, France: Photonis, <http://www.photonis.com/upload/industry/science/pdf/pmt/XP5301.pdf>.
- [72] M. Moszynski, M. Kapusta, M. Mayhugh, D. Wolski, and S. O. Flyckt, "Absolute Light Output of Scintillators," *IEEE Trans. Nucl. Sci.*, vol. 44 (1997) pp.1052-1061.
- [73] A. J. Wojtowicz, W. Drozdowski, M. Ptaszyk, Z. Galazka, and J. L. Lefaucher, "Scintillation Light Yield of Ce-Doped LuAP and LuYAP Pixel Crystals," SCINT 2005 Conference.
- [74] W. Drozdowski, A. J. Wojtowicz, T. Lukasiewicz, and J. Kisielewski, "Scintillation Properties of LuAP and LuYAP Crystals Activated with Cerium and Molybdenum," *Nucl. Instrum. Methods A*, vol. 562 (2006) pp. 254-261.

- [75] F. Cayotte, D. Laurendeau, and C. Moisan, "DETECT2000: An Improved Monte-Carlo Simulator of the Computer Aided Design of Photon Sensing Devices," in *Proc. of SPIE*, vol. 4833, 2002, pp.69-76.
- [76] M. Moszynski, W. Czarnacki, A. Syntfeld-Kazuch, A. Nassalski, T. Szczesniak, L. Swiderski, F. Kniest, and A. Iltis, "A Comparative Study of Undoped NaI Scintillators with Different Purity," in *IEEE Nucl. Sci. Symp.*, 2008, pp. N02-347.
- [77] Saint Gobain Crystals BrillanCe 380 technical data sheet, January 2009, Hiram, OH, USA: Saint Gobain Crystals, <http://www.detectors.saint-gobain.com>.
- [78] M. Gierlik, M. Moszynski, A. Nassalski, A. Syntfeld-Kazuch, T. Szczesniak, and L. Swiderski, "Investigation of Absolute Light Output Measurement Techniques", *IEEE Trans. Nucl. Sci.*, vol. 54 (2007) pp.1367-1371.
- [79] W. S. Choong, G. Hull, W.W. Moses, K.M. Vetter, S.A. Payne, N.J. Cherepy, J.D. Valentine, "Performance of a Facility for Measuring Scintillator Non-proportionality," *IEEE Trans. Nucl. Sci.*, vol. 55 (2008) pp.1073-1078.
- [80] P. R. Bevington, *Data Reduction and Error Analysis for the Physical Sciences*. McGraw-Hill: New York, 1969.
- [81] T. O'Haver, Interactive Peak Fitter, Vers. 2.3., Aug. 2008, University of Maryland, <http://terpconnect.umd.edu/~toh/spectrum/InteractivePeakFitter.htm>.

Appendix A

The following example illustrates how Eqns. (4.19) through (4.24) are applied to raw data to determine relative light yield. The procedure outlined in Example A.1 was formalized and programmed into MATLAB to produce relative light yield curves from data sets collected using the RLY system.

Example A.1

¹³⁷Cs spectra were recorded with a NaI:Tl spectrometer and a HPGe spectrometer. The full energy peaks were centered around $Pk_L = 7500\text{chns}$ and $Pk_G = 7400\text{chns}$. Calibration of the MCA found that $M = 786.36\text{chn/V}$ and $b = 11.912\text{chn}$. Begin by determining the system gains, G'_L and G'_G .

Begin by determining V_L and V_G from the recorded Pk_L and Pk_G respectively.

$$\bar{V}_L = \frac{(Pk_L - b)}{M} = 9.5225V$$

and

$$\bar{V}_G = \frac{(Pk_G - b)}{M} = 9.3953V.$$

From Eqn. (4.19), the NaI:Tl system gain is

$$G'_L = \frac{Pk_L}{E_{dep} R} = \frac{9.5225V}{662\text{keV} \cdot 1} = 0.0143844V / \text{keV}.$$

Similarly, from Eqn. (4.20), the calculated HPGe system gain is

$$G'_G = \frac{Pk_G}{E'_\gamma} = \frac{9.3953V}{662\text{keV}} = 0.0141923V / \text{keV}.$$

Now that the system gains are known, a single coincident event is recorded. The coincidence event yields $PH_L = 3800\text{chns}$ and $PH_G = 4000\text{chns}$. What is the relative light yield indicated by this data and at what energy?

Again, begin by determining the pulse heights of each.

$$V_L = \frac{(PH_L - b)}{m} = 4.8172V$$

and

$$V_G = \frac{(PH_G - b)}{m} = 5.0716V.$$

Thus, the amount of energy collected in the HPGe is

$$E'_\gamma = \frac{V_G}{G'_G} = \frac{5.0716\text{chns}}{0.0141923V / \text{keV}} = 357.347\text{keV}.$$

The energy deposited in the NaI:Tl was then

$$E_e = E_\gamma - E'_\gamma = 662 - 357.846 = 304.353\text{keV}$$

and the relative light yield at E_e is

$$R = \frac{V_L}{E_e G'_L} = \frac{4.8172V}{304.353\text{keV} \cdot 0.0143844V / \text{keV}} = 1.10$$

The collected coincidence event indicates $R(304.4\text{keV}) = 1.10$.

Collected coincident pulses from the RLY system described in Section 4.2.3 were stored in ASCII-formatted files to a PC. Analysis of the data required several steps to determine system gains and calculate relative light yield values for each pair of pulses collected.

The RLYMASTER.m function is the main function from which all subfunctions are called. Several adjustable parameters may be set to place limits on the relative light yields and deposited energies which will be considered valid. This function first determines the PMT and HPGe system gains at every gain check cycle. Next, relative light yields are calculated by calling CoincAnalyze.m. The final set of relative light yield and deposited energy pairs are finally stored to file.

```

%% RLYMASTER.m - Function to analyze coincidence data
% Author: Mark J. Harrison
% Date: January 8, 2009

%% Files called:
% (A tab indicates subfunction. Files listed in order called.)
% RLYMASTER.m
%   PMTGains.m
%   Step2.m

```

```

%           ImportCoinc.m
%           ChkData.m
%   GeGains.m
%       Step2.m
%           ImportCoinc.m
%           ChkData.m
%   CoincAnalyzer.m
%       Step2.m
%           ImportCoinc.m
%           ChkData.m

%% Initialize
clear all
close all
clc

%% Parameters
Eg = 661.657;           % Initial gamma ray energy (keV)

% Energy deposition limits
Eemax = 300;           % keV
Eemin = 5;             % keV

% Light yield limits
LYmax = 2.0;           % Max light yield
LYmin = 0.0;           % Min light yield

% MCA Calibration
m = 786.36;            % chns/V
b = 11.912;            % chns

%% Inputs
% Input filenames as string array
fnCoinc = {'coinc-02' 'coinc-03' 'coinc-04' 'coinc-05'...
           'coinc-06' 'coinc-07' 'coinc-08' 'coinc-09'};

fnPMT = {'cebr3-02' 'cebr3-03' 'cebr3-04' 'cebr3-05'...
         'cebr3-06' 'cebr3-07' 'cebr3-08' 'cebr3-09'};

fnGe = {'ge-02' 'ge-03' 'ge-04' 'ge-05'...
        'ge-06' 'ge-07' 'ge-08' 'ge-09'};

%% Get Gains
% Find FEP peak channels
PkPMT = PMTGains(fnPMT,m,b);
PkGe  = GeGains(fnGe,m,b);

% Calculate gains from peak data
Gpmt = PkPMT/Eg;
Gge  = PkGe/Eg;

%% Calculate relative light yields for each collection cycle
[junk Nf] = size(fnCoinc); % Count how many file names entered
RLY = []; Ee = []; tGe = []; tPMT = []; % Create cumulative arrays

```

```

% For each collection cycle, calculate relative light yield values for all
% pairs of pulse heights, then concatenate the data into cumulative arrays.
for i = 1:Nf
    [R ee tge tpmt] = CoincAnalyze(fnCoinc{1,i},Gpmt(i),Gge(i),...
        Eg,Eemax,Eemin,LYmin,LYmax,m,b);
    RLY = [RLY R];
    Ee = [Ee ee];
    tGe = [tGe tge];
    tPMT = [tPMT tpmt];
end;
clear R ee tge tpmt PkGe PkPMT i junk
display('Relative light yields calculated.');
```

%% Store calculated RLY values to file

```
save('OUT_FILE.mat');
```

PMTGains.m first imports each set of singles data collected for the purpose of correcting for PMT gain drift. The imported data is next histogrammed into a spectrum. A smoothing spline curve is fit to the data in the region of the FEP. This step smoothes out the FEP to ensure a more accurate peak centroid is chosen by minimizing the chance of choosing a peak channel number erroneously due to statistical variations. Finally, the peak centroid channel number is passed by to RLYMASTER.m for PMT system gain calculation.

```
function [PkPMT] = PMTGains(fnPMT,m,b)

% Energy regions of interest windows
PMTLo = (6000 - b)/m; % Low side of PMT ROI (chn)
PMTHi = (8055 - b)/m; % High side of PMT ROI (chn)
[junk Nf] = size(fnPMT); % Count how many file names entered

dc = abs(1/m);
cmax = (8191-b)/m;
cmin = (0-b)/m;
chns = cmin:dc:cmax;

%% Find peak channels of FEPs
for i = 1:Nf; % For every file entered
    [E1 E2 t1 t2 N] = Step2(fnPMT{1,i},m,b); % Import, reshape and check
data
    clear E1 t1 t2

    % Find data ranges
    E2r = max(E2) - min(E2);

    %% Fit spline to peak
    chns = cmin:dc:cmax;
    EE2 = histc(E2,chns);
```

```

EE2(1) = 0;
Efit = EE2(5500:8000);
chnfit = chns(5500:8000);
p = 0.9999;
pp=csaps(chnfit,Efit,p);

% Plot PMT Singles Spectrum
figure1 = figure('Color',[1 1 1]);
bar(chns,EE2);
hold on;
fnplt(pp,'r');
xlabel('Channel');
ylabel('Counts');
title('PMT Spectrum');
axis([min(chns) max(chns) 0 100]);

% Find peak channel number
x = PMTLo:0.1*dc:PMTHi;
v = fnval(x,pp);
maxV = max(v);
imax = find(v == maxV);
Xmaxi(i) = x(imax(1));

clear E2 E2r EE2 Efit chnfit chns imax maxV p pp v x
end;

%% Outputs
PkPMT = Xmaxi;
disp('PMT Gains calculated.');
```

GeGains.m operates on HPGe singles data in the same manner that PMTGains.m operates on PMT singles data. The key difference between the two subfunctions is the smoothing parameter used to fit the smoothing spline curve to the FEP. Due to the dramatically better energy resolution of the HPGe spectrometer, the smoother parameter used in GeGains.m allows a far less ‘smooth’ spline to be fit to the FEP.

```

function [PkGe] = GeGains(fnGe,m,b)

% Energy regions of interest windows
GeLo = (6000 - b)/m;           % Low side of PMT ROI (chn)
GeHi = (8000 - b)/m;           % High side of PMT ROI (chn)
[junk Nf] = size(fnGe);        % Count how many file names entered

dc = abs(1/m);
cmax = (8191-b)/m;
cmin = (0-b)/m;
chns = cmin:dc:cmax;

%% Find peak channels of FEPs
for i = 1:Nf;                   % For every file entered
```

```

[E1 E2 t1 t2 N] = Step2(fnGe{1,i},m,b); % Import, reshape and check data
clear E2 t1 t2

% Find data ranges
E1r = max(E1) - min(E1);

%% Fit spline to peak
chns = cmin:dc:cmax;
EE1 = histc(E1,chns);
EE1(1) = 0;
Efit = EE1(5500:8000);
chnfit = chns(5500:8000);
p = 1 - 1e-8;
pp=csaps(chnfit,Efit,p);

% Plot HPGe Singles Spectrum
figure1 = figure('Color',[1 1 1]);
plot(chns,EE1,'b-');
hold on;
fnplt(pp,'r');
xlabel('Channel');
ylabel('Counts');
title('HPGe Spectrum');
axis([min(chns) max(chns) 0 1.1*max(EE1)]);

% Find peak channel number
x = GeLo:0.1*dc:GeHi;
v = fnval(x,pp);
maxV = max(v);
imax = find(v == maxV);
Xmaxi(i) = x(imax(1));

clear E2 E2r EE2 Efit chnfit chns imax maxV p pp v x
end;

%% Outputs
PkGe = Xmaxi;
disp('HPGe Gains calculated.');
```

CoincAnalyze.m imports each set of coincidence data in turn, then eliminates data pairs outside time difference boundaries. Relative light yield and deposited energy values are next calculated. Finally, data pairs falling outside deposited energy and relative light yield limits are eliminated.

```

function [RLY,Ee,tGe,tpmt] =
CoincAnalyze(fn,Gpmt,Gge,Eg,Eemax,Eemin,LYmin,LYmax,m,b)

[PHGe PHpmt tGe tpmt N] = Step2(fn,m,b); % Import, reshape and check data

% Calculate Compton energies
Egp = PHGe/Gge; % Energy of gamma ray in HPGe pulse
```

```

Ee = Eg - Egp; % Energy assumed to be deposited in PMT

% Calculate relative light yields
RLY = PHpmt./(Ee*Gpmt); % Relative light yield at Ee

% Remove events outside Ee boundaries
iEe = find(Ee > Eemax | Ee < Eemin);
Ee(iEe) = []; RLY(iEe) = []; Egp(iEe) = [];
tpmt(iEe) = []; tGe(iEe) = [];

% Remove events outside RLY boundaries
iRLY = find(RLY > LYmax | RLY <= LYmin);
Ee(iRLY) = []; RLY(iRLY) = []; Egp(iRLY) = [];
tpmt(iRLY) = []; tGe(iRLY) = [];

```

Step2.m is a generic function used to call the file importing subfunction, call the data checking subfunction and reshape data arrays. This function is used for importing all singles data and all coincidence data.

```

function [EGe ENa tGe tNa N] = Step2(filename,m,b)

%% Import and Check Data for Errors
[datai Ni] = ImportCoinc(filename); % Read in data
[data N] = ChkData(datai,Ni); % Clean data
clear datai Ni

%% Reshape Data Arrays
dataB = reshape(data,7,N/7); % Reshape from a 1 col to 7 rows X N cols
clear data % Clear unneeded data

% Extract arrays of useful values
EGe = dataB(2,:); % Energy 1 (chn)
ENa = dataB(3,:); % Energy 2 (chn)
tGe = dataB(4,:); % Time 1 (ns)
tNa = dataB(5,:); % Time 2 (ns)
[junk N] = size(EGe);
clear dataB filename fups i junk

%% MCA Calibration
EGe = (EGe - b)./m; % Energy 1 (V)
ENa = (ENa - b)./m; % Energy 2 (V)

```

ImportCoinc.m is a generic function to simply read data files into MATLAB.

```

function [data N] = ImportCoinc(filename)

%% Import Data
fname = [filename '.asc']; % Source data file

```

```

format = '%f';

if (exist(fname) == 2)           % Check that the filename actually exists
    file_id = fopen(fname, 'r');
    data = [];
    while (1)
        segarray = textscan(file_id, format,1e5,'delimiter', ',');
        D = segarray{1,1};
        clear segarray
        data = [data; D];
        [N junk] = size(data);
        clear D junk
        if (feof(file_id))       % check for end of file
            break
        end
    end
else
    error('Check input file name.');
```

ChkData.m is a generic function to check that six values follow each header value. If more than six or fewer than six values are detected between two header values, the data is removed from the overall data array.

```

function [data2 N2] = ChkData(data,N)

%% Check data for errors
hdrs = find(data == 1193046);      % Find flags
[Nh junk] = size(hdrs);           % Count how many flags were found

bp = [];                           % Initialize bp array
nbad = [];                          % Initialize nbad array

for i = 2:Nh;                       % For all flags found
    diffh = hdrs(i) - hdrs(i-1);   % Count how far each flag is from the
previous flag
    if diffh ~= 7                   % If distance b/w flags is NOT 7
        bp = [bp; i - 1];          % Mark previous flag as bad
        nbad = [nbad; diffh];      % Remember how many til next good flag
    end;
end;

%% Remove bad data points
badpt = hdrs(bp);                  % Bad points
[Nb junk] = size(badpt);           % Number of bad points
NumberBadPoints = Nb;

for k = Nb:-1:1                     % For every bad point (end to beginning)
    data(badpt(k):badpt(k)+nbad(k)-1) = []; % Delete bad data
end;
```

```

end;

[N2 junk] = size(data);

%% Double check that data is good now
% Send data through same algorithm as above and check that the number of
% found bad points is now zero.
hdrs2 = find(data == 1193046);
[Nh2 junk] = size(hdrs2);

bp2 = [];
nbad2 = [];

for i = 2:Nh2
    diffh2 = hdrs2(i) - hdrs2(i-1);
    if diffh2 ~= 7
        bp2 = [bp2; i - 1];
        nbad2 = [nbad2; diffh2];
    end;
end;
%% Display error if data not clean
if bp2 ~isempty(bp2);
    error('Data still contains errors after cleaning.');
```

```

end;

rem = mod(N2,7);
data2 = data(1:end-rem);
N2 = N2 - rem;

clear N Nb Nh Nh2 Ni badpt bp bp2 data datai diffh diffh2
clear hdrs hdrs2 i junk k nbad nbad2
```